VRIJE UNIVERSITEIT

SPECTROSCOPY OF HIGHLY-CHARGED SN IONS FOR EXTREME ULTRAVIOLET NANOLITHOGRAPHY

ACADEMISCH PROEFSCHRIFT

ter verkrijging van de graad Doctor
aan de Vrije Universiteit Amsterdam,
op gezag van de rector magnificus
prof.dr. V. Subramaniam,
in het openbaar te verdedigen
ten overstaan van de promotiecommissie
van de Faculteit der Bètawetenschappen
op donderdag 19 december 2019 om 09.45 uur
in de aula van de universiteit,
De Boelelaan 1105

door

Francesco Torretti

geboren te Civitanova Marche, Italië

promotoren:	prof.dr. W. M. G. Ubachs
	prof.dr.ir. R. A. Hoekstra
copromotor:	dr. O. O. Versolato

This thesis was approved by the members of the reviewing committee:

prof.dr.ir. G. J. L. Wuite (Vrije Universiteit Amsterdam)
prof.dr.ir. U. Ebert (CWI Amsterdam and TU Eindhoven)
prof.dr. F. E. Schreck (Universiteit van Amsterdam)
Priv.-doz.dr. J. R. López-Urrutia (MPI für Kernphysik Heidelberg)
dr.ir. H. O. Folkerts (ASML)

The research reported in this thesis was carried out at the Advanced Research Center for Nanolithography (ARCNL), a public-private partnership between the University of Amsterdam (UvA), Vrije Universiteit Amsterdam (VU Amsterdam), the Netherlands Organization for Scientific Research (NWO), and the semiconductor equipment manufacturer ASML.

On the cover: Spectral flux of an infinitesimally-thick, one-dimensional, homogeneous Sn plasma at 32 eV and $10^{20}\, e/\mathrm{cm}^3$, obtained by solving the radiation transport equation for the opacity spectrum presented in Chapter 6.

Cover design by Domile Torretti.

ISBN: 978-94-92323-30-9

CONTENTS

List of Figures

LIST OF TABLES

Introduction

> There is nothing like professionalism. It is what makes humanity worth preserving.
>
> Jerry Seinfeld

Since the invention of the transistor [1, 2] and its applications in integrated circuits [3, 4], semiconductor devices have become ubiquitous in our everyday lives. The generic term "semiconductor devices" casts a very wide net, covering small and low-power microprocessors found in ultra-thin laptops, smartphones, smartwatches and other wearables; flash memory like NAND Flash or V-NAND; random-access memory, i.e. DRAM or SRAM; and reaching all the way to server-grade equipment for cloud computing infrastructures and data centers. Undoubtedly, these devices affect society in a deep manner and drastically improve our lives. Moreover, the semiconductor industry is a strong player in the world economy, having grown in 2017 to be a €360 billion industry [5] while also powering the much larger economy of the products related to integrated circuits.

Improvements in the design of integrated circuits can be attributed, amongst other factors, to the miniaturization of micro-electronic components enabling, for example, a greater number of transistors per unit area in a microprocessor. It was first Gordon Moore, co-founder of Intel, who predicted in 1965 that the number of components in integrated circuits would double every year [6]. Ten years later, once this empirical law was adjusted to doubling every two years [7], it became a point of reference for chipmakers and the semiconductor industry. Thanks to the effort of industrial partners to co-ordinate their activities through the bi-yearly release of a research road map [8], Moore's law, as it became known, has been followed for the past five decades [9].

The shrinking of components, and the faultlessness of Moore's law, is directly driven by improvements in the industrial process for the production of

integrated circuits: photolithography [10]. In its simplest form, the photolithographic process consists of a light source projecting a pattern onto a silicon wafer covered with a medium (photoresist) which reacts with the light in such a way that further processing of the wafer will imprint the pattern on the semiconductor. It is quite intuitive to understand that the performance of a photolithograpic system, in terms of the size of the imprinted features, is directly linked to the optical properties of the light source and of its optical system used to project the pattern onto the wafer. The minimum resolvable feature, most commonly referred to as the critical dimension (CD), is determined by the following equation:

$$\mathrm{CD} = k_1 \cdot \frac{\lambda}{\mathrm{NA}}, \tag{I.1}$$

where k_1 is a constant related to the specifics of the lithographic process, λ is the photon wavelength, and NA is the numerical aperture of the optical system. In the past few decades, the vast majority of improvements in CD came from reduction of the exposure wavelength or increases in the numerical aperture. Figure I.1 illustrates the development of photolithography machines from the Dutch company ASML [11] in the last 35 years. The miniaturization of the critical dimension over these years is clearly shown to be driven by the factors discussed above. The CD presented here refers to the minimum dimension achievable in a single exposure. In reality, thanks to the adoption of advanced techniques such as multiple-patterning [12], the final critical dimension can be made much smaller than the resolution limit. In fact, features down to 20 nm have been produced with 193 nm illumination. This, however, comes at great economic costs due to the multiple illumination and development cycles required for a single wafer.

In order to address these increased costs and to allow for smaller CD in a single wafer exposure, the industry has spent the last 20 years preparing for the paradigm shift of extreme ultraviolet (EUV) lithography [14, 15], in which the exposure wavelength of choice is 13.5 nm. In fact, going from 193 nm to 13.5 nm means that drastic changes need to be enacted in the entirety of the lithographic machine. First of all, such short-wavelength radiation is strongly absorbed by the vast majority of media, and therefore the entire process must be carried in vacuum. For the very same reason, lenses cannot be employed in the optical system which must be re-designed using only reflective elements. Even in the case of mirrors, special coatings must be used to ensure that the radiation will in fact be reflected from the surface. Fortunately, it is possible to manufacture multi-layer mirrors (MLMs) with the ability to reflect 13.5 nm photons [16]: by alternating few-nm-thick layers of molybdenum and silicon, the incoming radiation will interfere within these layers and be reflected, with maximum peak

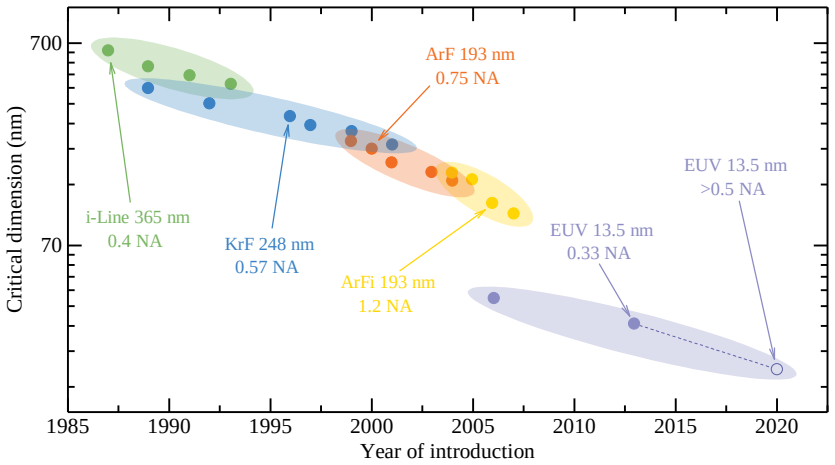

FIGURE I.1 Miniaturization of the single-exposure critical dimension in the past 35 years for ASML lithography machines. The various exposure wavelengths and the respective light sources are indicated by the different colors: in green, 365 nm i-Line (emission from a Hg lamp filtered at the desired wavelength); in blue, 248 nm KrF excimer laser; in orange, 193 nm ArF excimer laser; in yellow, 193 nm ArFi which uses the same ArF laser but with the wafer immersed in water allowing for a NA above 1; in violet, 13.5 nm generated by Sn laser-produced-plasma (see main text). Adapted from Ref. [13].

reflectivities of approximately 70 % centered at 13.5 nm with a 2 % bandwidth. It is now only a matter of producing the short-wavelength photons.

In industrial applications, the EUV photons are generated by irradiating micrometer-sized droplets of molten Sn with an intense laser pulse [17, 18]. High-power 10.6-μm-wavelength CO_2 lasers are currently employed, being able to produce the necessary laser intensities, in the order of $10^{10}\,\mathrm{W/cm^2}$, which allow for the creation of a hot, dense Sn plasma. To improve the conversion of laser light into EUV photons, a two-step process is adopted in which a low intensity laser *prepulse* first deforms the spherical droplet into a flat, disk-like target [19, 20]. Following this deformation, a higher intensity *main pulse* irradiates the target generating a plasma having temperatures and densities in the range 20–40 eV and 10^{18}–$10^{19}\,e/\mathrm{cm^3}$, respectively [21]. This process is repeated with frequencies up to 50 kHz. These sources are currently able to convert laser light into EUV with an efficiency of 5–6 %, allowing for the production of 250 W of EUV power in the 2 % bandwidth delivered by the source to the lithogra-

phy scanner. In the pursuit of producing more and more EUV photons, there exists a line of research into 1-μm-wavelength-driven sources [22]. Solid-state YAG lasers offer many technological advantages over CO_2 gas lasers, such as more compact size, improved wall-plug efficiencies, and better temporal pulse-shaping capabilities. The applicability of these solid-state lasers in EUV sources have been studied both for the prepulse [23–26] and the main pulse [27]. The shorter laser-wavelength introduces some interesting changes at the physical level: 1-μm radiation, in fact, is capable of traveling into plasma regions one hundred times denser than in the CO_2-laser case. This density increase has several consequences, e.g. increasing the laser absorption by the plasma to near-unity values. More importantly, when looking at main pulse YAG applications, EUV photons are now being produced at higher plasma densities. These conditions are such that now, in comparison with CO_2-produced-plasma, the emitted radiation suffers from self-absorption due to the surrounding ions. Absorption is well-known to cause broadening of the spectral emission features [28, 29], to some extent re-distributing energy across the spectral range outside the bandwidth accepted by MLMs. This lowers the overall conversion efficiency of laser light into EUV photons, with the record-high number recently recorded of 3.2 % [27].

The peculiar aptness of Sn laser-produced plasma to generate EUV photons is ultimately connected to the fortuitous atomic structure of the Sn ions at play in these processes [30]. For the plasma conditions outlined in the previous paragraph, the Sn^{10+}–Sn^{14+} ions are produced. Their atomic structures are determined by their ground configurations in the form $4p^6\,4d^m$, with $m = 4 - 0$. It is fairly well established that Sn ions exhibit an interesting behavior regarding their electric dipole excitations $4p \rightarrow 4d$ and $4d \rightarrow 4f$, resulting in the strongly-mixed excited configurations $4p^5\,4d^{m+1}$ and $4p^6\,4d^{m-1}\,4f$, respectively. These excited configuration and their respective levels have very similar excitation energies, and therefore strong configuration-interaction effects are observed [31], which cause a re-distribution of the transitions oscillator strengths to favor, in the Sn case, the short-wavelength transitions around 13.5 nm [30]. The coupling of high-angular-momentum electrons generates a considerable amount of states, which in turn allows for several thousands radiative de-excitation channels towards the ground levels of the ions through strong electric dipole transitions [32–36]. Moreover, these transition energies remains fairly constant across the isonuclear sequence Sn^{10+}–Sn^{14+} [37] as seen in figure I.2, which illustrates these properties using the emission spectra of Sn ions obtained in an ion trap. Therefore, Sn ions are excellent, bright radiators of 13.5 nm photons, with their serendipitous atomic structure being, for the most part, responsible for Sn becoming the element of choice for the lithography industry, above other EUV radiators such as Xe or Li.

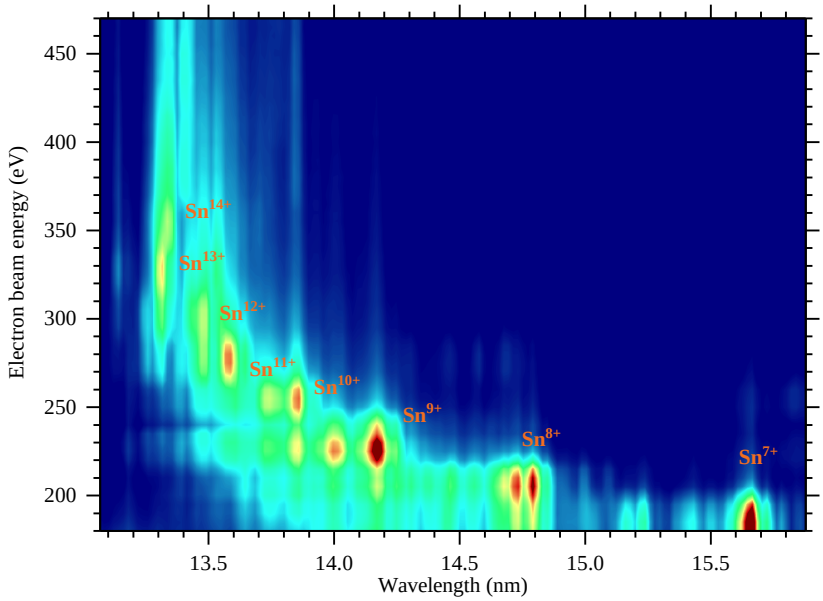

FIGURE I.2 Fluorescence of Sn ions measured at an electron beam ion trap at the Max Planck institute for Nuclear Physics in Heidelberg. The electron beam energy, shown on the y-axis, determines the ionization staged produced in the ion trap (see chapters 1 and 2 for more details). The emission here presented is from transitions to the ground configurations of these ions from the excited states $4p^5\,4d^{m+1}$ and $4p^6\,4d^{m-1}\,4f$, where $m = 7 - 0$ for Sn^{7+}–Sn^{14+}.

Thesis outline and summary

This thesis aims to further the understanding of the Sn ions responsible for emission of 13.5 nm radiation in laser-produced-plasma EUV sources for the nanolithographic industry. It collects the work performed at the Advanced Research Center for Nanolithography (ARCNL) in Amsterdam, in the EUV Plasma Processes group, and partly at the Max Planck Institute for Nuclear Physics in Heidelberg, Germany.

Chapter 1 and chapter 2 present the results of optical spectroscopy performed in an electron beam ion trap at the Max Planck institute for Nuclear Physics in Heidelberg, Germany. The ions Sn^{7+}–Sn^{14+} were created in the magnetic field of the ion trap using a monochromatic high-energy electron beam. The electrons ionize and excite the Sn ions through ion-electron collisions. Due

to the low collision frequency, the excited states are allowed to cascade towards their ground states and even transitions with very low transition probabilities can be observed. In these chapters, the magnetic dipole transitions within the ground-state manifolds of the studied ions were measured in the 200–700 nm range. These transitions were identified using three different atomic structure codes: the semi-empirical Cowan code, based on the semi-relativistic Hartree-Fock approach; the ab initio TRAFS-3C (Tel Aviv relativistic atomic FSCC code), based on Fock space coupled cluster; and the ab initio AMBiT code, based on the configuration-interaction + many-body perturbation theory. The work in these chapters presents two important results: firstly, the capabilities of these ab initio codes are such that even the complicated open-$4d$-shell atomic structure of the Sn ions investigated can be calculated with an unprecedented level of accuracy, which yet is still not sufficient to perform line-assignments without the help of semi-empirical Cowan code calculations; secondly, the level assignments performed have re-evaluated the fine structure of these ions, highlighting inaccuracies in previous, ground-laying works which will have to be revised.

Spectroscopy remains the main focus of chapter 3, but in the extreme ultraviolet regime. The light source used is a custom-built, droplet-based, laser-produced-plasma Sn EUV source built at ARCNL. The micrometer-sized droplets were irradiated by a high-energy, high-intensity 1-µm-wavelength laser pulse. The emission between 6 nm and 17 nm was recorded. This chapter focuses on the so-called "out-of-band" radiation, i.e. radiation outside the 2 % wavelength bandwidth, in order to unravel the various charge state contributions which are unresolved around 13.5 nm. The emission features found between 6 nm and 12 nm were investigated using the flexible atomic code (FAC). The investigation showed that a previous publication examining the same transitions had neglected what the present study has identified as the main contributor to the spectrum. The atomic structure calculation successfully associated all emission features observed to electric dipole transitions from excited states towards the ground-state manifold.

The results on the out-of-band radiation are applied in chapter 4 in order to analyze EUV spectra obtained at an industrial ASML light source. During the experiments, performed in the EUV cleanroom at ASML Veldhoven, the 10-µm-wavelength drive laser beam-spot was changed through manipulation of the beam optics. Changing the size of the laser beam, while keeping laser energy and duration constant, results in intensity changes. In laser-produced-plasma physics, laser intensity is the principal quantity setting the plasma temperature. By fitting the atomic structure calculations presented in chapter 3 to the experimental data, the contributions of the charge states Sn^{9+}–Sn^{15+} to the spectrum are determined for each experimental condition. The variations of these contributions can be used as a proxy for the charge state populations in the plasma. In

order to understand the scaling of temperature with laser intensity, the fitting results are compared to charge state population calculations performed with the non-equilibrium plasma-population kinetic code FLYCHK. The comparison shows that, for the EUV source here investigated, plasma temperature scales rather weakly with laser intensity, much weaker than expected when looking at theoretical scalings found in previous publications.

The concepts of radiation transport and optical depth, important for every heavily-radiating medium, are introduced in chapter 5. A multitude of experimental EUV spectra were obtained from the droplet-based EUV source at ARCNL, whereby the laser energy, laser pulse duration, and droplet size were varied while maintaining the average laser intensity. Increasing droplet size or laser-pulse duration is shown to broaden the emission spectra, a phenomenon most commonly associated with an increase in the number of absorbers in the plasma. A simple 1D radiation transport model is employed, which, surprisingly, is able to explain all the experimental spectra in terms of an increase of optical depth, the quantity directly related to the column density of Sn ions that affect the emission properties of the plasma. The knowledge of this scaling may drive the improvement of 1-μm-driven EUV sources to compete against 10-μm-driven sources in term of performance.

Chapter 6 deals with the topic of the opacity of Sn laser-produced-plasma. Opacity is closely related to be the absorption spectra of a medium and its characteristics are determined by the elements atomic structure and their level populations. Moreover, in certain equilibrium conditions, opacities are also directly connected to the emission characteristics of a plasma. Overall, these quantities are of great interest for modeling radiation transport in a system such as Sn laser-produced plasma, for example in radiation hydrodynamics simulations. The work in this chapter presents extensive opacity calculations, performed at the Los Alamos National Laboratory, which include 10^{10} electric dipole transitions per ions. The calculations are able to excellently reproduce the experimental spectra measured at ARCNL, highlighting that the vast majority of the light emission originates from transitions between highly-excited states serendipitously aligned around 13.5 nm, and not from singly-excited, 92-eV-average-energy states decaying to the ground configuration. These properties, overlooked in the literature thus far, demonstrate that the common picture of light emission from highly charged tin ions in laser-produced plasma must be revised.

CHAPTER ONE

ANALYSIS OF THE FINE STRUCTURE OF Sn^{11+}–Sn^{14+} IONS BY OPTICAL SPECTROSCOPY IN AN ELECTRON BEAM ION TRAP

A. Windberger, F. Torretti, A. Borschevsky, A. Ryabtsev, S. Dobrodey, H. Bekker, E. Eliav, U. Kaldor, W. Ubachs, R. Hoekstra, J. R. Crespo López-Urrutia, and O. O. Versolato

Physical Review A **94**(1), 012506 (2016)

We experimentally re-evaluate the fine structure of Sn^{11+}–Sn^{14+} ions. These ions are essential in bright extreme-ultraviolet (EUV) plasma-light sources for next-generation nanolithography, but their complex electronic structure is an open challenge for both theory and experiment. We combine optical spectroscopy of magnetic dipole $M1$ transitions, in a wavelength range covering 260 nm to 780 nm, with charge-state selective ionization in an electron beam ion trap. Our measurements confirm the predictive power of *ab initio* calculations based on Fock space coupled cluster theory. We validate our line identification using semi-empirical Cowan calculations with adjustable wavefunction parameters. Available Ritz combinations further strengthen our analysis. Comparison with previous work suggests that line identifications in the EUV need to be revisited.

1.1 Introduction

The strongly correlated electronic structure of heavy, multi-electron open shell ions is notoriously difficult to calculate and their complicated structure furthermore hampers straightforward experimental assessment. A typical example of this class of systems are Sn ions in charge states 7+ through 14+ with their open [Kr] $4d$ shell structure. These specific ions are used to generate extreme ultraviolet (EUV) light at 13.5 nm wavelength in laser-produced-plasma (LPP) sources for nanolithographic applications [38,39]. The EUV light is generated by thousands of transitions that form so-called unresolved transition arrays (UTAs) with little dependence on the charge state of the ion. For the relevant [Kr] $4d^m$ tin ions, with m=6-0 [30], the EUV-contributing upper configurations are $4p^6\,4d^{m-1}\,4f^1$, $4p^6\,4d^{m-1}\,5p^1$, and $4p^5\,4d^{m+1}$. The sheer multitude of lines in these UTAs complicates their accurate identification. Spectroscopic work using discharge sources [32–36,40], laser-produced-plasmas [41], or tokamaks [42,43] is challenging as the UTAs of various Sn ions are strongly blended. Nevertheless, work on discharge sources provides the most accurate spectroscopic data to date for highly charged Sn ions.

Besides experiments on thermal plasmas, there is work on charge state-resolved spectroscopy in the EUV regime. Charge-exchange spectroscopy (CXS) was performed by means of Sn ion beams colliding on He [37,44–46] and Xe [37] gas targets. The spectral accuracy achieved in those studies was lower than that of the discharge work due to instrument resolution. Studies using electron beam ion traps (EBITs) [44,47] which also provide charge state selectivity were similarly limited. In addition, the EBIT studies focused on the higher charge states of tin, outside of the range most relevant for EUV plasma sources. For these reasons, none of the charge-state-resolved studies could so far directly challenge the spectral data obtained from discharge sources.

The above issues of unresolved transitions in UTAs and limited resolution can be circumvented by turning to the optical range and addressing the optical magnetic dipole ($M1$) transitions between fine structure levels in the ground electronic configuration (see Fig. 1.1). This approach eliminates the uncertainties introduced by the reconstruction of ground state levels using a Ritz procedure based on the measured EUV lines. Such optical lines of Sn in charge states beyond 3+ have not been identified before.

We present results from charge state-resolved optical spectroscopy on Sn^{11+}–Sn^{14+} using FLASH-EBIT [49] at the Max Planck Institute for Nuclear Physics in Heidelberg. Tuning the energy of the electron beam enables us to assign each of the observed spectral lines to specific charge states. The $M1$ transitions are assigned using *ab initio* Fock space coupled cluster (FSCC) [50,51] calculations and we confirm them with the help of the semi-empirical Cowan code [52], which

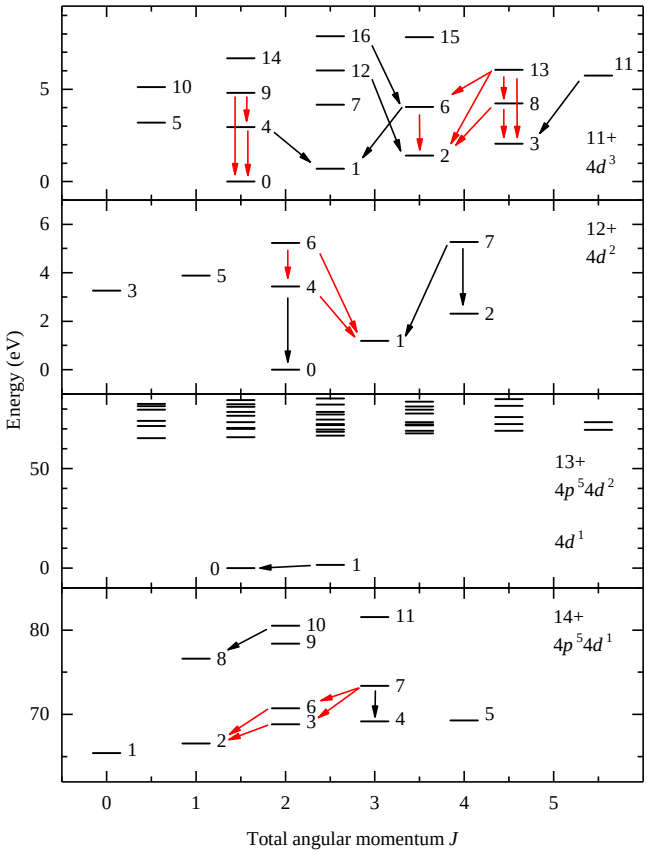

FIGURE 1.1 Grotrian diagrams obtained from Flexible Atomic Code calculations [48] depicting the atomic structure of the lowest energy configurations exhibiting optical magnetic dipole $M1$ transitions of the Sn charge states investigated in this work. The closed-shell [Kr] ground state of Sn^{14+} has no splitting; instead the first excited configuration is shown. The levels are numbered following their energy ordering. Their respective term symbols can be found in Table 1.3. Identified transitions are marked by arrows: (red) transitions confirmed by Ritz combinations; (black) the remainder. All observed spectral lines and identified transitions are listed in Table 1.1.

allows adjusting wave function scaling parameters to fit the observed spectra.

Optical transitions in heavy multi-electron open shell ions like Sn^{11+}–Sn^{14+} represent a stringent test for *ab initio* atomic structure calculations of strongly correlated many-electron ions. These transitions have non-negligible Breit contributions. Application of FSCC theory to this type of problems where multiple vacancies with high angular momenta can couple to each other is a promising approach. Coupled cluster methods have found wide application since the 1950s to analogous problems found in nuclear physics and quantum chemistry, yet their use for atomic physics problems involving highly charged ions is more recent (see, e.g., Ref. [53]). There are only few such works so far although the methods consistently show good agreement with experiment (see, e.g., Refs. [54–57]). It is therefore instructive to explore their *ab initio* performance in specific cases where other established calculational tools require empirical adjustments and judicious choices of configuration sets in order to analyze spectral data. Therefore, with optical spectroscopic studies we can address the issue of a precise theory-experiment comparison in complex open-shell systems without the high spectral density that has to be faced in EUV spectroscopy work. In the present case, both the important practical applications of the ions under study as well as the relative novelty of using FSCC calculations for them make such a comparison particularly valuable.

Our data enable a re-evaluation of the fine structure splitting of Sn^{11+}–Sn^{14+} ions and provide a benchmark for state-of-the-art atomic structure calculations such as FSCC. We infer that the identification of EUV lines needs to be revisited in previous works such as Ref. [32, 34] as was also suggested previously in Ref. [58]. The line identifications in those works constitute the basis for plasma modeling of EUV light sources.

1.2 Experiment

We produced and trapped Sn ions with FLASH-EBIT [49] using a monoenergetic electron beam to bring them to the desired charge state. The beam energy was controlled by the acceleration potential applied between the emitting cathode and the central trap drift tube. High current densities were reached by compressing the electron beam down to a diameter of approximately 50 μm using the 6 T magnetic field produced by a pair of superconducting Helmholtz-coils. A tenuous, well collimated molecular beam generated by the evaporation of volatile tetra-i-propyltin ($C_{12}H_{28}Sn$) was the carrier of Sn atoms into the electron beam, which dissociated the molecule and preferentially trapped the heavy Sn ions thereby produced. While the lighter atoms and ions of C and H escaped from the trap, Sn ions remained trapped, radially by the space charge potential

of the electron beam and axially by a potential generated by a set of drift tubes.

The trapped ions were electronically excited by electron impact to a manifold of states, many of them close to the ionization continuum since the beam energy is close to the respective ionization threshold.

Subsequent fluorescent cascades down towards the ground state cover a broad spectral range. This light was focused onto the entrance slit of a 320 mm-focal-length spectrometer employing a 300 lines/mm grating. We use in this work a low groove density grating and a short focal distance instrument for the convenience of having a broad spectral coverage, given the large number of spectra to be acquired. The spectral image recorded by a cooled CCD is integrated along the nondispersive axis after correcting for optical aberrations and removing cosmic muon events. Line widths of typically $\sim$1 nm (full-width-at-half-maximum) were obtained near 400 nm wavelength. For calibration a Hg or a Ne-Ar lamp was placed in front of the spectrometer entrance slit.

A typical acquisition cycle consisted of a short calibration and a series of 30 min exposures. After each acquisition the electron beam acceleration potential was increased by 10 V starting from a minimum acceleration potential of 137 V and ending at 477 V. The electron beam current was kept at a constant 10 mA. The dense electron beam produces a strong space charge potential which is partially compensated by the trapped ions [59, 60]. This reduces the acceleration potential by $\sim$20-40 V [61] to yield the actual electron beam energy in the interaction region. The chosen range of the acceleration potential enabled the production of charge states from Sn^{7+}, with its ionization potential (IP) of 135 V [62, 63] up to Sn^{16+} with IP $= 437$ V. We focus on the charge states Sn^{11+}–Sn^{14+} that could be reliably identified.

After stepping the EBIT acceleration potential through the full voltage range, the rotatable grating was set to cover a 125 nm adjacent wavelength range. Typically, a range of 270 nm was recorded at each grating position, so that the different regions overlapped. Next, the acceleration potential was stepped through again. This procedure was repeated for three settings of the spectrometer grating to cover the full accessible wavelength range from 260 nm to 780 nm.

1.3 Theory

Two calculational methods are compared in this work. First, we present dedicated *ab initio* FSCC calculations and show the accuracy of these predictions by comparison with our experimental data. Second, we compare them with Cowan code calculations using empirically adjusted wavefunction scaling parameters. This code is a mature tool used to identify lines, and serves particularly well when a combination of experimental observations provides additional data on

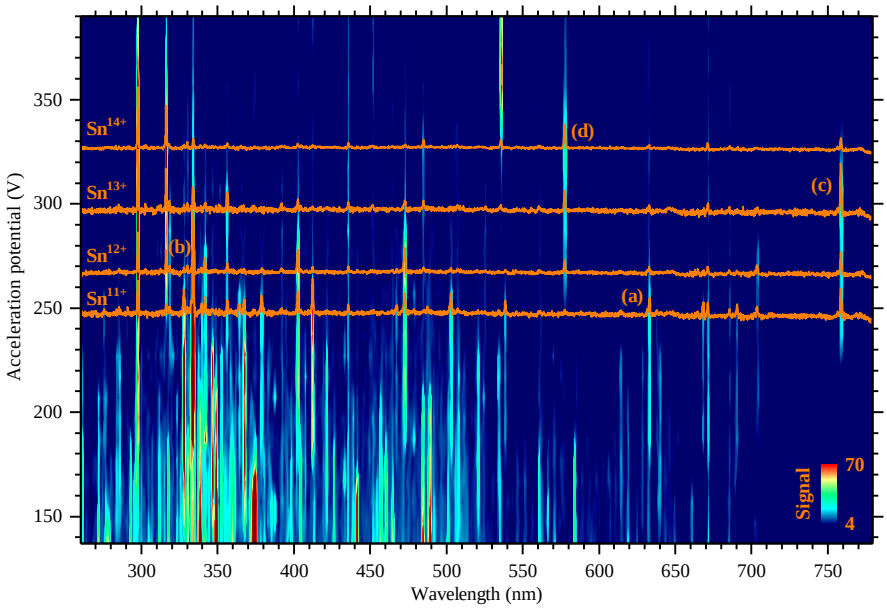

FIGURE 1.2 Composite spectral map of Sn ions interpolated between discrete voltage steps of the EBIT acceleration potential at a 10 mA beam current. The orange curves represent spectra of Sn^{11+}–Sn^{14+} ions taken at a maximum of the fluorescence yield of a specific charge state; they are individually scaled for better visibility. Enlarged sections around the lines indicated by symbols (a), (b), (c), and (d) can be found in Fig. 1.3 to visualize the identification of charge states through their fluorescence profiles.

electronic energy levels for their empirical adjustment. We also use it to obtain weighted transition rates gA used to predict line strengths. When necessary, auxiliary calculations were carried out with the Flexible Atomic Code (FAC) [48].

Fock space coupled cluster

Calculations of the transition energies were performed for the ions of interest using the FSCC method within the framework of the projected Dirac-Coulomb-Breit Hamiltonian [64],

$$H_{DCB} = \sum_i h_D(i) + \sum_{i<j} (1/r_{ij} + B_{ij}). \tag{1.1}$$

Here, h_D is the one-electron Dirac Hamiltonian,

$$h_D(i) = c\boldsymbol{\alpha}_i \cdot \mathbf{p}_i + c^2\beta_i + V_{nuc}(i), \tag{1.2}$$

where $\boldsymbol{\alpha}$ and β are the four-dimensional Dirac matrices. The nuclear potential $V_{nuc}(i)$ takes into account the finite size of the nucleus, modeled by a uniformly charged sphere [65]. The two-electron term includes the nonrelativistic electron repulsion and the frequency independent Breit operator,

$$B_{ij} = -\frac{1}{2r_{ij}}[\boldsymbol{\alpha}_i \cdot \boldsymbol{\alpha}_j + (\boldsymbol{\alpha}_i \cdot \mathbf{r}_{ij})(\boldsymbol{\alpha}_j \cdot \mathbf{r}_{ij})/r_{ij}^2], \tag{1.3}$$

and is correct to second order in the fine structure constant. The calculations for Sn^{14+}, Sn^{13+}, and Sn^{12+} started from the closed shell reference $4s^2\,4p^6$ configuration of Sn^{14+}. In the current state of the code, atomic systems with a maximum of two open shell electrons/holes can be treated, which does not apply to Sn^{11+} with its $4s^2\,4p^6\,4d^3$ ground state configuration. After the first stage of the calculation, consisting of solving the relativistic Hartree-Fock equations and correlating the closed shell reference state, different FSCC schemes were used for the different ions. In case of Sn^{14+}, a single electron was excited from the $4p$ to the $4d$ orbital to reach the $4p^5\,4d^1$ configuration. For Sn^{12+}, two electrons were added to the closed shell reference state. In this calculation, to achieve optimal accuracy, a large model space was used, comprised of three s, three p, three d, three f, two g, and one h orbitals. The intermediate Hamiltonian method was employed to facilitate convergence [66]. The fine structure splitting of Sn^{13+} was also obtained in the framework of this calculation, as a result of adding the first electron to the closed shell reference state.

The uncontracted universal basis set [67] was used for all the ions, consisting of 37 s, 31 p, 26 d, 21 f, 16 g, 11 h, and 6 i functions; the convergence of the obtained transition energies with respect to the size of the basis set was verified. All the electrons were correlated. The FSCC calculations were performed using the Tel-Aviv Relativistic Atomic FSCC code (TRAFS-3C) [68].

Lamb shifts for the various levels were obtained using the recently developed effective potential method, implemented in the QEDMOD program [69]. Here, an important feature is the inclusion of both the vacuum polarization and the self-energy components of the Lamb shift into the self-consistent field procedure. Thus, together with the first order QED interactions, many important higher order terms are included in the final Lamb shift expression. Its contribution to level energies is typically 20-60 cm^{-1}. The results of the calculations are presented in Table 1.3 where they are compared to the experimental results, as will be discussed in the next section.

Cowan

In the Cowan code [52], radial wavefunctions are obtained with a Hartree-Fock relativistic (HFR) method using a correlation term in the potential but accounting for the Breit interaction only partially. With these wavefunctions, the electrostatic single configuration radial integrals F^k and G^k (Slater integrals), configuration-interaction Coulomb radial integrals, and spin-orbit parameters ζ are then calculated. From these, the energy levels and intermediate coupling eigenvectors are extracted. Subsequently, *ab initio* values are obtained for the wavelengths and transition probabilities. However, the resulting energy level splittings are generally larger than those observed because of the cumulative influence of a large number of small perturbations originating from configuration interactions. To compensate for these effects the *ab initio* values of the electrostatic integrals are empirically scaled down by a factor between 0.7 and 0.95, depending on the charge state. Spin-orbit parameters can also be scaled. Both scalings are needed for a semi-empirical adjustment of the predicted spectrum that can be performed if enough experimental levels are available. The electrostatic and spin-orbit integrals are then adjusted to give the best possible fit of the calculated eigenvalues to the observed energy levels. Effective Coulomb-interaction operators α, β, and $T1$ are added as fit parameters to represent weak configuration-interaction corrections to the electrostatic single configuration effects. The results of this semi-empirical adjustment procedure are more useful for the interpretation of a particular experimental spectrum than the *ab initio* Cowan calculation. Additionally, the empirical ratios of the fitted (FIT) to the HFR energy parameters can be extrapolated, e.g., to neighboring ions along an isoelectronic sequence to improve the reliability of *ab initio* predictions.

1.4 Results

In the following, we present optical spectra of tin ions in charge states Sn^{11+}–Sn^{14+} obtained in a charge-state-resolved manner (see Figs. 1.2 and 1.3). We interpret the data using FSCC predictions and semi-empirical Cowan code calculations. Furthermore, we perform a comparison with predicted optical transition energies inferred from existing data in the EUV regime. First, we discuss the charge state identification and, second, the line identifications. All results are summarized in Tables 1.1, 1.2, and 1.3.

Charge state identification

Scanning the electron beam energy enables the assignment of lines to specific charge states (see Refs. [61, 70] and references therein) although the absolute

determination of a charge number can be challenging (see, e.g., Ref. [71]). A typical characteristic of EBIT spectra is that groups of spectral lines that exhibit the same dependence on the acceleration potential can be assigned to the same charge state (see Fig. 1.2). The appearance and disappearance of sets of lines enables the construction of a "ladder" of charge states (see Fig. 1.3). The challenge remaining is to pinpoint a single charge state, with which the others would be easily identified counting up and down. For this purpose, we used the fact that the [Kr] $4d^1$ ground state configuration of Sn^{13+} allows for only a single optical transition originating from the $4d\,^2D_{3/2}$–$^2D_{5/2}$ fine structure splitting (see Fig. 1.1). This transition is predicted by FSCC to occur near 13 144 cm^{-1} (see Table 1.3), in agreement with the 13 212(25) cm^{-1} obtained from the EUV spectra in Refs. [34, 35]. The brightest line, observed at 758.8(4) nm wavelength or 13 179(8) cm^{-1} is an excellent match for it. This unambiguously fixes the identification of Sn^{13+} and with it, that of the other charge states (see Fig. 1.3).

The onsets of fluorescence for all identified charge states occurred at lower acceleration potentials than expected from theory [62, 63] as is depicted in Fig. 1.3. This, together with the shape of the fluorescence curves, indicates strong contributions from metastable states [72]. The doubly peaked structure observed for all four charge states hints at metastable states at an excitation energy of ∼60 eV. This excitation energy is similar to that of the low-lying high-J levels of the first excited configuration $4p^5 4d^{m+1}$ that are metastable for decay through electric dipole $E1$ transitions. The observed dependence of the fluorescence of a particular charge state Sn^{11}–Sn^{14+} on the electron beam energy can be qualitatively understood by the sequential opening of four different channels (see Fig. 1.4). Such strong contributions from metastable states are of particular interest for plasma modeling.

A few spectral lines could not be linked to a specific Sn ion. These lines turned out to have only a weak dependence on the electron beam energy. They originate most likely from residual gas or W or Ba ions stemming from the cathode as they remained visible without Sn injection.

Line identification

The wavelengths and intensities of the spectral lines for each identified charge state were extracted at the acceleration potential that maximized its fluorescence intensity (see Figs. 1.3, 1.5). Listed in Table 1.1 are the centers of the lines, as obtained by fitting Gaussian functions to them. The uncertainty in the determination of the transition wavelengths is dominated by the uncertainty in the spectrometer calibration. Due to a relatively weak signal, the Sn^{11+}–Sn^{14+} spectra were acquired using a wider entrance slit than needed for the calibration source to reach a sufficient fluorescence intensity. This enlarged the influence of

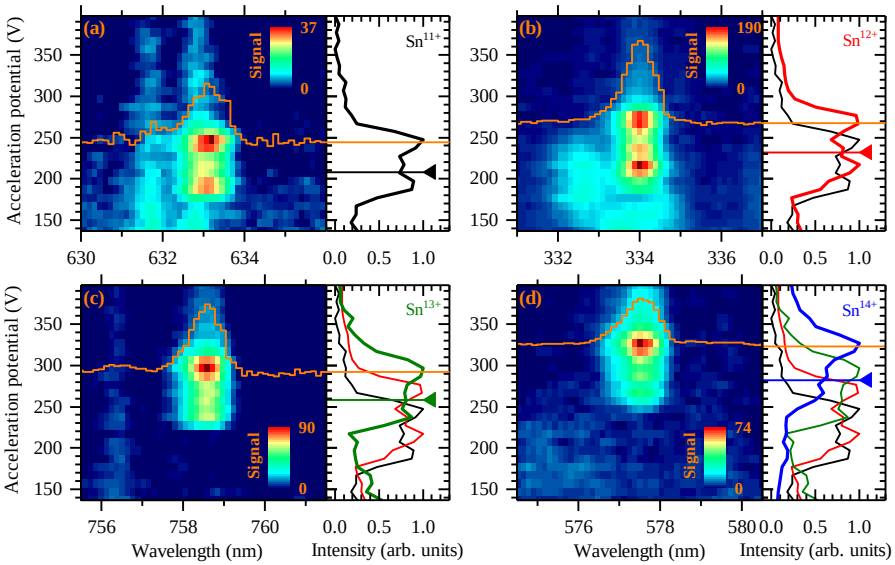

FIGURE 1.3 Enlarged sections around the spectral lines marked (a), (b), (c), and (d) in Fig. 1.2 assigned to the charge states Sn^{11+}, Sn^{12+}, Sn^{13+}, and Sn^{14+}. On the right hand side of the composite spectral maps we show the respective projection onto the acceleration potential axis as black (Sn^{11+}), red (Sn^{12+}), green (Sn^{13+}), and blue (Sn^{14+}) curves. Theoretical ionization energies of the charge states [62, 63] are depicted by triangles and colored accordingly. The profiles were averaged over several bright spectral lines exhibiting the same voltage dependence. By combining the obtained profiles, as shown in (d), a "ladder" was constructed which enabled the charge state identification of spectral lines (see main text). The overlaid orange spectra (also see Fig. 1.2) are obtained at the acceleration potential that maximizes the fluorescence yield.

TABLE 1.1 Vacuum wavelengths and relative intensities for spectral lines of Sn^{11+}–Sn^{14+} ions measured at the EBIT acceleration potential V_{max} that yielded maximum fluorescence. The experimental wavelength uncertainty of ∼0.4 nm is mainly due to the uncertainty in the calibration. All observed lines could be identified for $Sn^{11,12,14+}$. Our identifications were further confirmed with Ritz combinations where available (see Fig. 1.1); lines involved in Ritz combination groups are indicated by the letters ^{a,b,c,d,e,f}. Lines near 328 nm and 368 nm wavelength, now associated with Sn^{10+}, show signs of weak, blended contributions of Sn^{11+}, but their unambiguous identification is left for future work. Intensities were derived from the total area of the Gaussian fit, and were corrected for the grating efficiency. Theoretical wavelengths λ_{FSCC} were obtained from FSCC. Wavelengths obtained from semi-empirical Cowan code calculations are marked λ_{Cowan} and the associated weighted transition rates $gA_{ij,\mathrm{Cowan}}$ are given. "Transition" gives lower and upper state contributing to transition (from Fig. 1.1), with their respective configuration and (approximate) term given in the last two columns.

Ion	V_{max} (V)	λ_{exp} (nm)	Intensity (arb. units)	λ_{FSCC} (nm)	λ_{Cowan} (nm)	$gA_{ij,\mathrm{Cowan}}$ (s^{-1})	Transition (see Fig. 1.1)	Configuration	Term symbol
11+	247	275.6[a]	8		276	102	0-9	[Kr] $4d^3$	$^4F_{3/2}$-$^2D_{3/2}$
		291.2[b,c]	14		292	100	2-13		$^4F_{7/2}$-$^2G_{9/2}$
		297.8	23		297	308	2-12		$^4F_{7/2}$-$^2D_{5/2}$
		339.5[d]	34		341	79	3-13		$^4F_{9/2}$-$^2G_{9/2}$
		364.2	44		365	48	6-16		$^2G_{7/2}$-$^2F_{5/2}$
		378.9	81		379	59	3-11		$^4F_{9/2}$-$^2H_{11/2}$
		412.4	136		412	253	1-6		$^4F_{5/2}$-$^2G_{7/2}$
		467.5[a]	39		468	55	0-4		$^4F_{3/2}$-$^4P_{3/2}$
		503.0[c]	129		503	165	2-8		$^4F_{7/2}$-$^2H_{9/2}$
		538.7[b]	75		539	125	2-6		$^4F_{7/2}$-$^2G_{7/2}$
		633.3[b]	178		637	268	6-13		$^2G_{7/2}$-$^2G_{9/2}$
		638.1	53		640	17	1-4		$^4F_{5/2}$-$^4P_{3/2}$
		668.5[d]	143		668	211	3-8		$^4F_{9/2}$-$^2H_{9/2}$
		671.5[a]	51		674	139	4-9		$^4P_{3/2}$-$^2D_{3/2}$
		690.7[c,d]	92		695	267	8-13		$^2H_{9/2}$-$^2G_{9/2}$
12+	267	334.1	247	337	334	290	1-7	[Kr] $4d^2$	$^3F_3$-$^1G_4$
		341.8[e]	65	335	342	87	1-6		$^3F_3$-$^3P_2$
		402.6	122	396	402	117	0-4		$^3F_2$-$^1D_2$
		472.7	185	478	471	162	2-7		$^3F_4$-$^1G_4$
		665.0[e]	63	643	658	36	1-4		$^3F_3$-$^1D_2$
		703.9[e]	167	698	712	151	4-6		$^1D_2$-$^3P_2$
13+	297	285.2	11						
		318.5	19						
		356.5	62						
		391.9	17						
		525.6	24						
		758.8	518	763	757	150	0-1	[Kr] $4d^1$	$^2D_{3/2}$-$^2D_{5/2}$
14+	327	297.9[f]	211	292	295	984	3-7	$4p^5\,4d^1$	$^3P_2$-$^3D_3$
		302.9	15	308	302	2597	8-10		$^3D_1$-$^3D_2$
		316.3	109	308	311	516	4-7		$^3F_3$-$^3D_3$
		330.2[f]	20	331	319	62	2-6		$^3P_1$-$^1D_2$
		485.1[f]	51	465	503	80	6-7		$^1D_2$-$^3D_3$
		577.7[f]	207	571	575	349	2-3		$^3P_1$-$^3P_2$

TABLE 1.2 Cowan code Hartree-Fock (HFR) and fitted (FIT) parameters (with uncertainties $\delta_{\rm fit}$), their ratios (scaling factors), and root mean square deviations σ of the fits as calculated for the $4d^k + 4d^{k-1}\,5s + 4d^{k-2}\,5s^2$ interacting configurations ($k = 3, 2$ respectively in the Sn^{11+} and Sn^{12+} spectra). The electrostatic parameters were scaled by a factor 0.85 whereas average energies and spin-orbit parameters were not scaled in the unknown $4d^{k-1}\,5s$ and $4d^{k-2}\,5s^2$ configurations. All parameters are given in units of cm^{-1}.

Parameter	Sn^{11+}				Sn^{12+}			
	HFR	FIT	$\delta_{\rm fit}$	FIT/HFR	HFR	FIT	$\delta_{\rm fit}$	FIT/HFR
E_{av}	41 025	37 533	17		26 035	24 435	2	
$F^2(4d,4d)$	114 058	97 715	121	0.857	116 377	99 790	21	0.857
$F^4(4d,4d)$	76 975	68 047	323	0.884	78 692	69 026	270	0.877
α	-	64	3		-	68	1	
β	-	-600	fixed		-	-600	fixed	
$T1$	-	-4.4	fixed		-			
$\zeta(4d)$	4 638	4 774	16	1.029	4 868	5 028	2	1.033
σ		57				4		

any minor misalignments of the two light paths resulting in a systematic uncertainty estimated at ∼0.4 nm. We obtained this uncertainty by comparing spectral lines in the overlap region of different wavelength ranges. Also listed are the signal intensities given by the area under the fitted Gaussian curves, corrected for the spectral grating efficiency. The accuracy of this procedure is limited, and uncertainties in the determination of the total signal are further introduced by chromatic aberrations of the coupling optics, the finite aperture width, and polarization effects. However, this accuracy should be higher when comparing the relative intensities of transitions with close-lying wavelengths.

Accurate experimentally obtained spectra in the EUV regime are available for the charge states Sn^{7+} [33], Sn^{8+}–Sn^{11+} [32], Sn^{13+} [35], and $Sn^{12,13,14+}$ [34]. Transitions in the higher charge states were measured by D'Arcy and coworkers [45, 46]. We focus our discussion on the charge states Sn^{11+}–Sn^{14+}. As pointed out previously [58], the identification of weak EUV lines needs to be corrected in previous works. Nevertheless, we will start out by comparing our results to the reference data as is, except in the case of Sn^{12+} for which a new interpretation based on existing EUV spectral data is presented here. Further, a direct comparison is made to the FSCC calculations. In the following the results per charge state are discussed in detail.

TABLE 1.3 (Caption on the following page).

Ion	Level	Term	Experiment				FSCC			E_{Cowan}	E_{vs}	ΔE_{vs}
			E_{exp}	D_1	D_2	N	$\Delta E_{\mathrm{Breit}}$	ΔE_{LS}	E_{FSCC}			
11+ $4d^3$	0	$^4F_{3/2}$	0	17	0	2				0	0	0
	1	$^4F_{5/2}$	5 719	9	20	2				5 758	5 760	-36
	2	$^4F_{7/2}$	11 403	10	30	3				11 445	11 465	-57
	3	$^4F_{9/2}$	16 321	9	30	2				16 375	16 390	-64
	4	$^4P_{3/2}$	21 391	6	17	3				21 390	20 486	905
	5	$^4P_{1/2}$								23 341		
	6	$^2G_{7/2}$	29 967	8	30	3				30 011	30 057	-84
	7	$^4P_{5/2}$								31 130		
	8	$^2H_{9/2}$	31 280	6	30	3				31 337	31 110	175
	9	$^2D_{3/2}$	36 283	9	19	2				36 216	35 810	471
	10	$^4P_{1/2}$								38 736		
	11	$^2H_{11/2}$	42 713	28	44	1				42 726	42 230	488
	12	$^2D_{5/2}$	44 983	45	56	1				45 081	44 990	-2
	13	$^2G_{9/2}$	45 759	6	30	4				45 720	45 705	59
	14	$^2P_{3/2}$								51 365		
	15	$^2F_{7/2}$								57 261	55 460	
	16	$^2F_{5/2}$	57 425	30	43	1				57 414	55 660	1 770
12+ $4d^2$	0	$^3F_2$	0	25	0	1	0	0	0	0	0	0
	1	$^3F_3$	9 786	9	30	2	-374	29	9 738	9 780	9 745	41
	2	$^3F_4$	18 564	18	50	1	-655	57	18 507	18 563	18 480	84
	3	$^3P_0$					-87	0	23 642	22 649		
	4	$^1D_2$	24 838	6	25	2	-355	29	25 285	24 835	24 320	518
	5	$^3P_1$					-238	29	28 750	27 905		
	6	$^3P_2$	39 044	8	30	2	-425	57	39 636	39 042	38 370	674
	7	$^1G_4$	39 718	36	44	1	-983	29	39 381	39 715	38 830	888
	8	$^1S_0$					-381	57	83 202	80 700		
13+ $4d^1$	0	$^2D_{3/2}$	0				0	0	0	0	0	0
	1	$^2D_{5/2}$	13 179				-439	30	13 144	12 740	13 212	-33
14+ $4p^6$	0	$^1S_0$					0	0	-540 785	-539 447		
$4p^5\,4d^1$	1	$^3P_0$					-870	-128	-8 962	-8 970		
	2	$^3P_1$	0	11	0	2	-1 054	-128	0	0		
	3	$^3P_2$	17 311	12	12	2	-1 262	-97	17 544	17 392		
	4	$^3F_3$	19 275	40	50	1	-1 048	-128	19 247	19 115		
	5	$^3F_4$					-1 464	-97	21 027	20 991		
	6	$^1D_2$	30 278	16	30	2	-1 197	-128	30 252	31 345		
	7	$^3D_3$	50 891	16	30	2	-1 410	-97	51 770	51 208		
	8	$^3D_1$					-1 535	12	76 730	77 445		
	9	$^3F_2$					-1 996	12	91 543	93 484		
	10	$^3D_2$					-2 348	46	109 202	110 507		
	11	$^1F_3$					-2 445	46	117 668	118 362		
	12	$^1P_1$					-1 853	12	209 573	222 563		

TABLE 1.3 (Table on the previous page) Energy levels $E_{\rm exp}$ (all energies in cm^{-1}) derived from the experimental data using Kramida's LOPT algorithm [73], *ab initio* FSCC calculations $E_{\rm FSCC}$ (including individual contributions from the Breit interaction $\Delta E_{\rm Breit}$ and Lamb shift $\Delta E_{\rm LS}$) as well as semi-empirical Cowan code calculations $E_{\rm Cowan}$ of the investigated fine-structure configurations in Sn^{11+}–Sn^{14+}. Levels (from Fig. 1.1) are ordered by their energies; we use *LS*-term notations as approximated from the Cowan code. The dispersive energy uncertainty D_1 is close to the minimum uncertainty of separation from other levels, and the energy uncertainty D_2 is that relative to the ground level (or to the $^3P_1$ level in Sn^{14+} which is offset to zero $E_{\rm FSCC}$ and $E_{\rm Cowan}$ in this Table; $\Delta E_{\rm Breit}$ and $\Delta E_{\rm LS}$ are given with respect to the ground level $^1S_0$); see the exact definition in [73]. The number of spectral lines used for the determination of each level energy is given by N. Semi-empirical Cowan code calculations are given in column $E_{\rm Cowan}$. The identification of spectral lines in Sn^{11+} and Sn^{12+} used an iterative fit procedure based on the measured spectra (see Section 1.3, Table 1.2); for Sn^{13+} the value for $E_{\rm Cowan}$ was obtained from a single configuration HFR; and for Sn^{14+} the ratio FIT/HFR of Cowan parameters was determined by isoelectronic extrapolations and data from [42] (see main text). Energies deduced from vacuum-spark EUV spectra $E_{\rm vs}$ have uncertainties of $\sim$40 cm^{-1} [32, 34]. The difference $\Delta E_{\rm vs} = E_{\rm exp} - E_{\rm vs}$ of that interpretation with our own identifications suggests the need for revision of those earlier identifications.

Sn^{11+}

First identifications of transitions within the [Kr] $4d^3$ ground state were obtained from a comparison of the observed energies to the transition energies resulting from the semi-empirical Cowan energy parameters as obtained from Ref. [32]. We associated the predicted transitions of high gA values with the closest-lying, brightest spectral lines (see Fig. 1.5). In this manner, enough levels were identified to enable a fit of the calculations to these levels, improving on the original predictions. This in turn enabled the further identification of observed lines. Iterating the above procedure, all lines attributed to the Sn^{11+} spectrum were identified (see Table 1.1). In the final step, the obtained energies of the levels were optimized employing Kramida's code LOPT (for Level Optimization) [73]. The energy levels thus derived from the experimental wavelengths are collected in Table 1.3. A comparison of the energy parameters is presented in Table 1.2: on the one hand those obtained from *ab initio* HFR calculations, and on the other hand those obtained from fitting the Cowan code to the experimental level values obtained from LOPT. The effective parameters β and T1 were fixed in the fitting on the values roughly estimated from the isoelectronic spectrum of

Pd^{7+} [74] and the isonuclear spectrum of Sn^{7+} [40].

Many of the identified levels are connected by Ritz combinations within the experimental uncertainty (red arrows in Fig. 1.1), enabling the sensitive verification of our $M1$ line identifications. Transitions shown by black arrows in Fig. 1.1 are not supported by Ritz combinations but there is no obvious other choice for their identification. The branching ratios obtained from the signal intensities can be compared to the gA predictions from the Cowan code. Agreement is found within a factor of two except for short wavelength lines at 275.6 and 291.2 nm, as is to be expected taking into account the experimental uncertainties including those related to the drop of spectrometer efficiency at short wavelengths.

The last column of Table 1.3 shows the differences between the level energies obtained in this work and those from the study of the EUV spectrum in Ref. [32]. The magnitude of the differences indicates that the analysis of EUV transitions in Ref. [32] needs to be revised.

Sn^{12+}

We find a very good agreement of our *ab initio* FSCC predictions with the experimental data for the five relatively strong transitions found in this work. In order to confirm this outcome, we compare them with earlier work.

All levels of the $4d^2$ ground configuration of Sn^{12+} were obtained previously in the analysis of EUV lines in discharge spectra [34]. Subsequent studies of the spectra of the Rh^{7+}, Pd^{8+}, Ag^{9+} and Cd^{10+} ions from the Sn^{12+} isoelectronic sequence and the extrapolation of the isoelectronic regularities to Sn^{12+} showed [58], however, that the analysis in Ref. [34] of Sn^{12+} should be corrected.

In Fig. 1.6, the ratios of the energy parameters obtained from fits (FIT) and the *ab initio* Hartree-Fock values (HFR) of the electrostatic and spin-orbit parameters for the [Kr] $4d^2$ configuration in the aforementioned isoelectronic sequence [58] are shown. The points for Sn^{12+} were obtained by linear extrapolation of the data. The thus obtained scaling factors for the electrostatic parameter F^4 and for the spin-orbit parameter, respectively 0.897 and 1.027, are in close agreement with the values 0.900 and 1.030 obtained in Ref. [34]. However, the scaling factor for the electrostatic parameter F^2, at 0.850, disagrees with the value of 0.829 from Ref. [34]. The initial Cowan code calculations of energy levels, wavelengths, and transition probabilities for $M1$ transitions in this work were performed using the empirical scaling factors obtained from the mentioned extrapolation and taking $\alpha = 55$. These prior parameters enabled an accurate prediction of the Sn^{12+} level energies and enabled also the identification of all observed lines for this charge state. This strengthens our assignments of *ab initio* FSCC results to the observed transitions. The branching ratios of the intensity I of the identified transitions I(4-6) and I(1-6), as well as I(1-7) and

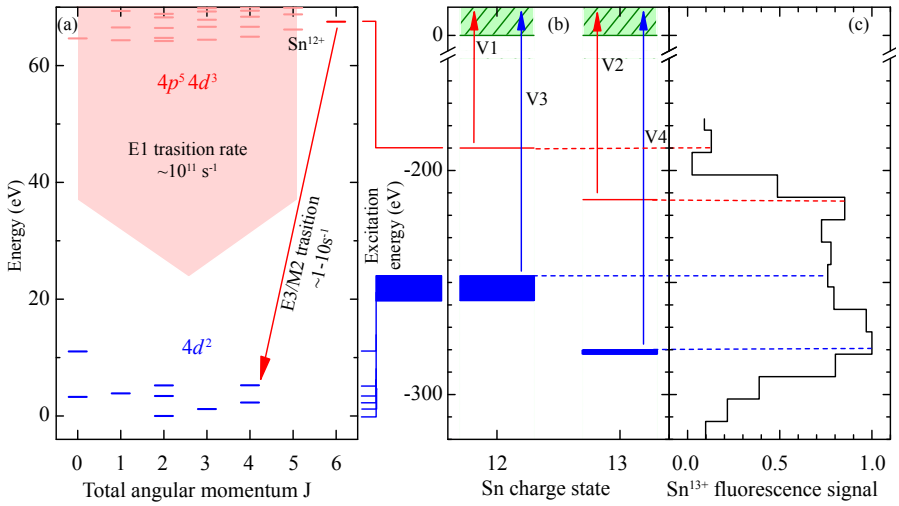

FIGURE 1.4 Effect of metastable states on the in-EBIT production and fluorescence of Sn^{13+} from the ionization step $Sn^{12+} \rightarrow Sn^{13+}$. (a) Grotrian diagram of Sn^{12+}. States in the excited $4p^5\,4d^3$ and $4p^6\,4d^1\,4f^1$ configurations (light red) with total angular momenta $J \leq 5$ decay to the ground state configuration $4p^6\,4d^2$ (blue) through fast $E1$ transitions. States with $J \geq 6$ are metastable (red) since all possible transitions require a change $\Delta J \geq 2$, and thus accumulate population. (b) The lowest such metastable states for Sn^{11}–Sn^{14+} ions are ∼60 eV closer to the continuum (green) than their ground states (blue). This allows ionization at an energy V1 that is lower than the corresponding ionization potential V3 for the ground state. Between V1 and V3, the value of V2 indicates the ionization threshold for metastable states of the fluorescing Sn^{13+} at which production of Sn^{14+} starts. For the Sn^{11}–Sn^{14+} ions, the difference in (ground state) ionization energies (∼30 eV) is roughly only half as large as typical metastable-state energies (∼60 eV). At the threshold V4, Sn^{13+} will be ionized from its ground state, and its population will decrease again. (c) The dependence of the Sn^{13+} fluorescence intensity (black curve) on the electron beam energy qualitatively follows this scenario. The electron beam energy (y-axis in (c)) has been shifted by -20 eV (compare Fig. 1.3) to account for the electron beam space charge potential.

I(2-7) (see Fig. 1.5) can be compared with predictions. The experimental ratio I(4-6)/I(1-6) = 2.6 is in agreement with the value 1.7 from the gA values obtained from Cowan calculations, given the uncertainty in the measurement of the total signal strength. Experimentally, we find I(1-7)/I(2-7)=1.3, compared to the 1.8 from Cowan's theory. One Ritz combination is found, further confirming our identifications of the lines involved. The energy levels of Sn^{12+} derived from the wavelengths of Table 1.1 and optimized with the LOPT [73] code are collected in Table 1.3. The magnitude of the differences between the here obtained energy levels and the previously available experimental data [34] indicates that the identification of EUV transitions in that work needs to be revisited.

A comparison of the energy parameters is presented in Table 1.2: those obtained from *ab initio* HFR calculations, and those obtained from the final fitting of the Cowan code to the experimental level values obtained from LOPT. The scaling factors for the Sn^{12+} energy parameters are in agreement with the extrapolated values within the uncertainty of extrapolation. The trends in the change of the scaling factors from Sn^{12+} to Sn^{11+} can be used in extrapolation to the spectrum of Sn^{10+} for a better prediction of its $M1$ transitions; this is part of future work.

Sn^{13+}

The *ab initio* FSCC calculations predicting a transition energy of 13 144 cm^{-1} for the $4d\,^2D_{3/2}$–$^2D_{5/2}$ fine structure splitting are in good agreement with the line measured at 758.8(4) nm wavelength, or 13 179(8) cm^{-1}. The data are also in excellent agreement with the result of 13 212(25) cm^{-1} given by Refs. [34, 35]. This allowed us to use this line for unequivocally identifying the Sn^{13+} charge state. After correcting for the grating efficiency, this line is by far the brightest one observed in our measurements. Features at shorter wavelengths having low intensities stem from transitions between excited, densely packed states within the [Ar] $3d^{10}\,4s^2\,4p^5\,4d^2$ configuration. Identification of these transitions is outside the scope of this work.

Sn^{14+}

The [Kr] ground state configuration $4p^6\,{}^1S_0$ does not exhibit a fine structure splitting and all contributions to the observed optical spectrum have to come from excited configurations, such as [Ar] $3d^{10}\,4s^2\,4p^5\,4d^1$. All levels of this configuration except the $J = 1$ levels are metastable for $E1$ transitions. The metastable states can thus decay and be observed through $M1$ fine structure transitions. Identification of the observed optical lines was performed with the aid of the FSCC and Cowan code calculations. For the latter ones the Slater F^k and

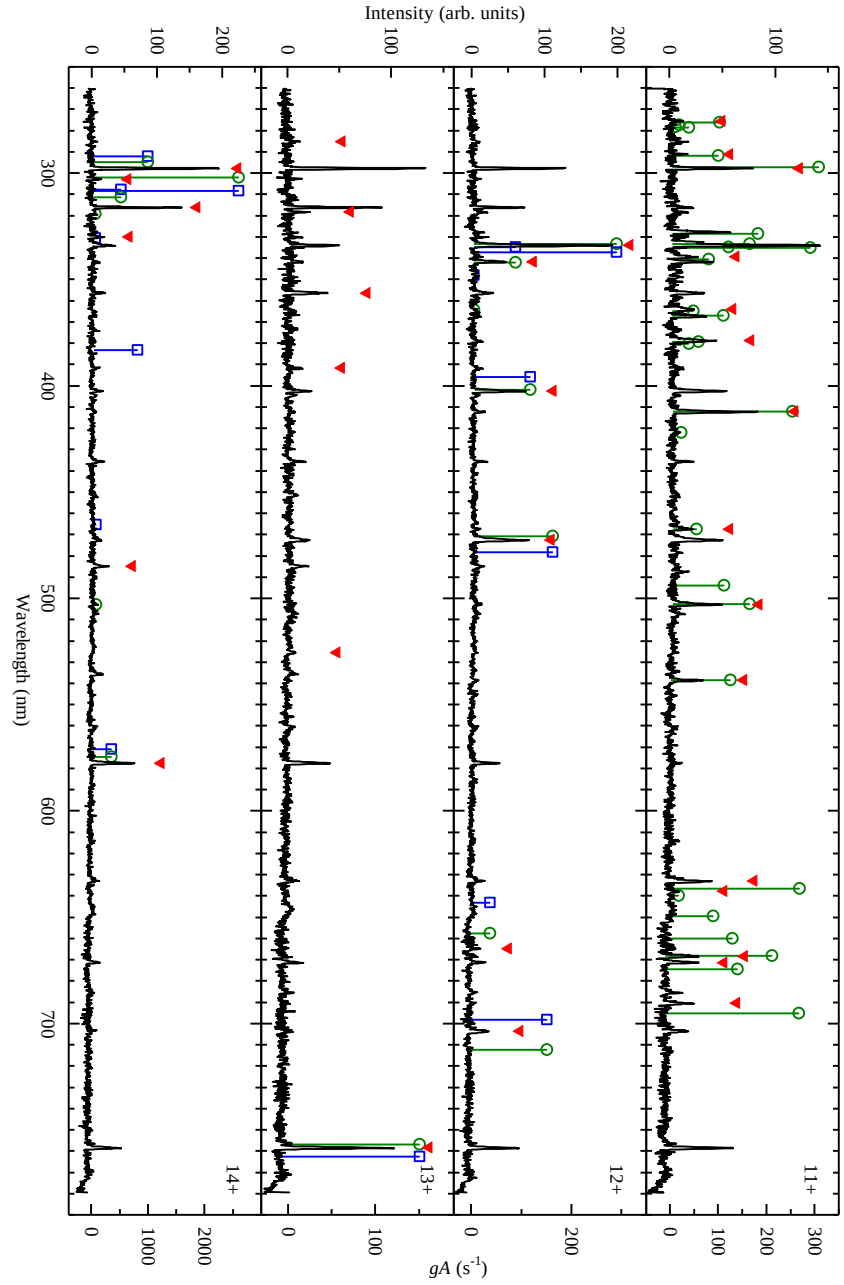

FIGURE 1.5 (Caption on the following page).

FIGURE 1.5 (Figure on the previous page) Spectra of the charge states Sn^{11+}–Sn^{14+} (orange lines in Fig. 1.2). Signal intensities here are not corrected for instrument sensitivity. Lines marked with red full triangles belong to the respective charge state. Blue open squares: FSCC predictions. Green circles: semi-empirical Cowan code calculations (see main text). The weighted transition rates gA are obtained from the Cowan code; they give a measure of the line strength of both theory predictions (right-hand y-axis).

G^k parameters were scaled down to 90% of their *ab initio* values. The spin-orbit parameters for the $4p$ and $4d$ electrons were scaled by the factors 1.024 and 1.03, respectively: for the $4p$ electron we took a value evaluated for the $4p^5$ configuration in Sn^{15+} [75]; the value for the $4d$ electron was extrapolated from the spectra of Sn^{7+} [40], Sn^{11+} (see the previous section) and Sn^{12+} [34]. Additionally, the average energy of the configuration was adjusted so that the $^3D_1$ value 616 892 cm^{-1} obtained in the previous experiment [42] was reproduced exactly. The results of the calculations are shown in Table 1.3 along with the results of the FSCC calculations. There is good agreement between the wavelengths calculated by these two methods. We used the gA coefficients as obtained from the Cowan code.

As before, if we associate each predicted transition with the closest-lying, brightest transition, we find that all observed lines can be identified (see Table 1.1). Moreover, if we now consider the fact that four of the transitions identified here form a Ritz group (see Fig. 1.1), we obtain a sensitive tool for checking our tentative assignments. Indeed, the assigned spectral lines form such a group well within the experimental uncertainty. The poor agreement between the experimental and theoretical branching ratio I(3-7)/I(6-7) could well be related to the poorer agreement between theory and experiment regarding the wavelengths of the assigned transitions. This discrepancy indicates an inaccurate determination of the involved wavefunctions and, hence, of gA coefficients. Furthermore, as discussed in the case of Sn^{11+}, experimental uncertainties in the determination of the signal intensity increase for short wavelengths like that of the 3-7 transition used in the comparison above.

The identification of the line at 316.3 nm is achieved considering that the branching ratio I(3-7)/I(4-7)≈2 fits best by assigning this line to the 4-7 transition. There appears to be no other choice for the weak line at 302.9 nm but the 8-10 transition even though the gA value for this transition is the largest of all predicted transitions. It should be noted that another predicted transition with large gA, namely 9-11, is absent from the spectrum. Both transitions start from high-lying levels and the apparent low intensities of the corresponding lines could be explained by a lower population of these levels. The experimental fine

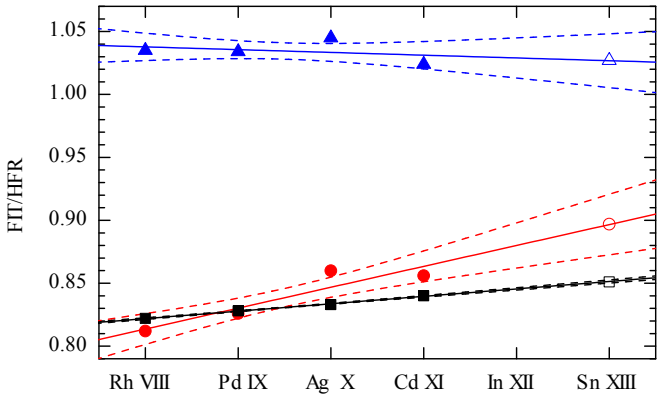

FIGURE 1.6 Empirical adjustments of scaling factors in the Cowan code calculations: The ratios (FIT/HFR) for the electrostatic parameters F^2 (black squares) and F^4 (red circles), and for the spin-orbit parameter ζ (blue triangles) were obtained by fitting (FIT) to available data [58] and *ab initio* (HFR) Cowan values of the [Kr] $4d^2$ configuration in Rh^{7+}...Cd^{10+}. Solid lines represent linear fits and their extrapolation to Sn^{12+} (open symbols). Dashed lines delimit their 1-σ confidence bands.

structure splittings $E_{\rm exp}$ of the $4p^5\,4d^1$ configuration, given in Table 1.3, were obtained by inserting the wavelengths of the transitions identified here into LOPT keeping the $^3P_1$ level fixed at the Hartree-Fock value. The agreement of *ab initio* FSCC and the semi-empirical Cowan results with experimental data in Table 1.3 is excellent. The *ab initio* FSCC method performs at the same level of accuracy as semi-empirical Cowan code that uses extensive input data. Furthermore, agreement of FSCC predictions of the energy of the levels 8 ($^3D_1$ at 617 515 cm^{-1}) and 12 ($^1P_1$ at 750 358 cm^{-1}) with previous experimental work in the EUV [42], which yielded 616 892 and 749 429 cm^{-1}, respectively, is outstanding.

Transitions in the EUV stemming from the configurations $4p^5\,4d^1$–$4p^5\,5p^1$ were observed previously [45]. In that work, several peaks in the recorded spectrum were assigned using Cowan code calculations but level energies were not derived because of poor resolution and strong overlap of the various lines. However, there are several cases when two EUV lines starting from the same $4p^5\,5p^1$ level were measured. Thereby, the separation between the $4p^5\,4d^1$ levels was found and compared to the levels given in Table 1.3. The splittings $^3P_2$–$^3D_3$ and $^3F_3$–$^1D_2$ are 33 600(1 500) and 11 100(1 500) cm^{-1}, respectively. Our values for these intervals, respectively 33 580(20) and 11 003(43) cm^{-1}, are in good

agreement. Therefore, the uncertainty of the relative wavelengths in [45] might be better than the quoted 0.02 nm, a finding that also supports our identification of the visible EBIT lines.

1.5 Conclusions

We have re-evaluated the fine structure of Sn^{11+}–Sn^{14+} ions, which are of particular interest for EUV plasma light sources used in next-generation nanolithography. Experimentally, we combined optical spectroscopy of magnetic dipole $M1$ transitions with charge-state selective ionization in an EBIT. The registered optical spectra were analyzed and line identifications were obtained based on *ab initio* FSCC calculations as well as semi-empirical Cowan code calculations that had adjustable parameters allowing us to fit the observed spectra. Both the FSCC calculations and the semi-empirical Cowan calculations showed a good agreement. The present measurements and identifications provide immediate input for optical plasma-diagnostic tools. Furthermore, our identifications of transitions confirm the very good predictive power of *ab initio* FSCC calculations. Given these encouraging results, it would be particularly advantageous if FSCC could be further developed, as in the current state of the code only atomic systems with a maximum of two open shell electrons/holes can be treated. Comparison of our results with previous work suggests that line identifications based on EUV data need to be revisited. In this type of complex correlated electronic systems, optical spectroscopy delivers data that both complements and challenges studies in the EUV regime and their interpretations.

CHAPTER TWO

OPTICAL SPECTROSCOPY OF COMPLEX OPEN-$4d$-SHELL IONS Sn^{7+}–Sn^{10+}

F. Torretti, A. Windberger, A. Ryabtsev, S. Dobrodey, H. Bekker, W. Ubachs, R. Hoekstra, E. V. Kahl, J. C. Berengut, J. R. Crespo López-Urrutia, and O. O. Versolato

Physical Review A **95**(4), 042503 (2017)

We analyze the complex level structure of ions with many-valence-electron open [Kr] $4d^m$ sub-shells (m=7–4) with *ab initio* calculations based on configuration-interaction many-body perturbation theory (CI+MBPT). Charge-state-resolved optical and extreme ultraviolet (EUV) spectra of Sn^{7+}–Sn^{10+} ions were obtained using an electron beam ion trap. Semi-empirical spectral fits carried out with the orthogonal parameters technique and Cowan code calculations lead to 90 identifications of magnetic-dipole transitions and the determination of 79 energy ground-configuration levels, questioning some earlier EUV-line assignments. Our results confirm the *ab initio* predictive power of CI+MBPT calculations for these complex electronic systems.

2.1 Introduction

The electronic structure [Kr] $4d^m$ (m=7–4) of the highly charged ions (HCI) Sn^{7+}–Sn^{10+} is extremely complicated due to the many electrons that occupy their open $4d$ sub-shell, and remains inaccessible to even some of the most advanced atomic theories. Furthermore, the unresolved transition arrays [76] formed by the Sn ions are particularly useful for the production of 13.5-nm-wavelength extreme ultraviolet (EUV) radiation for nanolithographic applications [38, 39, 77, 78]. Unfortunately, experimental assessments [32–37, 40–47, 79] of spectral data are hampered by the prevalence of strong configuration interaction contributions, and by a high density of states which approaches the quantum-chaos regime for high excitation energies [80–83]. In a recent study [79], we found evidence calling for a revision of earlier identifications [34, 35] in Sn^{11+}–Sn^{14+} ions having 3 to 0 electrons in their $4d$ sub-shell, and successfully demonstrated the suitability of Fock space coupled cluster (FSCC) calculations for systems with up to two valence electrons or holes. We now investigate other charge states relevant for the EUV production in plasmas, namely Sn^{7+}–Sn^{10+}.

We focus on optical spectroscopy in the present work, which can resolve the complex manifold fine-structure splittings of these ions. Therefore, the analysis of optical transitions in heavy multi-electron, open-shell ions enables the most stringent tests of *ab initio* atomic-structure calculations of strongly correlated systems with non-negligible many-electron Breit contributions. For such systems, a suitable theoretical tool is a combination of configuration interaction and many-body perturbation theory (CI+MBPT). The CI+MBPT method was first developed to very accurately treat neutral thallium as a three-valence-electron atom [84]. Since then, it has been markedly successful in treating also four- [85–88] and even five-valence-electron [89] systems. However, as the number of valence electrons increases, it becomes less accurate. A recent extension of the CI+MBPT method, used here, includes particle-hole interaction, and improves the accuracy of the calculations [90]. This makes it possible to treat systems with several vacancies which, e.g., are currently inaccessible to FSCC calculations.

We present charge-state-resolved optical and EUV spectral measurements of Sn^{7+}–Sn^{10+} ions trapped in an electron beam ion trap (EBIT), FLASH-EBIT [49], at the Max Planck Institute for Nuclear Physics (Max-Planck-Institut für Kernphysik, MPIK) in Heidelberg. EUV spectra were obtained simultaneously with the optical ones in order to identify the charge states and assign the optical lines to them. Then, we compare the Sn^{7+} data to the level structure accurately determined in Ref. [40], whereby a good agreement further validates our charge state assignments. Subsequently, we perform line and level identifications for Sn^{8+}–Sn^{10+} using semi-empirical calculations by employing the orthogonal pa-

rameters technique [91, 92] and the Cowan code [52]. The observed Ritz combinations strongly support our semi-empirical spectral analysis. Analogous to our recent work [79], we compare our experimental findings to previous level structure determinations from measurements of EUV spectra [32] and find noteworthy discrepancies. Armed with these experiment-fitted level structure, we test our state-of-the-art *ab initio* CI+MBPT calculations, and find them in very good agreement with the data. Both the important practical applications of the ions under study as well as the relative novelty of using CI+MBPT calculations for systems with such large numbers of valence electrons make our theory-experiment comparisons very valuable.

2.2 Experiment

Tin ions were produced and subsequently trapped and excited using FLASH-EBIT [49, 79]. In this device, the electron beam is compressed to a diameter of approximately 50 μm by the 6 T magnetic field generated by a pair of superconducting coils in Helmholtz configuration. Tin atoms were brought to the trapping region by injecting a tenuous molecular beam of tetra-i-propyltin ($C_{12}H_{28}Sn$), which dissociated while crossing the electron beam. Tin HCI were subsequently produced through electron impact ionization, while tuning the electron beam acceleration potential allowed the selection of the desired charge states. The heavier tin HCI were trapped longitudinally by the trapping potential created using a set of drift tubes and radially by the electron beam space-charge potential, while the lighter elements in the compound (C, H) escaped from the trap. Electron collisions populate levels close to the corresponding ionization continua and profusely induce fluorescence which was recorded by two instruments: a flat-field grating spectrometer and a Czerny-Turner spectrometer for EUV and optical emissions, respectively.

In the EUV spectrometer [61], light emitted by the trapped ion cloud is diffracted by a 1200 lines/mm flat-field, grazing-incidence grating [93] and recorded with a Peltier-cooled charge-coupled device (CCD) sensor. Calibration was performed using resolved bright lines of Sn in the 12–17 nm range, for which the wavelengths were known from Ref. [32], yielding a root-mean-square deviation of the calibration function residuals of 0.03 nm. Typical observed line widths are in the order of 0.04 nm, giving an experimental resolving power $\lambda/\delta\lambda$ of approximately 300 in the region near 13.5 nm.

In order to measure optical spectra, FLASH-EBIT is equipped with two in-vacuo and two in-air lenses imaging the ion cloud onto the entrance slit of a 320-mm-focal-length Czerny-Turner spectrometer equipped with a 300-lines/mm grating. For wavelength calibration Ne-Ar and Hg spectral lamps were used,

depending on the spectral region. They exhibited an instrument-dominated line width of approximately 1 nm at full-width at half-maximum (FWHM) around 400 nm. This setup, despite its relatively low resolving power compared to typical work of the MPIK group, is very convenient for quickly covering the whole optical range in these cases where no data were available.

A typical acquisition cycle consisted of a short calibration of the optical spectrometer, and a series of 30-minute-long simultaneous exposures of both the optical and EUV spectrometers. After each acquisition the electron beam acceleration potential was increased by 10 V, stepping from 137 V to 477 V at a constant beam current of 10 mA. This low current gives rise to a modest space-charge potential correction of approximately 25 V [61, 79]. The chosen range of the acceleration potential enabled the production of charge states from Sn^{7+} up to at least Sn^{14+} [79]. After each energy scan the grating was rotated to measure an adjacent wavelength range while keeping a certain overlap. Next, the acceleration potential was stepped through its entire range again. This procedure was performed thrice, encompassing the full accessible wavelength range from 260 to 780 nm. Gaussian fits were carried out to determine the centroid positions of the recorded lines. Associated error bars of approximately 0.4 nm are dominated by the calibration uncertainty [79]. Intensities are taken from the Gaussian fits and corrected for the grating efficiency.

2.3 Theory

Two calculation methods are presented in this work. First, we present dedicated *ab initio* CI+MBPT calculations performed with the AMBiT code, and benchmark them by comparison with our experimental data. Second, in order to identify the measured transitions and the associated energy levels we utilize semi-empirical calculations using orthogonal energy scaling parameters which can be tuned to fit the spectral data. We also use the Cowan code results on weighted transition rates gA to predict line strengths and branching ratios.

CI+MBPT

The detailed electronic structure of Sn^{7+}–Sn^{10+} was calculated using the AMBiT code which combines configuration interaction and many-body perturbation theory (CI+MBPT). Full details of this method have been presented previously [85, 89, 90]. Here we explain some of the physics and details relevant to the current calculations of tin ions. A more formal discussion, including mathematical details, may be found in Ref. [85]. Atomic units ($\hbar = m_e = e = 1$) are used in this section.

We start with a Dirac-Fock (relativistic Hartree-Fock) calculation in the V^N approximation. In this approximation all N electrons of the tin ion are included in the self-consistency procedure, creating a Dirac-Fock potential and electron orbitals that are optimized for the [Kr] $4d^m$ ground-state configuration. This is particularly important for this study because between m =4 and 7, the $4d$ orbitals pass through the half-filled sub-shell ($4d^5$), in which the exchange contribution is maximal. We will use Sn^{9+} (m = 5) as a working example in the following.

A large orbital basis is formed by diagonalizing a set of B-splines [94–96] over the Dirac-Fock operator

$$\hat{h}_{\mathrm{DF}} = c\,\boldsymbol{\alpha}\cdot\mathbf{p} + (\beta-1)m_e c^2 - \frac{Z}{r} + V^N(r). \tag{2.1}$$

The resulting basis is then ordered by energy. The lowest few valence orbitals in each wavefunction are close to their "spectroscopic" counterparts, while the higher energy orbitals, so-called pseudostates, include large contributions from the continuum.

We now form a set of many-body configurations for the CI method. The CI basis includes all configurations formed by allowing single and double excitations from the $4d^5$ ground-state configuration up to $8spdf$ orbitals (i.e. including $5s$ – $8s$, $5p$ – $8p$, $4d$ – $8d$, and $4f$ – $8f$ orbitals). The configurations included in CI are defined to be within a subspace here denoted P; all others are within its complementary subspace Q. For each configuration, a complete set of projections is generated, specifying the total angular momentum and projection of each electron in the configuration. These projections are diagonalized over the $\hat{J}^2$ operator to obtain configuration state functions (CSFs). The CSFs are diagonal in total angular momentum, projection, and relativistic configuration, and they form the CI basis which we denote $|I\rangle$. All CSFs corresponding to configurations in the subspace P are included in CI.

The many-electron wavefunction ψ is expressed as a linear combination of CSFs from the subspace P,

$$\psi = \sum_{I\in P} C_I\,|I\rangle\,,$$

where the C_I are obtained from the matrix eigenvalue problem. The Hamiltonian for the CI problem is

$$\hat{H} = E_{\mathrm{core}} + \sum_i \hat{h}_{\mathrm{CI}} + \sum_{i<j}\frac{1}{|\mathbf{r}_i-\mathbf{r}_j|}, \tag{2.2}$$

where the indices i and j run over the valence electrons only. Note that the one-body operator $\hat{h}_{\rm CI}$ is not equal to the Dirac-Fock operator: $\hat{h}_{\rm CI}$ has a potential term $V^{N_{\rm core}}$ due to the core electrons only. Therefore, the basis orbitals are not eigenvalues of the one-body CI operator, which must then be included explicitly.

Because the size of the CI matrix grows rapidly with the inclusion of additional orbitals, we must account for these configurations using many-body perturbation theory. The matrix-eigenvalue equation for the combined CI+MBPT method in second-order of perturbation theory is

$$\sum_{J\in P}\left(H_{IJ}+\sum_{M\in Q}\frac{\langle I|\,\hat{H}\,|M\rangle\,\langle M|\,\hat{H}\,|J\rangle}{E-E_M}\right)C_J=EC_I, \tag{2.3}$$

where the CSFs $|M\rangle$ belong to configurations outside of the subspace P. They are, in fact, in the subspace Q.

Because of the extremely large number of CSFs in the subspace Q, it is prohibitively expensive computationally to modify all matrix elements H_{IJ} directly. Instead, the CI+MBPT method includes Eq. (2.3) by modifying the radial integrals of the one and two-body matrix elements [84]. The Slater-Condon rules for calculating matrix elements of Slater determinants ensure that this is equivalent to Eq. (2.3), except for the energy denominator (for a detailed discussion beyond the scope of this work, see [84, 85, 97]). Because in this work $\hat{h}_{\rm DF}\neq\hat{h}_{\rm CI}$, so-called 'subtraction diagrams' must be included with terms proportional to $\hat{h}_{\rm CI}-\hat{h}_{\rm DF}$. These diagrams can become very large when there are many valence electrons since $V^{N_{\rm core}}-V^N$ is large, but there is cancellation between some of the largest subtraction diagrams and the three-body MBPT operator [89]. For this reason it is important to include three-body operators when calculating these tin ions. An alternative is to calculate the orbitals in the V^{N-m} approximation (equal to $V^{N_{\rm core}}$) as suggested in Ref. [98]; however, in this case the orbitals are much further from "spectroscopic", and the CI basis must be made considerably larger to correct them. In this work all one, two, and three-body second-order diagrams are included.

Until recently, only core-valence correlations were taken into account using MBPT. These correlations incorporate the effects of configurations $|M\rangle$, which include an excitation from the $N_{\rm core}$ electrons. It was shown in Ref. [90] that valence-valence correlations could also be included in the same manner. Thus, in the current work, valence-valence correlations with excited orbitals up to $30spdfg$ are included; this incorporates the effect of configurations that have one or two pseudo-orbitals above $8spdf$, but have no core excitations. Furthermore, for the first time, the valence-valence subtraction diagrams presented in

TABLE 2.1 Energy levels of the Sn^{9+} $4d^5$ configuration (in cm^{-1}) calculated by AMBiT CI+MBPT code. The first column give the approximate LS-term of the calculated energy levels. The CI values give the energy as calculated using only configuration interaction, while the Σ^{core}, Σ^{val}, Breit, and QED are the successive corrections to the CI energy by including core-valence MBPT, valence-valence MBPT, Breit, and QED contributions, respectively. The total energy including all corrections is also presented, as are the available experimentally determined values and the differences ΔE (Exp. - Total) (see main text).

	Energy (cm^{-1})							
Level	CI	Σ^{core}	$\Sigma^{val.}$	Breit	QED	Total	Exp	ΔE
$^6S_{5/2}$	0	0	0	0	0	0	0	0
$^4G_{5/2}$	39469	-4203	-2141	284	-28	33381	33784	403
$^4G_{7/2}$	42840	-4593	-1833	11	-2	36421	36874	453
$^4G_{11/2}$	43706	-4676	-1756	-132	3	37145	37535	390
$^4G_{9/2}$	44212	-4606	-1734	-120	7	37759	38170	411
$^4P_{5/2}$	43692	-3649	-2067	60	-4	38032	38315	283
$^4P_{3/2}$	44398	-3174	-2316	138	-12	39035	39190	155
$^4P_{1/2}$	47021	-2711	-2281	32	-1	42060		
$^4D_{7/2}$	51789	-4612	-2351	-98	8	44737	44915	178
$^4D_{5/2}$	55276	-3752	-2521	-106	10	48907		
$^4D_{1/2}$	55286	-3812	-2310	-190	22	48996		
$^4D_{3/2}$	56627	-3340	-2319	-241	25	50753		
$^2I_{11/2}$	62330	-7093	-2270	-110	5	52863	53692	829
$^2I_{13/2}$	65768	-7344	-2186	-318	18	55937	56792	855
$^4F_{7/2}$	66988	-5849	-3102	60	-9	58088	58487	399
$^2D_{5/2}$	65152	-3732	-2808	-150	18	58479	58756	277
$^4F_{3/2}$	65795	-4189	-3004	-17	4	58588	58891	303
$^4F_{9/2}$	67897	-5777	-3104	-33	-2	58981	59417	436
$^4F_{5/2}$	71298	-4933	-2901	-193	20	63291	63643	352
$^2H_{9/2}$	74999	-5532	-3005	-207	17	66273	66824	551
$^2G_{7/2}$	75308	-4572	-3146	-292	27	67325	67698	373
$^2D_{3/2}$	76386	-4767	-3007	-325	34	68321		
$^2F_{7/2}$	80012	-6786	-3048	-351	32	69859	70199	340
$^2F_{5/2}$	81165	-5771	-3713	-170	19	71529	71806	277
$^2H_{11/2}$	82714	-5812	-2746	-527	45	73674	74311	637
$^2F_{7/2}$	85363	-6347	-3651	-323	31	75073	75470	397
$^2G_{9/2}$	85188	-6283	-3135	-465	42	75347	75795	448
$^2F_{5/2}$	90363	-7289	-4328	-145	16	78616	78700	84
$^2S_{1/2}$	87288	-5338	-2910	-647	64	78457		
$^2D_{3/2}$	99595	-6555	-4503	-149	18	88405	88649	244
$^2D_{5/2}$	102913	-6472	-4465	-373	37	91640	91927	287
$^2G_{9/2}$	111086	-8615	-4736	-273	23	97485	98217	732
$^2G_{7/2}$	112328	-8403	-4689	-341	32	98927	99649	722

TABLE 2.2 Mean differences and standard deviation between our CI+MBPT calculations and experiment for measured transitions in different Sn ions (all this work).

Ion	Configuration	# of lines	$\Delta E_{\text{th-exp}}$ (eV)
Sn^{7+}	$4d^7$	8	-0.004 ± 0.013
Sn^{8+}	$4d^6$	24	-0.005 ± 0.023
Sn^{9+}	$4d^5$	30	-0.010 ± 0.026
Sn^{10+}	$4d^4$	28	-0.008 ± 0.034

Ref. [90] are also included. They vanished in that work because $\hat{h}_{\text{DF}}$ was the same as $\hat{h}_{\text{CI}}$, but play a role in the present context.

Finally, Breit and Lamb shift corrections are taken into account. The latter include the vacuum polarization (Uehling) [99] and self-energy [100] corrections in the radiative potential formulation of Flambaum and Ginges [101]. Because both of these effects arise from the electron density near the nucleus, they have a fairly constant ratio for all the levels we calculated.

The ion Sn^{9+} has a half-filled $4d$-shell, and for it the results are presented broken down into different contributions (Table 2.1). The MBPT corrections are separated into core-valence contributions, Σ^{core} (which correspond to unfreezing of the $4sp3d$ core), and valence-valence contributions, Σ^{val} (introduced in Ref. [90]), which account for configurations that include orbitals above $8spdf$. The column marked QED shows the vacuum polarization and self-energy corrections.

The Sn^{9+} and Sn^{10+} ions were treated with CI+MBPT calculations using only electron excitations (the approach of Refs. [84, 85]). However, as the number of valence electrons increases, this electron-only approach becomes inaccurate due to very large contributions from the subtraction diagrams. To avoid this inaccuracy, the particle-hole CI+MBPT calculations are instead used for the Sn^{7+} and Sn^{8+} ions. This approach, described in Ref. [90], places the Fermi level above the $4d$ shell and treats the $4d^{\text{m}}$ ground-state configuration as a corresponding number of valence holes in an otherwise filled shell. That is, the one-body CI operator includes the potential due to a completely filled $4d$ shell, $V^{N_{\text{core}}+10}$. Our complete CI+MBPT results for Sn^{7+} and Sn^{8+} in this particle-hole framework are presented in Tables 2.2, 2.3, 2.4, 2.5, and 2.6 together with the results for Sn^{9+} and Sn^{10+}.

TABLE 2.3 Energy levels of the ground configuration $4d^7$ for Sn^{7+} (all in cm^{-1}). The level energies E_{exp} were experimentally determined in Ref. [40] and are provided along with their approximate LS-term. $E_{CI+MBPT}$ are energy levels calculated by the AMBiT code. The difference between the two data sets $\Delta E_{CI+MBPT} = E_{exp} - E_{CI+MBPT}$ are presented in the last column.

Level	Term	E_{exp}	$E_{CI+MBPT}$	$\Delta E_{CI+MBPT}$
0	$^4F_{9/2}$	0	0	0
1	$^4F_{7/2}$	6986	6944	42
2	$^4F_{5/2}$	10341	10318	23
3	$^4F_{3/2}$	12153	12137	16
4	$^4P_{3/2}$	18280	18126	154
5	$^4P_{5/2}$	20373	20123	250
6	$^2G_{9/2}$	22636	22523	113
7	$^4P_{1/2}$	23946	23698	248
8	$^2G_{7/2}$	29001	28924	77
9	$^2H_{11/2}$	30312	30047	265
10	$^2P_{3/2}$	30657	30487	170
11	$^2D_{5/2}(3)$	33670	33762	-92
12	$^2P_{1/2}$	35458	35329	129
13	$^2H_{9/2}$	37751	37486	265
14	$^2D_{3/2}(3)$	44177	44051	126
15	$^2F_{5/2}$	45452	45083	369
16	$^2F_{7/2}$	49476	49087	389
17	$^2D_{3/2}(1)$	73321	71994	1327
18	$^2D_{5/2}(1)$	75377	75089	288

Orthogonal Energy Parameters

Line and level identifications in the Sn^{8+}–Sn^{10+} ions were performed using the *ab initio* MCDF (multiconfiguration Dirac-Fock) code [102], followed by semi-empirical calculations based on the orthogonal energy scaling parameters methods for the predictions of the energy levels. The orthogonal parameters method [92, 103] has several advantages in comparison with the more usual Slater-Condon approximation, as for instance used in the Cowan code [52]. Firstly, the energy parameters are maximally independent, facilitating the fitting of the radial integrals of the interactions to experimental energy levels. Secondly, it is possible to include an additional number of small interactions, such as two-particle magnetic and three- and four-particle electrostatic parameters. These qualities of the orthogonal parameters method, in general, improve the agreement be-

tween calculated and measured energy levels when sufficient experimental data are available to fit its parameters. This method has been shown to be apt even for complex electronic configurations, where configuration-interaction plays a relevant role [91]. For instance, it has been applied successfully in the identification of $4d^4$–$4d^3\,5p$ transitions in Pd^{6+} [104] reducing the standard deviation of the fits up to nine times compared to the Cowan code.

Prediction of the energy levels in the $4d^6$–$4d^4$ configuration in the Sn^{8+}–Sn^{10+} spectra was performed by interpolation of the energy parameters between Sn^{6+} ($4d^8$) [105,106], Sn^{7+} ($4d^7$) [40], Sn^{11+} ($4d^3$) [79], and Sn^{12+} ($4d^2$) [79]. These spectra were recalculated in the framework of the orthogonal parameters to determine the scaling parameters needed for the interpolation (see also subsection 2.4).

The transition probabilities of the magnetic dipole ($M1$) transitions were calculated using the Cowan code. In first approximation, the Cowan code energy levels were fitted to the energy levels predicted with the orthogonal parameters method to determine the level wavefunctions. The transition probabilities estimated with these wavefunctions were then used for the spectrum analyses and for the identification of the spectral lines. The energy levels established from the identified lines were optimized using Kramida's code LOPT [73]. The line uncertainty relevant for the optimization was taken to be 0.4 nm corresponding to $60\,cm^{-1}$ at 260 nm and $10\,cm^{-1}$ at 600 nm. The uncertainty was increased only for doubly classified (i.e. lines that can be ambiguously assigned to two transitions), blended or masked lines. Final transition probabilities were obtained after the fitting of the Cowan code to the experimentally established levels. The details of the identifications are given in the following section.

2.4 Results

In the following, we present optical and EUV spectra of tin ions in the resolved charge states Sn^{7+}–Sn^{10+} (see Figs. 2.1, 2.2, and 2.3). We interpret the data using orthogonal parameters and semi-empirical Cowan code calculations, delivering the most complete data set available to date for the ground configurations of Sn^{8+}–Sn^{10+} (with the semi-empirical results providing data also on level energies that were not directly probed experimentally). A detailed comparison of the thus obtained lines and levels with the CI+MBPT calculations is presented. Furthermore, we perform a comparison with energy levels available from existing data obtained in the EUV regime. We discuss first the charge state identification and second the line identifications. All results are summarized in Tables 2.2, 2.3, 2.4, 2.5, and 2.6. The result of line and level identifications is presented in the form of Grotrian diagrams in Fig. 2.4.

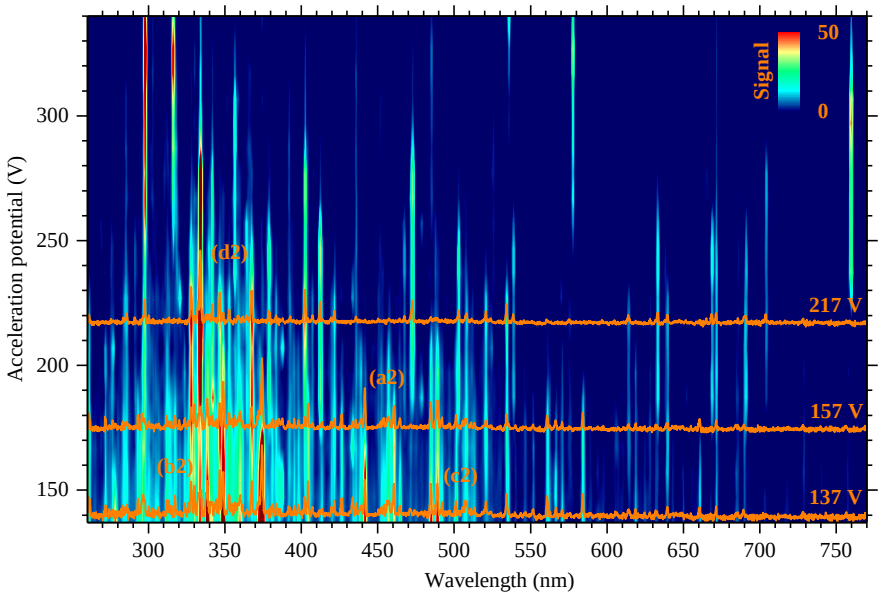

FIGURE 2.1 Spectral map of Sn ions in the optical regime obtained by interpolating discrete spectra acquired at different electron beam energies (uncorrected for space charge effects). The inset color map represents the fluorescence signal strength scale in arbitrary units. The projections highlight spectra at three acceleration potentials at which the fluorescence of a certain charge state is highest. The lines labeled with (a2), (b2), (c2), and (d2) are shown in more detail in Fig. 2.3, alongside with the features recorded in the EUV (Fig. 2.2) to assign the charge state.

Charge state identification

In an EBIT, charge state identification can be performed by evaluating the intensities of groups of spectral lines belonging to the same charge state as a function of the electron beam acceleration potential [61,70,79]. The doubly-peaked structure of the Sn^{10+} fluorescence curve (*cf.* Fig. 2.3), and its premature onset, has been previously observed in the optical domain for the charge states Sn^{11+}–Sn^{14+} [79]. This phenomenon was interpreted as being caused by the existence of strongly populated high-J metastable states. They act as stepping stones for reaching the next charge state at an energy below the corresponding ionization threshold, which is derived from the ground state binding energy. Moreover, as in Ref. [79], we observe that the onset of charge breeding of Sn^{8+} and Sn^{9+} takes

place well before the respective ionization potentials are reached. Once again, this is a signature of the presence of metastable states.

In this work, the charge state identification was somewhat hampered due to the low-energy onset of the charge states Sn^{7+}, Sn^{8+}, and Sn^{9+}, which could not be clearly discerned in the optical data. Therefore, we relied on simultaneously obtained charge-state-resolved EUV spectra to assign optical spectra to their respective charge states. The EUV spectra were compared to previously observed clusters of lines [32,33], as shown in Fig. 2.2. These lines stem from transitions to the ground configurations [Kr] $4d^m$ (m=7–4) from the $4p^6\,4d^{m-1}\,4f$+$4p^5\,4d^{m+1}$ excited electronic configurations. Four main features have been identified in the EUV spectra that could reliably be attributed to the charge states of interest. Therefore, tracking these features as a function of the electron beam acceleration potential and comparing them to their counterparts in the optical enabled the charge-state assignment, as shown in Fig. 2.3.

Line and energy level identification

Line wavelengths and intensities for each charge state were determined at the acceleration potential that maximized their yield by fitting Gaussians to the data. The intensities, given by the curve areas, were corrected for the grating spectral efficiency. Their uncertainties arise from statistics, as well as chromatic aberrations of the optical system and its finite aperture [79]. They are minimized when comparing close-lying wavelengths. The strong magnetic field of the EBIT could potentially influence the observed intensities as well. Firstly, this is because emission is polarized. However, since no polarizing optical element was employed, such possible effects are minimal and limited to small differences in the overall detection efficiency of the two polarizations. Secondly, anisotropic excitation of magnetic sublevels by the directed electron beam leads indeed to a differential population of electronic states, but the large number of cascades from highly excited levels feeding the upper states of the optical transitions under study leads to an almost complete depolarization of the emission lines. These effects have been studied in detail in the case of X-ray transitions with far less complex cascading networks populating their respective upper states [107–110], and should lead in the present cases to almost isotropic emission.

Listed in Tables 2.4 and 2.5 are their centers and integrated intensities obtained by Gaussian fits. A direct comparison to the CI+MBPT calculations is also displayed. Deviations from the experimental data are quantified by the mean difference and standard deviation between theory and experiment for all measured transitions (see Table 2.2). We find very good agreement with exper-

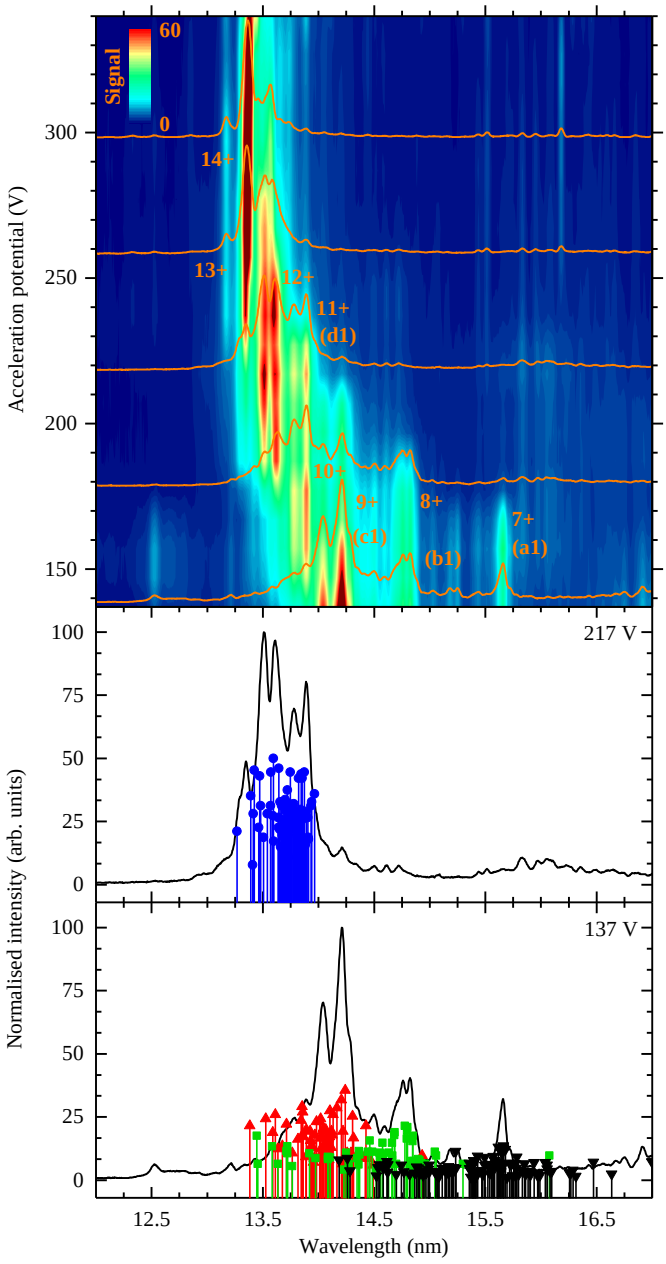

FIGURE 2.2 (Caption on the following page).

FIGURE 2.2 (Figure on the previous page) (Upper) Spectral map of Sn ions in the extreme ultraviolet obtained by interpolating discrete spectra acquired at 10 V acceleration potential steps starting from 137 V (uncorrected for space charge). The inset color map indicates the fluorescence strength scale in arbitrary units. The overlaid spectra are individually scaled for visibility and spaced by approximately 40 V, highlighting the onset of various spectral features. Labels (a1), (b1), (c1), and (d1) indicate features shown in detail in Fig. 2.3, where they are used for charge-state identification. (Lower) Spectra obtained at acceleration potentials 137 V and 217 V, individually normalized to 100 (arb. units). Scatter points represent transitions previously observed in a vacuum spark discharge [32, 33], arbitrarily scaled for visibility and to facilitate comparison (black inverted triangles: Sn^{7+}; green squares: Sn^{8+}; red triangles: Sn^{9+}; blue circles: Sn^{10+})[†].

iment for all Sn ions studied. In the following, the results per charge state are discussed in detail.

Spectrum of the Sn^{7+} ion

All levels of the $4d^7$ configuration in Sn^{7+} are known from the analysis of the $4d^7$–$4d^6\,5p$ transitions in the EUV region [40], with estimated uncertainties of less then 12 cm^{-1}. The position of the $M1$ optical transitions can be accurately obtained from the energy differences of these levels. Weighted transition rates gA for these $M1$ transitions were calculated by the Cowan code to facilitate the comparison, shown in Table 2.4, of the eight lines measured in this work with the energy levels in Ref. [40]. Most of the transitions that are predicted from the available structure [40] have a relatively small calculated gA value, and as such are not observable in our experiments. Three of the predicted stronger transitions (here taking $gA > 35\,s^{-1}$), at 372.1 nm ($^2F_{5/2}$-$^2D_{3/2}$), nearby 372.6 nm ($^2G_{9/2}$-$^2F_{7/2}$), and at 488.4 nm wavelength ($^2G_{7/2}$-$^2F_{7/2}$), were not reliably identified. In all three instances, this can be explained by line blending and by masking of such transitions by stronger emissions of the other charge states in the trap. The differences between our experimental wavelengths and wavelengths predicted from Ref. [40] are well within mutual uncertainties, which are dominated by the 0.4 nm uncertainty in our spectrometer calibration. Branching ratios cannot straightforwardly be used for comparison purposes, as the relevant observed transition sets (between levels 1-8/2-8, and 15-18/16-18, see Table 2.4

[†]It was found that the calibration of the EUV spectrometer was incorrect by 0.009 nm due to an incorrect line assignment in Ref. [34]. Regardless, this does not affect the results presented in any way.

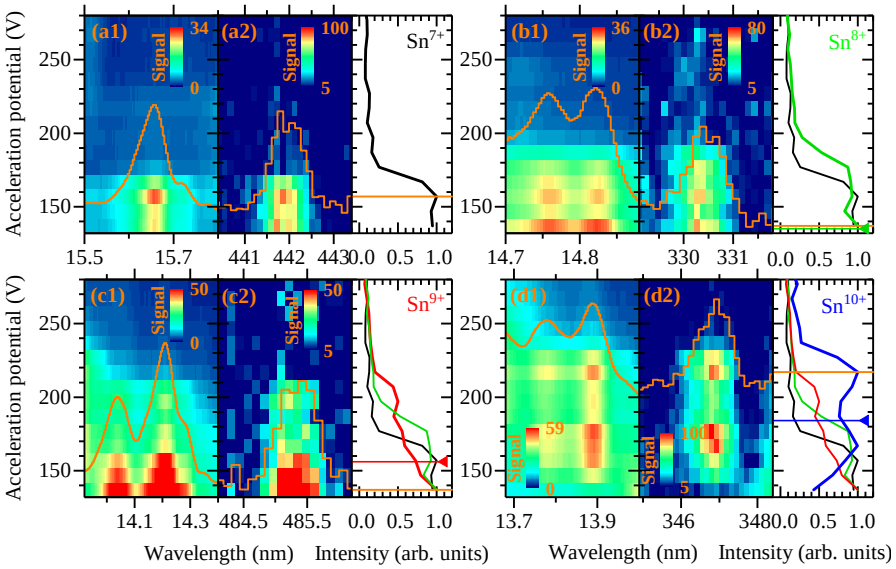

FIGURE 2.3 Enlarged view of selected features from Figs. 2.1 and 2.2. Independent color map scales for the fluorescence signal strength are given in arbitrary units. The fluorescence curves are determined by the averaged projections of all line intensities onto the acceleration potential axis of all the lines belonging to the same charge state, normalized to 1 at their respective maximum. Arrows indicate theoretical ionization potentials (Sn^{6+}: 113 eV, Sn^{7+}: 135 eV, Sn^{8+}: 156 eV, and Sn^{9+}: 184 eV [62, 63]). Vertical axes show acceleration potentials (not corrected for the space-charge contribution).

and Fig. 2.4) are affected by blends with neighboring lines. We do not experimentally re-investigate the $4d^7$ configuration in Sn^{7+} level structure, because of the limited number of lines here well resolved and the high-accuracy and detailed results available from Ref. [40]. The good agreement between the present data and previous experimental observations serves as further validation of our charge state identifications.

Spectrum of the Sn^{8+} ion

The list of the identified transitions between levels within the $4d^6$ configuration is presented in Table 2.5. In total, 22 spectral lines were uniquely identified. Of these, we found 17 levels connected to the ground $^5D_4$ level. Identification of nine levels is supported by observation of 11 Ritz combinations. The level

energies, optimized by LOPT [73], are presented in Table 2.6 with their respective uncertainties. The fitting of the orthogonal parameters was performed with these optimized levels. The resulting optimized sets of parameters are given in Table 2.7. The 354.8, 360.2, and 381.2 nm lines are isolated lines, i.e. the upper and lower levels of these lines are not involved in any other transition. Therefore, the lower levels of these isolated transitions were placed at the position as calculated with the orthogonal parameters method, with an estimated uncertainty of 16 cm^{-1} (one-standard-deviation value of the orthogonal parameters fit to the experimental values). These levels were not used in the parameter fitting procedure.

Most levels can be uniquely designated by the largest contributor in the LS-coupling decomposition of their wavefunctions. For example, the level labeled $^5D_3$ in Table 2.6 is composed of 97% $^5D_3$, 2% $^3F_3(2)$, and 1% $^3D_3$. Here, the number in brackets serves to distinguish between different LSJ-wavefunctions designated by the same LSJ values, supplementing a sequential index as defined by Nielson and Koster [111]. In this intermediate coupling regime, the choice of such a designating LS-term does not imply this term also provides the largest, or any at all, contribution to the transition magnetic dipole matrix elements. Indeed, some transitions occur that appear to violate $M1$ selection rules based on the chosen LS-term denomination, but nonetheless satisfy them since they arise from the admixture of other appropriate terms in the LS decomposition of both the upper and lower state wavefunctions.

Two exceptions to the naming convention explained in the previous paragraph are the $^1S_0(4)$ and $^3F_4(2)$ levels in the Sn^{8+} ground configuration, which we uniquely designate by the second-largest component of the wavefunction decomposition.

There are seven branched upper levels (numbered 6, 9, 11, 20, 21, 27, and 30 in Table 2.6, *cf.* Fig. 2.4). Most of the associated Cowan-calculated branching ratios are in reasonable agreement with the experimental data, except for lines affected by blends (such as in the ratios 9-21/11-21 and 0-9/1-9) or for short-wavelength transitions below 300 nm (featuring in the ratio 0-11/1-11 at 293.3 nm), the intensity of which are affected by a significant drop of detection efficiency. This reduction could not be assessed in our experimental setup.

The levels of Sn^{8+} found from EUV measurements on vacuum sparks [32] belong to four disjointed groups, where levels within a single group are connected to each other by measured lines but no transitions were identified connecting the different groups. The uncertainty of the level energies within each of the groups was estimated at 10 cm^{-1}, but between the groups as several 100 cm^{-1}. For this reason in Table 2.6, which contains comparison of the energies of these levels (E_{vs}) with our results (E_{exp}), the four groups are identified by their respective uncertainties z_i (i=1–4, as given in Ref. [32]). These

values should be interpreted as systematic common shifts, with respect to the ground state. Statistics of the differences $\Delta E_{\rm vs}$ (see Table 2.6) between previous identifications and the current experimental results provide a meaningful comparison between the two data sets. It is found that the two levels with shift z_1 are consistent with the present experimental values, with differences $\Delta E_{\rm vs}$ equaling -36 and $-22\,\mathrm{cm}^{-1}$, the scatter in which is well within the uncertainty of $16\,\mathrm{cm}^{-1}$ obtained from the orthogonal parameter fitting of the experimental data. In contrast, the average value of z_2 is found to be $270 \pm 377\,\mathrm{cm}^{-1}$, where the latter number represents the one-standard-deviation spread in the former. This large spread, compared to the experimental uncertainties (see Table 2.6), indicates that the respective levels from the previous work [32] are not consistent with the present experimental values and that the classification of EUV transitions therein requires a revision. The consistency of the remaining shifts for Sn^{8+}, z_3 and z_4, cannot be ascertained from our data.

Spectrum of the Sn^{9+} ion

Table 2.5 contains 28 identified lines between the levels of the $4d^5$ configuration in Sn^{9+}. Two lines, at 296.0 and 457.0 nm wavelength, are doubly classified. Measured intensities of branching ratios (from the ten upper levels numbered 15, 16, 19, 20, 22, 24, 26, 27, 31, and 32 in Table 2.6, *cf.* Fig. 2.4) are in reasonable agreement with the Cowan calculations, except for blended or doubly classified lines (affecting the transitions coupling levels 2-15, 2-19, 4-20, 12-24, and 8-27), and ultraviolet transitions (8-27, 3-24, and 4-24) due to the lower detection efficiency, similar to the identified Sn^{8+} lines. With the identified transitions, 24 levels connected to the ground $^6S_{5/2}$ level were established. Their values, optimized using LOPT [73], are listed in Table 2.6 with their respective uncertainties. The parameter fitting to the available levels resulted in an uncertainty of $41\,\mathrm{cm}^{-1}$ (one-standard-deviation of the fit). As in the case of Sn^{8+}, the majority of the levels can be uniquely designated by the largest component of the LS-coupling decomposition of the wavefunction. Four levels are named by the second-largest component. Only a single transition, at 399.9 nm wavelength, is found to be isolated. Thus, as before, the energy for the corresponding lower level $^4F_{5/2}$ was assumed to be equal to the value obtained from the orthogonal parameters method. These two isolated levels were not used in the parameter fitting. In addition to the agreement with the calculations, 15 levels are connected by transitions composing four Ritz combination chains, thus further supporting the identifications.

From the analysis of EUV vacuum spark observations [32], 21 levels of the $4d^5$ configuration were found as one group not connected to the ground $^6S_{5/2}$ level in the Sn^{9+} spectrum. The uncertainty of these levels relative to the ground

level was estimated as several $100\,\mathrm{cm}^{-1}$ common to the whole group, as indicated by the single value z_5 in Table 2.6. As in Sn^{8+}, the comparison between vacuum spark measurements and the current results allows to obtain information on the systematic uncertainty z_5. We find that the average value of this systematic shift is $460 \pm 422\,\mathrm{cm}^{-1}$, the one-standard-deviation spread of which exceeds the current uncertainty of $41\,\mathrm{cm}^{-1}$ by a factor ten, and therefore points to inconsistencies in the previous assignments. From the statistics of the differences ΔE_{vs} (see Table 2.6), we identify two groups of levels with common deviations 131 ± 10 and $197 \pm 13\,\mathrm{cm}^{-1}$. These groups comprise four (level numbers 3, 12, 13, and 24) and five levels (numbered 1, 4, 5, 6, and 14), respectively. However, the identification in Ref. [32] of more than half of the levels in the Sn^{9+} $4d^5$ configuration presents too large deviations ($\Delta E_{\mathrm{vs}} > 250\,\mathrm{cm}^{-1}$) from current values.

Spectrum of the Sn^{10+} ion

The list of 26 identified lines between the levels of the $4d^4$ configuration is presented in Table 2.5. Three of these (at 297.4, 328.1 and 614.1 nm wavelength) are doubly classified because they can be ambiguously assigned to two transitions. The measured intensities of the branched transitions (from upper levels 20, 21, 26, and 27 in Table 2.6, *cf.* Fig. 2.4) are in reasonable agreement with the Cowan code calculations except for the same two situations seen in the previous subsections: lines observed in the ultraviolet near the edge of the observable range, affecting the branching ratios related to the upper level 27; blending and double classifications which affect the transitions 15-21, 15-26, 16-26, and 18-27.

The level energies obtained from the analysis of the experimental spectra belong to two isolated groups. One group consists of 23 levels with the $^5D_1$ level being the lowest in energy. The remaining four levels numbered 2, 7, 9, and 22 form another group. Their relative energy values are optimized using LOPT [73] and are collected in Table 2.6. All of the found levels can be uniquely designated by the largest component of the LS-coupling decomposition of the wavefunction. The position of the two groups relative to the ground $^5D_0$ level could not be established from the present identifications. Thus, we assume the spacing between the $^5D_1$ and $^5D_0$ to be equal to the values obtained from the orthogonal parameters method, with a one-standard-deviation uncertainty of $14\,\mathrm{cm}^{-1}$ obtained from the fit. In a similar fashion, the value calculated employing the orthogonal parameters method was assigned to the lowest, $^5D_2$ level of the smaller group. The thus determined energy levels of these groups fall well within statistical uncertainties of the calculated values (*cf.* ΔE_{orth} in Table 2.6). However, they were not used in the fitting procedure to determine the energy parameters shown in Table 2.7.

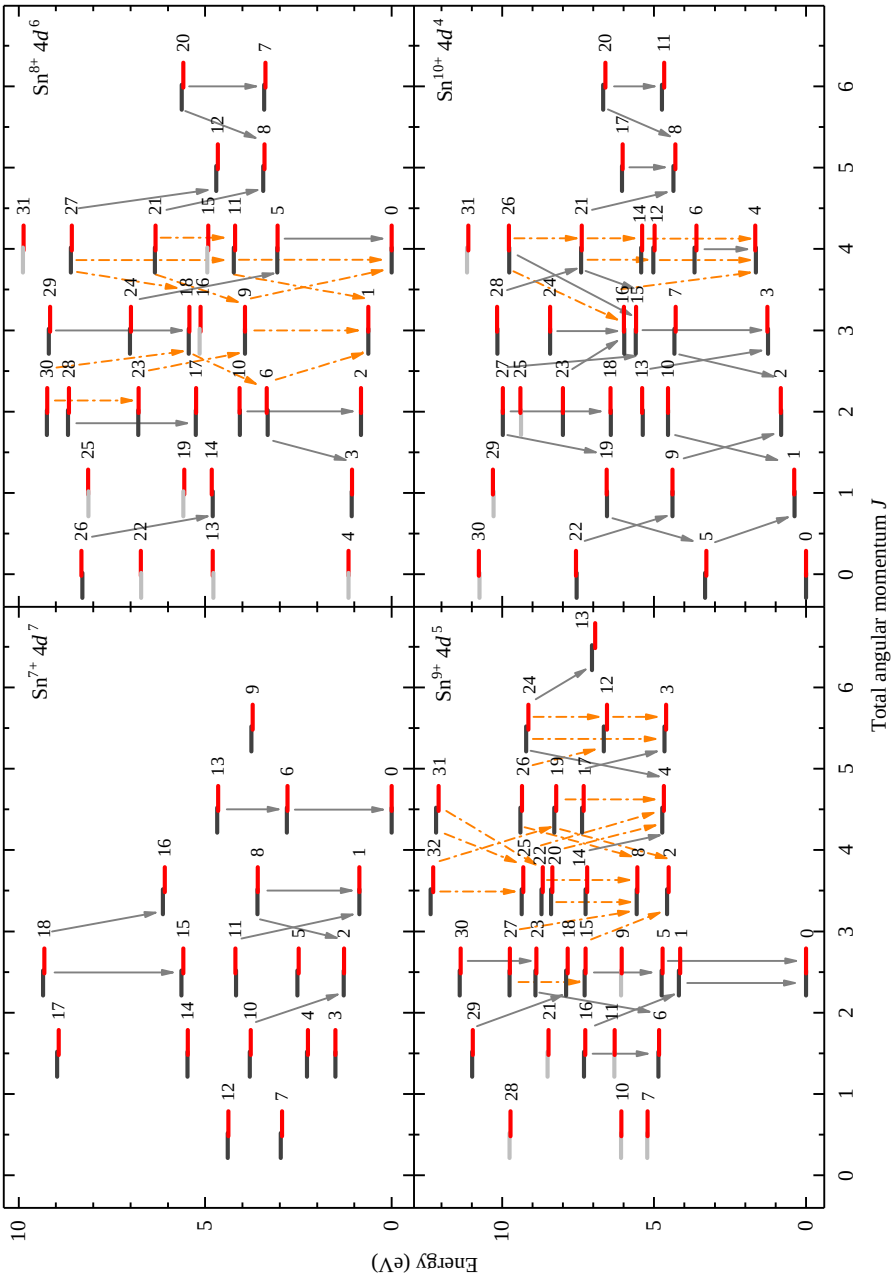

FIGURE 2.4 (Caption on the following page).

FIGURE 2.4 (Figure on the previous page) Grotrian diagrams for the ions Sn^{7+}–Sn^{10+}. The energy levels in dark grey (left) are determined experimentally, for Sn^{7+} they are taken from [40], whereas the Sn^{8+}–Sn^{10+} energy levels are results of this work (see Table 2.6). Light gray levels (left) in Sn^{8+}–Sn^{10+} could not be determined experimentally, and thus the values from orthogonal parameters calculations are used. Levels in red (right) are calculated with the AMBiT code. Arrows indicate experimentally observed optical transitions. Orange (dash-dotted) arrows indicate transitions which are part of one or more Ritz combinations.

The level energies thus obtained in this work can be compared to the levels established in Ref. [32] as determined from EUV spectra. The levels in that work form four isolated groups, three of which are not connected to the ground level. The uncertainties in relative positions of these three groups were estimated to be several 100 cm^{-1} [32], parameterized by the values $z_{6,7,8}$ in Table 2.6. Analogous to the cases of Sn^{8+} and Sn^{9+}, the differences $\Delta E_{\rm vs}$ are used to probe the agreement of our results with the previous analysis. We find average values for the shifts $z_6 = 339 \pm 95\,cm^{-1}$ and $z_7 = 383 \pm 43\,cm^{-1}$, when removing a single outlier in the latter group (level number 14). These one-standard-deviation values are reasonably consistent with the experimental uncertainties. Thus, our data support the identification of five levels with shift z_6 and seven levels of the z_7 group. The outlier, as well as the levels with shift z_8, show much larger discrepancies implying that affected energy levels in Ref. [32] are called into question.

Orthogonal scaling parameters

The orthogonal parameters for the isonuclear sequence Sn^{6+}–Sn^{12+} obtained from a fit to the experimental levels are collected in Table 2.7. Here, the orthogonal parameters $O2$, $O2'$, E'_a and E'_b are the orthogonal counterparts of the traditional Cowan parameters F^2, F^4, α and β [52,79]. The one-electron magnetic (spin-orbit) operator $\zeta(4d)$ and the effective three-particle electrostatic operators $T1$ and $T2$ are the same as in the Cowan code and (A_c-A_0) are additional two-particle magnetic parameters. The fitting was performed for the matrices of the interacting $4d^k$+$4d^{k-1}\,5s$+$4d^{k-2}\,5s^2$ configurations, k=8–2 for Sn^{6+}–Sn^{12+} respectively. The energy parameters of the unknown $4d^{k-1}\,5s$+$4d^{k-2}\,5s^2$ configurations therein were fixed at the MCDF-calculated values for the average energies and spin-orbit interactions. The corresponding electrostatic and configuration interaction parameters (the latter ones calculated by the Cowan code) were also kept fixed for the $4d^{k-1}\,5s$+$4d^{k-2}\,5s^2$ configurations, after scaling them by

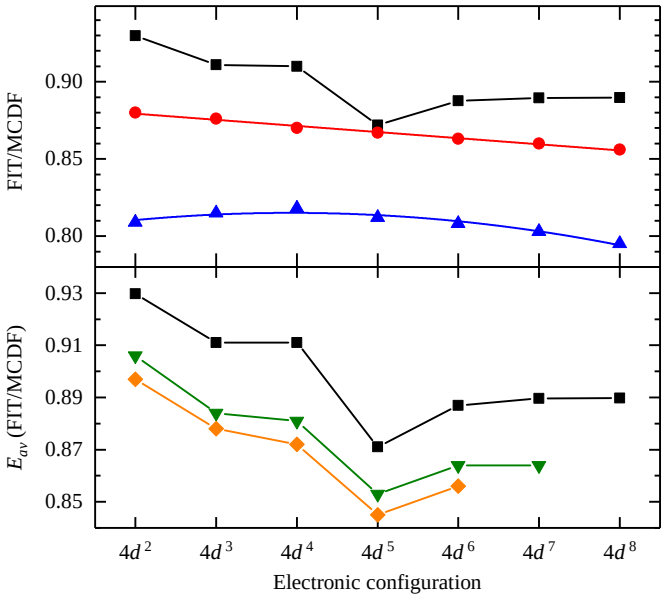

FIGURE 2.5 (upper) Empirical adjustments of scaling factors compared to the MCDF-calculated values: The ratios (FIT/MCDF) for the electrostatic parameters $O2$ (red circles) and $O2'$ (blue triangles), and for the average energy $E_{\rm av}$ (black squares) were obtained by fitting (FIT) to available data. Solid lines represent quadratic fits. (lower) Ratio of the semi-empirical final value (FIT) to the MCDF value for the average energy $E_{\rm av}$ along the isonuclear sequences of three elements: black squares Sn^{12+} to Sn^{6+}, green inverted triangles Ag^{9+} to Ag^{4+}, orange diamonds Pd^{8+} to Pd^{4+}.

0.85 from their *ab initio* values. The average energy $E_{\rm av}$ is defined such that the ground level energy of the $4d^k$+$4d^{k-1}\,5s$+$4d^{k-2}\,5s^2$ configurations is equal to zero. The two-particle magnetic parameters (A_c-A_0) were fixed to the MCDF-calculated values in all instances. For better stability of the fitting parameters, E_b' in Sn^{11+} and E_a' in Sn^{12+} were fixed to the extrapolated values.

Table 2.7 furthermore contains the ratios of the fitted parameters to the parameters obtained from MCDF calculations. Along the Sn^{6+}–Sn^{12+} isonuclear sequence the orthogonal energy parameters and the scaling factors can be approximated by linear or weak quadratic dependencies as is visible from Fig. 2.5 for the $O2$ and $O2'$ parameters. However, the scaling factor for the average energy presents a discontinuity going from the $4d^5$ to $4d^6$ configurations. Fig. 2.5 also shows that a similar dependence of the $E_{\rm av}$ scaling factors occurs in the Pd and

Ag isonuclear sequences. For comparison purposes, the ions Pd^{4+}–Pd^{8+} and Ag^{4+}–Ag^{9+} have been analyzed using the same orthogonal parameters method here used for Sn. The data were taken from Refs. [112] (Pd^{4+}), [113] (Pd^{5+}), [104] (Pd^{6+}), [74] (Pd^{7+}), [114] (Pd^{8+}, Ag^{9+}), [115] (Ag^{4+}), [116] (Ag^{5+}) and [74] (Ag^{6+}–Ag^{8+}). The three elements strikingly exhibit the same irregularity in scaling factors of the average energies for the configuration $4d^5$ (Sn^{9+}, Ag^{6+}, Pd^{5+}), which may be related to the fact that the $4d^5$ configuration is a half-filled shell. This physical phenomenon, resulting from the maximal exchange contribution in half-filled shells, yields for them a higher binding energy. It is also the cause for the often discussed and somewhat anomalous ground state configurations of the chemical elements Cr ($3d^5\,4s$), Mn ($3d^5\,4s^2$), Mo ($4d^5\,5s$), and Tc ($4d^5\,5s^2$), and analogously for Eu ($4f^7\,5s^2\,p^6\,6s^2$), Gd ($4f^7\,5s^2\,5p^6\,5d^1\,6s^2$), Am ($5f^7\,6s^2\,6p^6\,7s^2$) and Cm ($5f^7\,6s^2\,6p^6\,6d^1\,7s^2$). The *ab initio* MCDF calculations do not accurately account for this exchange contribution, and thus the required empirical correction does not follow a continuous trend, otherwise seen in the filling of the nd^m sub-shell in the isonuclear sequences observed in this experiment and earlier work [74, 74, 104, 112–116] (*cf.* Fig. 2.5). In contrast to this, our CI+MBPT calculations with AMBiT include this effect from the start.

2.5 Conclusions

We performed optical and EUV spectroscopy on open-$4d$-shell ions Sn^{7+}–Sn^{10+} in a charge-state-resolved manner using an electron beam ion trap and recorded 90 magnetic dipole transitions. Line and level identifications were performed using the semi-empirical orthogonal parameters method and Cowan code calculations. Our measurements of transitions in the ground configuration of Sn^{7+} are in good agreement with previous measurements in the EUV [40]. The lines and level energies obtained for the $4d^m$ (m=6–4) configurations in Sn^{8+}–Sn^{10+} present the most complete data available to date for these ground configurations, with a total of 79 energy levels experimentally determined. Analogous to our recent work on Sn^{11+}–Sn^{14+} [79], we conclude that the classification of certain cataloged EUV transitions in previous work [32] needs to be revised. Furthermore, these many-valence-electron, open-$4d$-shell ions provide an excellent testing ground for state-of-the-art CI+MBPT calculations, performed with the AMBiT code. Our *ab initio* calculations are shown to be in very good agreement with our data, validating the predictive power of this theoretical method for these until now challengingly complex electronic systems.

2.6 Acknowledgments

This work is part of and supported by the DFG Collaborative Research Centre "SFB 1225 (ISOQUANT)". JB would like to express his gratitude for ARCNL's hospitality during his visit there.

2.7 Appendix

In this appendix, the tabulated values for all experimentally determined and calculated quantities are presented. Table 2.4 collects the measured $M1$ transitions of Sn^{7+}. Comparison is made between these transitions, the transitions as inferred from the levels determined in Ref. [40], and the transitions predicted by CI+MBPT theory. Moreover, in Table 2.3, the AMBiT-calculated energy levels of the $4d^7$ ground configuration of Sn^{7+} are compared to the level energies determined experimentally in Ref. [40].

Table 2.5 shows the wavelengths of the lines measured in the optical domain, along with their identification and values as determined from AMBiT calculations.

The energy levels of the ground configuration of the ions Sn^{8+}–Sn^{10+} are given in Table 2.6. Here the level energies optimized with Kramida's LOPT [73] are shown alongside with the levels calculated with the orthogonal energy parameters method, the results of CI+MBPT calculations, and levels from previous work [32]. Finally, the orthogonal parameters used in the semi-empirical calculations are collected in Table 2.7.

TABLE 2.4 Experimental vacuum wavelengths $\lambda_{\rm exp}$ and line intensities for Sn^{7+} within its ground electronic configuration [Kr] $4d^7$. Spectra recorded at acceleration potential of 157 V, which yielded maximum fluorescence signal. Intensity integrals from Gaussian fits were corrected for the grating efficiency. Wavelengths $\lambda_{\rm Ritz}$ are determined from the energy levels of Sn^{7+} given in Ref. [40]. Transition probabilities $gA_{ij,\rm COWAN}$ are calculated with the Cowan code based on those levels. Wavelengths $\lambda_{\rm CI+MBPT}$ are *ab initio* results from our CI+MBPT calculations. "Transition" column shows lower and upper levels as used in Fig. 2.4. Approximate LS-terms are given in the last column. Numbers in brackets are sequential indices as defined by Nielson and Koster [111] to differentiate levels with the same LSJ values. Superscripts *bl* mark spectral blends.

$\lambda_{\rm exp}$ (nm)	Intensity (arb. units)	$\lambda_{\rm Ritz}$ (nm)	$gA_{ij,\rm COWAN}$ (s^{-1})	$\lambda_{\rm CI+MBPT}$ (nm)	Transition (see Fig. 2.4)	Terms
333.9^{bl}	132	334.2	167	333.3	15-18	$^2F_{5/2}$-$^2D_{5/2}(1)$
374.5	271	374.8	375	372.9	1-11	$^4F_{7/2}$-$^2D_{5/2}(2)$
386.0	68	386.1	57	384.6	16-18	$^2F_{7/2}$-$^2D_{5/2}(1)$
441.9	142	441.8	262	444.0	0-6	$^4F_{9/2}$-$^2G_{9/2}$
454.3	12	454.2	66	455.0	1-8	$^4F_{7/2}$-$^2G_{7/2}$
492.2	69	492.2	44	495.8	2-10	$^4F_{5/2}$-$^4P_{3/2}$
536.0^{bl}	35	535.9	32	537.5	2-8	$^4F_{5/2}$-$^2G_{7/2}$
660.9	116	661.6	170	668.3	6-13	$^2G_{9/2}$-$^2H_{9/2}$

TABLE 2.5 Vacuum wavelengths and line intensities for Sn^{8+}–Sn^{10+} ions at the acceleration potential maximizing ion fluorescence. Intensities are taken from Gaussian fits and corrected for the grating efficiency. Wavelengths $\lambda_{\rm orth}$ are calculated from level energies from Table 2.6. Transition probabilities $gA_{ij,\rm COWAN}$ are determined with the Cowan code using the same level energies. Wavelengths $\lambda_{\rm CI+MBPT}$ calculated *ab initio* with the AMBiT CI+MBPT code. "Transition" refers to levels shown in Fig. 2.4. Configurations and approximate LS-coupling terms are given in the last two columns (the numbers in brackets are sequential indices [111] for distinction of levels with the same LSJ values). The superscript *bl* indicates line blends, and the superscript D marks doubly classified lines (i.e. which can be ambiguously assigned to two transitions).

Ion	V_{max} (V)	$\lambda_{\rm exp}$ (nm)	Intensity (arb. units)	$\lambda_{\rm orth}$ (nm)	$gA_{ij,\rm COWAN}$ (s^{-1})	$\lambda_{\rm CI+MBPT}$ (nm)	Transition (see Fig. 2.4)	Configuration	Term symbol
8+	137	283.4	18	284	104	283.1	11-27	[Kr] $4d^6$	$^3F_4(2)$-$^3F_4(1)$
		293.3	42	293	226	295.2	0-11		$^5D_4$-$^3F_4(2)$
		313.5	17	314	54	315.1	5-24		$^3H_4$-$^1F_3$
		315.0	16	315	60	315.4	0-9		$^5D_4$-$^3F_3(2)$
		317.6	45	318	192	316.6	12-27		$^3G_5$-$^3F_4(1)$
		326.0	15	326	105	325.2	18-30		$^3D_3$-$^3P_2(1)$
		330.4	70	330	279	331.6	18-29		$^3D_3$-$^3F_3(1)$
		344.6	25	344	31	346.5	1-11		$^5D_3$-$^3F_4(2)$
		354.8	33	355	102	352.3	14-26		$^3P_1(2)$-$^3P_0(1)$
		360.2^{bl}	43	360	120	363.5	17-28		$^3D_2$-$^3F_2(1)$
		374.5^{bl}	271	374	131	374.6	1-9		$^5D_3$-$^3F_3(2)$
		381.2	36	381	65	381.3	2-10		$^5D_2$-$^3F_2(2)$
		392.1	24	392	78	392.2	18-27		$^3D_3$-$^3F_4(1)$
		404.6	60	404	239	405.7	0-5		$^5D_4$-$^3H_4$
		426.6	54	428	186	424.0	8-21		$^3H_5$-$^1G_4(2)$
		434.1	36	434	107	434.2	9-23		$^3F_3(2)$-$^1D_2(2)$
		460.9	138	461	315	454.5	1-6		$^5D_3$-$^3P_2(2)$
		505.7	38	505	107	507.3	23-30		$^1D_2(2)$-$^3P_2(1)$
		513.2^{bl}	85	515	89	516.1	9-21		$^3F_3(2)$-$^1G_4(2)$
		551.8	40	552	65	542.9	3-6		$^5D_1$-$^3P_2(2)$
		560.9	149	560	185	568.9	7-20		$^3H_6$-$^1I_6$
		566.8	91	565	87	576.5	8-20		$^3H_5$-$^1I_6$
		584.4^{D}	118	585	62	599.1	6-18		$^3P_2(2)$-$^3D_3$
		584.4^{D}	118	585	291	581.0	11-21		$^3F_4(2)$-$^1G_4(2)$
9+	137	261.0	66	261	304	262.9	0-5	[Kr] $4d^5$	$^6S_{5/2}$-$^4G_{5/2}$
		272.0	53	272	418	273.8	3-24		$^4G_{11/2}$-$^2H_{11/2}$
		276.6	30	276	209	278.4	4-24		$^4G_{9/2}$-$^2H_{11/2}$
		296.0^{D}	46	296	115	295.2	8-27		$^4D_{7/2}$-$^2F_{5/2}(1)$
		296.0^{D}	46	296	149	299.6	0-1		$^6S_{5/2}$-$^4G_{5/2}$
		304.8	25	303	69	306.2	19-32		$^2H_{9/2}$-$^2G_{7/2}(1)$
		306.6^{bl}	34	306	16	307.7	6-23		$^4P_{3/2}$-$^2F_{5/2}(2)$
		312.1	62	312	151	311.5	4-22		$^4G_{9/2}$-$^2F_{7/2}(1)$

TABLE 2.5 (continued)

Ion	V_{max} (V)	λ_{exp} (nm)	Intensity (arb. units)	λ_{orth} (nm)	$gA_{ij,COWAN}$ (s^{-1})	$\lambda_{CI+MBPT}$ (nm)	Transition (see Fig. 2.4)	Configuration	Term symbol
		323.9	50	324	105	326.7	8-26		$^4D_{7/2}$-$^2G_{9/2}(2)$
		333.9^{bl}	70	333	132	335.0	2-19		$^4G_{7/2}$-$^2H_{9/2}$
		338.7^{bl}	219	339	222	338.2	4-20		$^4G_{9/2}$-$^2G_{7/2}(2)$
		349.1^{bl}	271	349	297	350.7	4-19		$^4G_{9/2}$-$^2H_{9/2}$
		356.8	41	354	57	362.0	22-31		$^2F_{7/2}(1)$-$^2G_{9/2}(1)$
		395.5	64	394	131	398.1	8-22		$^4D_{7/2}$-$^2F_{7/2}(1)$
		398.3	68	398	86	396.7	1-16		$^4G_{5/2}$-$^4F_{3/2}$
		399.9	26	401	42	398.2	18-29		$^4F_{5/2}$-$^2D_{3/2}(2)$
		413.5	43	415	133	419.2	25-32		$^2F_{7/2}(2)$-$^2G_{7/2}(1)$
		438.9	46	439	155	442.7	8-20		$^4D_{7/2}$-$^2G_{7/2}(2)$
		439.7	34	441	109	446.2	25-31		$^2F_{7/2}(2)$-$^2G_{9/2}(1)$
		452.4	32	453	105	444.8	12-26		$^2I_{11/2}$-$^2G_{9/2}(2)$
		457.0^{D}	58	456	99	453.4	2-15		$^4G_{7/2}$-$^2D_{5/2}(3)$
		457.0^{D}	58	456	82	458.0	3-17		$^4G_{11/2}$-$^4F_{9/2}$
		485.0^{bl}	358	484	472	480.5	12-24		$^2I_{11/2}$-$^2H_{11/2}$
		489.2	414	489	562	489.1	5-15		$^4G_{5/2}$-$^2D_{5/2}(3)$
		492.2	107	492	69	491.9	4-14		$^4G_{9/2}$-$^4F_{7/2}$
		497.0	55	496	107	497.3	23-30		$^2F_{5/2}(2)$-$^2D_{5/2}(2)$
		501.4	167	502	339	496.6	15-27		$^2D_{5/2}(3)$-$^2F_{5/2}(1)$
		507.6	105	508	103	511.4	6-16		$^4P_{3/2}$-$^4F_{3/2}$
		570.8	76	569	151	563.8	13-24		$^2I_{13/2}$-$^2H_{11/2}$
		618.9	137	621	119	636.2	3-12		$^4G_{11/2}$-$^2I_{11/2}$
10+	217	283.7	13	283	278	283.0	15-27	[Kr] $4d^4$	$^3F_3(2)$-$^3F_2(1)$
		284.7	18	285	114	286.3	3-15		$^5D_3$-$^3F_3(2)$
		286.0	33	286	163	287.4	4-16		$^5D_4$-$^3D_3$
		297.4^{D}	15	297	110	298.8	1-10		$^5D_1$-$^3F_2(2)$
		297.4^{D}	15	298	91	296.7	15-26		$^3F_3(2)$-$^3F_4(1)$
		300.5	15	300	73	300.2	3-13		$^5D_3$-$^3P_2(2)$
		328.1^{D}	112	328	137	333.1	4-14		$^5D_4$-$^3G_4$
		328.1^{D}	112	328	261	327.4	16-26		$^3D_3$-$^3F_4(1)$
		346.8	91	347	278	348.2	2-9		$^5D_2$-$^3P_1(2)$
		349.1^{bl}	271	349	93	349.7	18-27		$^3D_2$-$^3F_2(1)$
		353.0	38	353	82	359.0	2-7		$^5D_2$-$^3G_3$
		361.9	14	361	95	363.1	19-27		$^3D_1$-$^3F_2(1)$
		367.7	145	368	227	374.6	4-12		$^5D_4$-$^3F_4(2)$
		383.7	28	384	84	378.0	5-19		$^3P_0(2)$-$^3D_1$
		392.7	68	392	124	390.6	9-22		$^3P_1(2)$-$^1S_0(2)$
		407.4	38	408	87	402.4	8-21		$^3H_5$-$^1G_4(2)$
		421.8	26	421	139	428.3	1-5		$^5D_1$-$^3P_0(2)$
		450.5	18	450	88	444.7	21-28		$^1G_4(2)$-$^3F_3(1)$
		508.2	127	508	193	510.3	16-24		$^3D_3$-$^1F_3$
		520.7	84	521	310	518.6	12-21		$^3F_4(2)$-$^1G_4(2)$
		524.2	17	525	45	516.5	21-26		$^1G_4(2)$-$^3F_4(1)$
		534.4	117	535	234	538.4	8-20		$^3H_5$-$^1I_6$

TABLE 2.5 (continued)

Ion V_{max} (V)	λ_{exp} (nm)	Intensity (arb. units)	λ_{orth} (nm)	$gA_{ij,COWAN}$ (s^{-1})	$\lambda_{CI+MBPT}$ (nm)	Transition (see Fig. 2.4)	Configuration	Term symbol
	614.1^D	95	614	102	643.9	4-6		$^5D_4$-$^3H_4$
	614.1^D	95	616	106	616.1	16-23		$^3D_3$-$^1D_2(2)$
	628.3	69	630	116	626.8	14-21		$^3G_4$-$^1G_4(2)$
	639.9	157	642	201	642.9	11-20		$^3H_6$-$^1I_6$
	689.5^{bl}	85	690	164	697.0	15-21		$^3F_3(2)$-$^1G_4(2)$
	728.1	39	727	103	713.1	8-17		$^3H_5$-$^3G_5$

TABLE 2.6 Energy levels of the Sn^{8+} $4d^6$, Sn^{9+} $4d^5$, and Sn^{10+} $4d^4$ configurations (in cm^{-1}) adjusted with the LOPT algorithm [73] based on the measured transitions. Levels labels use approximate LS-coupling terms. Numbers in brackets display sequential indices [111] to differentiate levels having the same LSJ values. Uncertainties x_j ($j = 1-5$) and y are given as the one-standard-deviation of the orthogonal parameters fit for the respective configuration: $x_{1,2,3} = \pm 16\,cm^{-1}$; $x_4 = \pm 41\,cm^{-1}$; $x_5 = y = \pm 14\,cm^{-1}$. The dispersive energy uncertainty D_1 is close to the minimum uncertainty of separation from other levels, and the energy uncertainty D_2 is that relative to the ground level of the configuration (*cf.* [73]). N is the total number of lines connected to the level. $E_{\rm orth}$ values are semi-empirical energy levels calculated with the orthogonal parameters in Table 2.7. The $E_{\rm CI+MBPT}$ values are *ab initio* energy levels calculated using the AMBiT CI+MBPT code. Differences between experimental and calculated values appear in columns $\Delta E_{\rm orth}$ ($E_{\rm exp} - E_{\rm orth}$) and $\Delta E_{\rm CI+MBPT}$ ($E_{\rm exp} - E_{\rm CI+MBPT}$). Energies determined from previous vacuum spark measurement [32] shown as $E_{\rm vs}$; $\Delta E_{\rm vs} = E_{\rm exp} - E_{\rm vs}$, their deviations. Uncertainties in the systematic common shifts of the identified level groups z_i ($i = 1-8$) [32] are of the order of several hundreds of cm^{-1} (see main text). The uncertainty of the relative level energies within each of these groups was estimated at $10\,cm^{-1}$.

Ion	Level	Term	$E_{\rm exp}$	D_1	D_2	N	$E_{\rm orth}$	$\Delta E_{\rm orth}$	$E_{\rm CI+MBPT}$	$\Delta E_{\rm CI+MBPT}$	$E_{\rm vs}$	$\Delta E_{\rm vs}$
8+ $4d^6$	0	$^5D_4$	0	30	0	3	-5	5	0	0	0	0
	1	$^5D_3$	5075	13	30	3	5064	11	5011	64	5050	25
	2	$^5D_2$	6634+x_2	0	0	1	6634	0	6626	8	6670+z_1	-36
	3	$^5D_1$	8648	13	40	1	8636	12	8593	55	8670+z_1	-22
	4	$^5D_0$					9345		9307			
	5	$^3H_4$	24716	24	24	1	24726	-10	24651	65	24685+z_2	31
	6	$^3P_2(2)$	26785	16	40	3	26771	14	27011	-226		
	7	$^3H_6$	27592	13	43	1	27604	-12	27270	322	27610+z_2	-18
	8	$^3H_5$	27778	22	39	2	27781	-3	27503	275	27710+z_2	68
	9	$^3F_3(2)$	31740	12	30	4	31736	4	31709	31	31747+z_3	-7
	10	$^3F_2(2)$	32847+x_2	28	28	1	32847	0	32855	-8	33028+z_3	-181
	11	$^3F_4(2)$	34103	11	30	4	34102	1	33873	230	34220+z_2	-117
	12	$^3G_5$	37908	40	59	1	37930	-22	37616	292	37950+z_2	-42
	13	$^1S_0(4)$					38532		38684			
	14	$^3P_1(2)$	38694+x_1	0	0	1	38694	0	38903	-209		
	15	$^3G_4$					39872		39674		39609+z_2	
	16	$^3G_3$					41548		41310			
	17	$^3D_2$	42340+x_3	0	0	1	42340	0	42287	53	41787+z_2	553
	18	$^3D_3$	43879	17	40	4	43887	-8	43704	175		
	19	$^3D_1$					45061		44847			
	20	$^1I_6$	45421	13	41	2	45399	22	45032	389	45440+z_2	-19
	21	$^1G_4(2)$	51219	11	30	3	51217	2	51085	134	50840+z_4	379
	22	$^3P_0(2)$					54202		54250			
	23	$^1D_2(2)$	54777	13	40	2	54795	-18	54742	35		
	24	$^1F_3$	56613	41	47	1	56586	27	56385	228		
	25	$^3P_1(1)$					65561		65611			
	26	$^3P_0(1)$	66874+x_1	32	32	1	66875	-1	67067	-193		
	27	$^3F_4(1)$	69394	23	40	3	69401	-7	69198	196	68566+z_2	828

TABLE 2.6 (continued)

Ion	Level	Term	$E_{\rm exp}$	D_1	D_2	N	$E_{\rm orth}$	$\Delta E_{\rm orth}$	$E_{\rm CI+MBPT}$	$\Delta E_{\rm CI+MBPT}$	$E_{\rm vs}$	$\Delta E_{\rm vs}$
	28	$^3F_2(1)$	70 006+x_3	31	31	1	70 006	0	69 800	206		
	29	$^3F_3(1)$	74 146	37	54	1	74 144	2	73 860	286	73 385+z_2	761
	30	$^3P_2(1)$	74 552	14	40	2	74 548	4	74 454	98		
	31	$^1G_4(1)$					79 767		79 565		79 186+z_2	
	32	$^1D_2(1)$					101 675		101 319		99 838+z_4	
	33	$^1S_0(1)$					131 838		131 874		130 008+z_4	
$9+\ 4d^5$	0	$^6S_{5/2}$	0	59	0	2	-17	17	0	0	0	0
	1	$^4G_{5/2}$	33 784	61	61	2	33 748	36	33 381	403	33 582+z_5	202
	2	$^4G_{7/2}$	36 874	21	70	2	36 834	40	36 421	453	36 610+z_5	264
	3	$^4G_{11/2}$	37 535	10	90	3	37 576	-41	37 145	390	37 399+z_5	136
	4	$^4G_{9/2}$	38 170	20	80	5	38 173	-3	37 759	411	37 958+z_5	212
	5	$^4G_{5/2}$	38 315	16	59	2	38 282	33	38 032	283	38 110+z_5	205
	6	$^4P_{3/2}$	39 190	16	68	2	39 183	7	39 035	155	39 010+z_5	180
	7	$^4P_{1/2}$					42 159		42 060			
	8	$^4D_{7/2}$	44 915	15	80	4	44 958	-43	44 737	178	44 470+z_5	445
	9	$^4D_{5/2}$					49 065		48 907			
	10	$^4D_{1/2}$					49 104		48 996			
	11	$^4D_{3/2}$					50 861		50 753			
	12	$^2I_{11/2}$	53 692	8	80	3	53 685	7	52 863	829	53 554+z_5	138
	13	$^2I_{13/2}$	56 792	12	83	1	56 765	27	55 937	855	56 660+z_5	132
	14	$^4F_{7/2}$	58 487	16	77	1	58 491	-4	58 088	399	58 300+z_5	187
	15	$^2D_{5/2}(3)$	58 756	14	60	3	58 721	35	58 479	277	58 370+z_5	386
	16	$^4F_{3/2}$	58 891	25	66	2	58 848	43	58 588	303		
	17	$^4F_{9/2}$	59 417	28	87	1	59 469	-52	58 981	436	58 850+z_5	567
	18	$^4F_{5/2}$	63 643+x_4	0	0	1	63 643	0	63 291	352		
	19	$^2H_{9/2}$	66 824	22	70	3	66 846	-22	66 273	551	66 427+z_5	397
	20	$^2G_{7/2}(2)$	67 698	18	80	2	67 687	11	67 325	373	66 975+z_5	723
	21	$^2D_{3/2}(3)$					68 584		68 321			
	22	$^2F_{7/2}(1)$	70 199	18	80	3	70 228	-29	69 859	340	70 185+z_5	14
	23	$^2F_{5/2}(2)$	71 806	43	80	2	71 837	-31	71 529	277		
	24	$^2H_{11/2}$	74 311	16	80	4	74 338	-27	73 674	637	74 195+z_5	116
	25	$^2F_{7/2}(2)$	75 470	16	80	2	75 423	47	75 073	397	74 385+z_5	1 085
	26	$^2G_{9/2}(2)$	75 795	18	80	2	75 816	-21	75 347	448	75 345+z_5	450
	27	$^2F_{5/2}(1)$	78 700	16	60	2	78 654	46	78 616	84		
	28	$^2S_{1/2}$					78 719		78 457			
	29	$^2D_{3/2}(2)$	88 649+x_4	25	25	1	88 702	-53	88 405	244		
	30	$^2D_{5/2}(2)$	91 927	16	81	1	91 976	-49	91 640	287	90 911+z_5	1 016
	31	$^2G_{9/2}(1)$	98 217	18	80	2	98 228	-11	97 485	732	96 800+z_5	1 417
	32	$^2G_{7/2}(1)$	99 649	21	80	2	99 568	81	98 927	722	98 277+z_5	1 372
	33	$^2P_{3/2}$					114 830		114 351			
	34	$^2P_{1/2}$					117 607		117 122			
	35	$^2D_{5/2}(1)$					128 906		128 281			
	36	$^2D_{3/2}(1)$					130 802		130 180			
$10+\ 4d^4$	0	$^5D_0$	0+y	0	0	0	0	0	0	0	0	0
	1	$^5D_1$	3 043	22	0	2	3 043	0	3 141	-98	3 035	8
	2	$^5D_2$	6 590+x_5	0	0	2	6 590	0	6 717	-127	6 545	45
	3	$^5D_3$	10 073	49	84	2	10 054	19	10 213	-140	10 005	68
	4	$^5D_4$	13 300	24	70	4	13 315	-15	13 516	-216	13 280	20
	5	$^3P_0(2)$	26 752	27	23	2	26 750	2	26 490	262		
	6	$^3H_4$	29 584	15	75	1	29 589	-5	29 046	538	29 380+z_6	204

TABLE 2.6 (continued)

Ion	Level	Term	$E_{\rm exp}$	D_1	D_2	N	$E_{\rm orth}$	$\Delta E_{\rm orth}$	$E_{\rm CI+MBPT}$	$\Delta E_{\rm CI+MBPT}$	$E_{\rm vs}$	$\Delta E_{\rm vs}$
	7	$^3G_3$	34 918+x_5	32	32	1	34 899	19	34 573	345	34 630+z_6	288
	8	$^3H_5$	35 147	24	73	3	35 143	4	34 639	508	34 814+z_7	333
	9	$^3P_1(2)$	35 425+x_5	33	33	2	35 429	-4	35 438	-13	35 048+z_6	377
	10	$^3F_2(2)$	36 669	61	61	1	36 666	3	36 613	56	36 297+z_6	372
	11	$^3H_6$	38 232	10	70	1	38 226	6	37 656	576	37 890+z_7	342
	12	$^3F_4(2)$	40 490	13	70	2	40 475	15	40 208	282	40 130+z_7	360
	13	$^3P_2(2)$	43 351	44	95	1	43 377	-26	43 530	-179	42 898+z_6	453
	14	$^3G_4$	43 777	10	70	2	43 765	12	43 539	238	43 710+z_7	67
	15	$^3F_3(2)$	45 197	8	70	3	45 196	1	45 146	51	44 766+z_7	431
	16	$^3D_3$	48 279	35	80	4	48 263	16	48 310	-31	47 850+z_7	429
	17	$^3G_5$	48 881	8	73	1	48 893	-12	48 663	218	48 480+z_7	401
	18	$^3D_2$	51 801	30	60	1	51 808	-7	51 885	-84		
	19	$^3D_1$	52 814	31	35	2	52 806	8	52 945	-131		
	20	$^1I_6$	53 860	14	74	2	53 867	-7	53 211	649	53 475+z_7	385
	21	$^1G_4(2)$	59 693	6	70	6	59 684	9	59 493	200		
	22	$^1S_0(2)$	60 890+x_5	26	42	1	60 870	20	61 041	-151		
	23	$^1D_2(2)$	64 563	15	80	1	64 549	14	64 542	21		
	24	$^1F_3$	67 957	16	80	1	67 958	-1	67 907	50	66 757+z_8	1 200
	25	$^3P_2(1)$					75 662		75 823			
	26	$^3F_4(1)$	78 771	14	70	3	78 777	-6	78 854	-83		
	27	$^3F_2(1)$	80 446	50	47	3	80 445	1	80 484	-38		
	28	$^3F_3(1)$	81 891	20	71	1	81 881	10	81 982	-91	80 207+z_8	1 684
	29	$^3P_1(1)$					82 941		83 107			
	30	$^3P_0(1)$					86 664		86 851			
	31	$^1G_4(1)$					89 965		89 627			
	32	$^1D_2(1)$					112 401		112 544			
	33	$^1S_0(1)$					144 549		145 002			

TABLE 2.7 Orthogonal energy parameters (all in cm^{-1}) obtained by fitting experimental energy levels (FIT) and ratios of FIT to MCDF code (FIT/MCDF) calculations. Experimental energy levels taken from: Ref. [105, 106] for Sn^{6+}, Ref. [40] for Sn^{7+}, this work for Sn^{8+}–Sn^{10+} and Ref. [79] for Sn^{11+}, Sn^{12+}). Two-particle magnetic parameters (A_c-A_0) were fixed to *ab initio* MCDF calculations, not fitted, and thus not listed here. Effective Coulomb-interaction operators E'_a, E'_b, and effective three-particle electrostatic operators $T1$ and $T2$ are fit parameters for the given number of d electrons. For the fits parameters E'_b in Sn^{11+} and E'_a in Sn^{12+} were fixed (denoted by the superscript letter f) on extrapolated values (see main text). Fits were performed for the interacting $4d^k$+$4d^{k-1}\,5s$+$4d^{k-2}\,5s^2$ configurations, k=8–2 for Sn^{6+}–Sn^{12+} respectively. Energy parameters for the unknown $4d^{k-1}\,5s$+$4d^{k-2}\,5s^2$ configurations (not listed) were fixed at *ab initio* values for the average energies and spin-orbit interactions, but scaled by 0.85 for electrostatic and configuration interaction parameters. Average energy $E_{\rm av}$ is defined such that the ground level energy of the $4d^k$+$4d^{k-1}\,5s$+$4d^{k-2}\,5s^2$ configurations is equal to zero. σ is the root-mean-square of the fit uncertainty in cm^{-1} for the calculated configuration. "n/a" indicates non-applicable parameters.

Parameter	Sn^{6+}		Sn^{7+}		Sn^{8+}		Sn^{9+}	
	FIT	FIT/MCDF	FIT	FIT/MCDF	FIT	FIT/MCDF	FIT	FIT/MCDF
$E_{\rm av}$	16 279(4)	0.890	29 983(4)	0.890	42 688(4)	0.888	64 568(10)	0.872
$O2$	9 649(6)	0.856	9 979(5)	0.860	10 288(5)	0.863	10 592(9)	0.867
$O2'$	6 100(6)	0.795	6 326(4)	0.803	6 526(7)	0.808	6 702(11)	0.812
E'_a	243(6)		247(3)		255(3)		256(6)	
E'_b	22(5)		34(3)		37(5)		66(10)	
$\zeta(4d)$	3 688(4)	1.024	3 899(3)	1.021	4 119(3)	1.020	4 334(8)	1.018
$T1$	n/a	n/a	-5.2(0.2)		-5.6(0.1)		-5.9(0.3)	
$T2$	n/a	n/a	n/a	n/a	0.26(0.16)		-0.05(0.75)	
σ	10		14		16		41	

Parameter	Sn^{10+}		Sn^{11+}		Sn^{12+}	
	FIT	FIT/MCDF	FIT	FIT/MCDF	FIT	FIT/MCDF
$E_{\rm av}$	50 180(3)	0.91	37 553(9)	0.911	24 425(14)	0.93
$O2$	10 878(3)	0.87	11 200(16)	0.876	11 480(43)	0.88
$O2'$	6 896(6)	0.818	7 007(23)	0.815	7 102(43)	0.81
E'_a	275(2)		248(15)		260^f	
E'_b	44(3)		50^f		n/a	n/a
$\zeta(4d)$	4563(3)	1.017	4783(6)	1.013	5038(11)	1.016
$T1$	-6.6(0.1)		-9.72(1.0)		n/a	n/a
$T2$	0.37(0.16)		n/a	n/a	n/a	n/a
σ	14		20		32	

CHAPTER THREE

SHORT-WAVELENGTH OUT-OF-BAND EUV EMISSION FROM SN LASER-PRODUCED PLASMA

F. Torretti, R. Schupp, D. Kurilovich, A. Bayerle, J. Scheers, W. Ubachs, R. Hoekstra, and O. O. Versolato

Journal of Physics B: Atomic, Molecular and Optical Physics **51**(4), 045005 (2018)

We present the results of spectroscopic measurements in the extreme ultraviolet (EUV) regime (7–17 nm) of molten tin microdroplets illuminated by a high-intensity 3-J, 60-ns Nd:YAG laser pulse. The strong 13.5 nm emission from this laser-produced plasma is of relevance for next-generation nanolithography machines. Here, we focus on the shorter wavelength features between 7 and 12 nm which have so far remained poorly investigated despite their diagnostic relevance. Using flexible atomic code calculations and local thermodynamic equilibrium arguments, we show that the line features in this region of the spectrum can be explained by transitions from high-lying configurations within the Sn^{8+}–Sn^{15+} ions. The dominant transitions for all ions but Sn^{8+} are found to be electric-dipole transitions towards the n=4 ground state from the core-excited configuration in which a $4p$ electron is promoted to the $5s$ sub-shell. Our results resolve some long-standing spectroscopic issues and provide reliable charge state identification for Sn laser-produced plasma, which could be employed as a useful tool for diagnostic purposes.

3.1 Introduction

Sn and its highly charged ions are of undoubtable technological importance, as these are the emitters of extreme ultraviolet (EUV) radiation around 13.5 nm used in nanolithographic applications [38, 39]. In such state-of-the-art lithography machines, EUV light is generated using pulsed, droplet-based, laser-produced plasma (LPP) [17, 117]. Molten Sn microdroplets are illuminated by high-intensity (10^9–10^{12} W/cm^2) laser pulses, generating typically high-density (10^{19}–10^{21} e/cm^3) plasma. In this plasma, laser light is converted efficiently into photons with wavelengths close to 13.5 nm. Technologically this is advantageous as it corresponds to the peak reflectivity of the mirrors composing the projection optics in nanolithography machines. These molybdenum-silicon multilayer mirrors (MLMs) [16, 118] are characterised by an "in-band", 2-% reflectivity bandwidth centered around 13.5 nm, which conveniently overlaps with the strong EUV emission of Sn LPP. The relatively high conversion efficiency of laser into EUV light in this wavelength region is mainly due to the atomic structure of the highly charged Sn ions found in this laser-produced plasma.

The atomic transitions responsible for these EUV photons are $4p^6\,4d^m$–$4p^6\,4d^{m-1}\,4f$ + $4p^6\,4d^{m-1}\,5p$ + $4p^5\,4d^{m+1}$, with m=6–0 for Sn^{8+}–Sn^{14+} [30]. These transitions are clustered in so-called unresolved transition arrays (UTAs) [76] as the close-lying large number of possible transitions arising from the complex open-$4d$-subshell electronic structure renders them unresolvable in practical applications. Configuration-interaction between the excited states $4p^6\,4d^{m-1}\,4f^1$ and $4p^5\,4d^{m+1}$ causes a significant redistribution of oscillator strength towards the high-energy side of the transition arrays, which is referred to as "spectral narrowing" [31]. A serendipitous level crossing involving the EUV-contributing excited configurations [57] furthermore fixes the average excitation energies of the excited states to the same value across a number of charge states.

The nature of the convoluted structure of these highly charged ions has been addressed in several theoretical and experimental investigations both directly in the EUV regime and in the optical regime where charge-state-resolved spectroscopy enables complementary investigations that challenge the direct EUV measurements [32–37, 40, 41, 45, 79, 119, 120].

In view of the application perspective, most of the work has so far been focused on the configurations responsible for emission around 13.5 nm. However, in dense and hot plasmas, a significant amount of energy can be radiated at shorter wavelengths arising from configurations that remain poorly investigated with, to the best of our knowledge, but a single study [41] dedicated to the corresponding transition arrays. This short-wavelength, "out-of-band" radiation could very well negatively affect the optics lifetime [118, 121], whilst obviously hindering the conversion efficiency from laser energy to 13.5 nm pho-

tons.

In our experiments EUV spectra are obtained from plasma created by irradiating micrometer-sized molten Sn droplets with a pulsed Nd:YAG laser. We focus on the short-wavelength, high-energy features in the 7–12 nm region and provide a detailed study of their origins using the flexible atomic code (FAC) [48]. Applying a simple local thermodynamic equilibrium (LTE) scaling argument, we show that the line features in the experimental spectrum can be well explained by electric dipole ($E1$) transitions from high-lying configurations within the same tin charge states responsible for 13.5 nm radiation in EUV sources. We find that the dominant contribution in the short wavelength region actually comes from the core-excited configuration $4p^5\,4d^m\,5s$ where a $4p$ core electron is promoted to the $5s$ subshell. Our calculations excellently reproduce the line emission features observed experimentally, furthering the understanding of these emission features, and enabling the identification of individual contributions from various charge states Sn^{8+}–Sn^{15+} which remain unresolvable in the 13.5 nm UTAs. Furthermore, using the Bauche-Arnoult UTA formalism [31,76,122] as well as Gaussian fits to our results, we provide simplified outcome of our calculations which can be used to straightforwardly interpret Sn LPP spectra.

3.2 Experiment

The experimental setup to generate droplets has been described in a previous publication [23], and only the details relevant to this chapter are presented in the following. Droplets of molten tin of 99.995 % purity are dispensed from a droplet generator operating at a 10.2-kHz repetition rate inside a vacuum vessel filled with a continuous flow of Ar buffer gas ($\sim 10^{-2}$ mbar). The droplets have a diameter of approximately 45 μm. An injection-seeded, 10-Hz repetition rate, 3-J, 60-ns pulse length Nd:YAG laser operating at its fundamental wavelength λ=1064 nm is imaged to a circular flat-top beam spot (200 μm at $1/e^2$ encircled energy) at the droplet position, producing an averaged intensity of $1.6{\cdot}10^{11}$ W/cm^2, close to industrially relevant conditions for obtaining high conversion efficiency [123–125]. Using polarizing optics the laser energy can be set without modifying the beam spot. The linearly-polarised laser pulse is timed to hit the droplet, thus creating an EUV-emitting plasma. This emitted EUV radiation is coupled into a grazing-incidence spectrometer positioned at a 120° angle with respect to the laser light propagation direction (directly facing the laser-droplet interaction zone). Optical light and debris from the laser-produced plasma are blocked by a 200-nm-thick zirconium filter. In the spectrometer the EUV light is diffracted by a gold-coated concave grating (1.5 m radius of curvature,

1200 lines-per-mm) at an angle of incidence of 86° with respect to the grating normal. The 100-μm entrance slit and the detector, a Greateyes back-illuminated charge coupled device (GE 2048 512 BI UV1) cooled to 0°C, are positioned on the circle determined by the radius of curvature of the grating, in a standard Rowland circle geometry. Wavelength calibration is performed after the measurements using an aluminium solid target positioned at the same location as the droplets and ablated by the Nd:YAG laser. Well-known Al^{3+} and Al^{4+} lines in the 10–16 nm range from the NIST atomic database [63] are used, obtaining a calibration function with a systematic one-standard-deviation uncertainty of 0.003 nm. The typical full-width at half-maximum of the features observed is approximately 0.06 nm at 13 nm wavelength.

During acquisition, the camera is exposed to about ten droplets irradiated by the Nd:YAG laser. This exposure is repeated multiple times to improve the statistics of the measurement, resulting in an averaged spectrum. The obtained spectrum is corrected for geometrical aberrations causing the spectra to move across the vertical, non-dispersive axis of the camera, as is known from the Al calibration spectra. Background counts are dominated by readout-noise and are subtracted before averaging over the non-dispersive axis. The contribution of second-order diffraction is obtained from the line emission in the Al calibration spectra, enabling the related correction. Further corrections are subsequently applied for the sensor quantum efficiency, as obtained from the manufacturer datasheets, and the Zr-filter transmission curve [126]. No correction curves could be obtained for the gold-coated grating. However, the behaviour in the 7–12 nm region can reasonably be expected to be rather constant [126].

Fig. 3.1 shows a thus obtained spectrum. The strongest feature is found near 13.5 nm wavelength as expected. The left shoulder of this UTA feature, starting its steep rise upward from about 13 nm with well-known contributions from Sn^{10+}–Sn^{14+} [32, 34, 35] continuing to a peak at exactly 13.5 nm after which the feature decays more slowly as it moves over the contributions of the lower tin charge states [32, 33] whilst also suffering opacity-related broadening [28]. This main feature appears to lie on top of an apparent continuum which extends over the full observed wavelength range. At the typical plasma conditions of this LPP, such continuum radiation is usually attributed to recombination processes [127]. Continuing our investigations to line features with wavelengths below 12 nm first requires new calculations since, as pointed out in the introduction, pertinent experimental data and calculations are sparsely available.

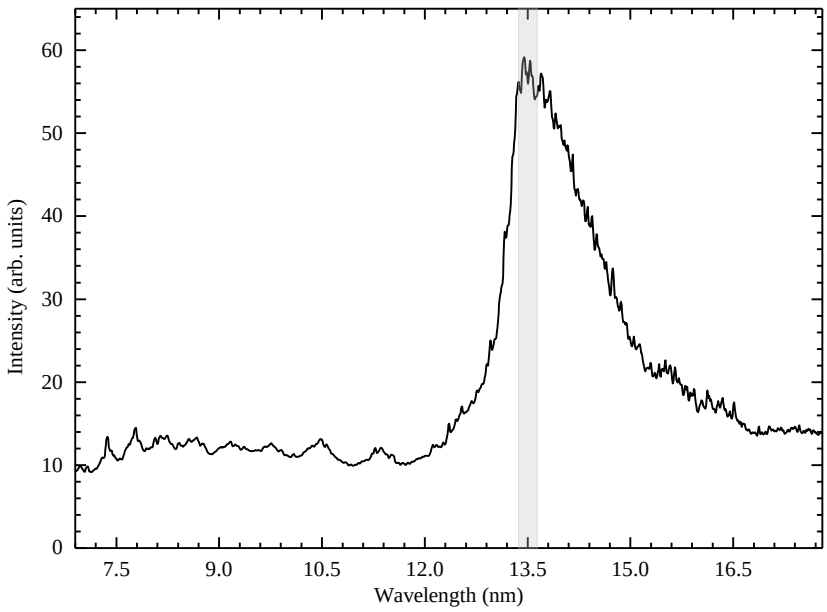

FIGURE 3.1 Experimental spectrum emitted by the plasma generated from a 45 μm-diameter Sn droplet irradiated by a 60-ns Nd:YAG laser pulse, circular flat-top beam spot of 200 μm ($1/e^2$ encircled energy). This spectrum is obtained at an average laser intensity of $1.6 \cdot 10^{11}$ W/cm^2. The shaded gray area shows the 2-% reflectivity bandwidth of multi-layer mirrors.

3.3 Calculations

Atomic structure

For the interpretation of the short-wavelength side of the obtained experimental spectrum, we employ the flexible atomic code (FAC) [48]. Specifically, we use it to investigate short-wavelength transitions in the 7–12 nm region in Sn^{8+}–Sn^{15+}. FAC performs relativistic atomic structure calculations including configuration-interaction. The atomic wavefunctions are calculated as linear combination of configuration state functions, which are determined from a local central potential obtained by solving self-consistently the Dirac equations. Relativistic effects are taken into account by the Dirac-Coulomb Hamiltonian. Radiative transition rates are calculated from the obtained wavefunctions in the single-multipole approximation. For more details, we refer to reference [48].

Calculations are performed including the following configurations for the open-$4d$-shell ions Sn^{8+}–Sn^{13+}: the ground state [Kr] $4d^m$, [Kr] $4d^{m-1}\,4f$, [Kr] $4d^{m-1}\,5pf$, [Kr] $4d^{m-1}\,6pf$, [Ar] $3d^{10}\,4s^2\,4p^5\,4d^{m+1}$, [Ar] $3d^{10}\,4s^2\,4p^5\,4d^m\,5sd$, [Ar] $3d^{10}\,4s^2\,4p^5\,4d^m\,6sd$ (m=6–1). This somewhat limited set of configurations is used since, in the chosen benchmark case of Sn^{8+}, they give good agreement with both *ab initio* multi-configuration Dirac-Fock calculations performed by Svendsen and O'Sullivan [41] as well as with the current experimental observations. For the open-$4p$-shell ions Sn^{14+} and Sn^{15+}, the configuration sets used are [Ar] $3d^{10}\,4s^2\,4p^q$, [Ar] $3d^{10}\,4s^2\,4p^q\,4df$, [Ar] $3d^{10}\,4s^2\,4p^q\,5spd$, [Ar] $3d^{10}\,4s^2\,4p^q\,6spd$ (q=4,5), which are found to give good agreement with measured features. Weighted transition rates g_iA_{ij} (statistical weight g_i of upper level i times the transition probability A_{ij} from i to j) are calculated for transitions from each excited state towards the ground state for all ions involved.

Emission properties

Our FAC calculations indicate that in the 7–12 nm (or approximately 110–180 eV) region the main transitions of interest (i.e. the strongest contributions to the radiative decay) are the following: $4d^m$–$4d^{m-1}\,5f$ (from here on denoted as $4d$–$5f$), $4d^m$–$4d^{m-1}\,6p$ ($4d$–$6p$), $4d^m$–$4d^{m-1}\,6f$ ($4d$–$6f$), $4p^6\,4d^m$–$4p^5\,4d^m\,5s$ ($4p$–$5s$), $4p^6\,4d^m$–$4p^5\,4d^m\,5d$ ($4p$–$5d$), $4p^6\,4d^m$–$4p^5\,4d^m\,6s$ ($4p$–$6s$), $4p^6\,4d^m$–$4p^5\,4d^m\,6d$ ($4p$–$6d$). These are all $E1$ single-electron excitations. In Fig. 3.2 the properties of these transition arrays are presented for the isonuclear sequence Sn^{8+}–Sn^{15+}. The weighted mean energies in Fig. 3.2(a) are calculated using as weights the transition rates (this is in accordance with the UTA formalism, see section 3.5 for a more thorough description). They are seen to scale quite regularly along the isonuclear sequence, increasing for higher ionic charge. There is no level crossing apparent, making these transition arrays a potential diagnostic tool to identify the contributions of different charge states in the spectra of Sn LPPs.

The weighted mean energies of the transition arrays towards the n=4 ground state stemming from configurations with principal quantum number n=6 are observed to scale more strongly with charge state Z compared to configurations having n=5. This can be explained similarly to hydrogenic scaling of binding energy for different n orbitals. In these systems, the binding energy scales with $Z^2\,n^{-2}$. The transition energy, i.e. the difference between the ground state and the excited state binding energies, will therefore have a stronger dependence on ionic charge for higher n. Naturally, this exact scaling does not perfectly describe the one observed, as hydrogenic approximations are far too limited to be able to interpret complicated ionic systems with multiple valance electrons such as the highly charged Sn ions here considered.

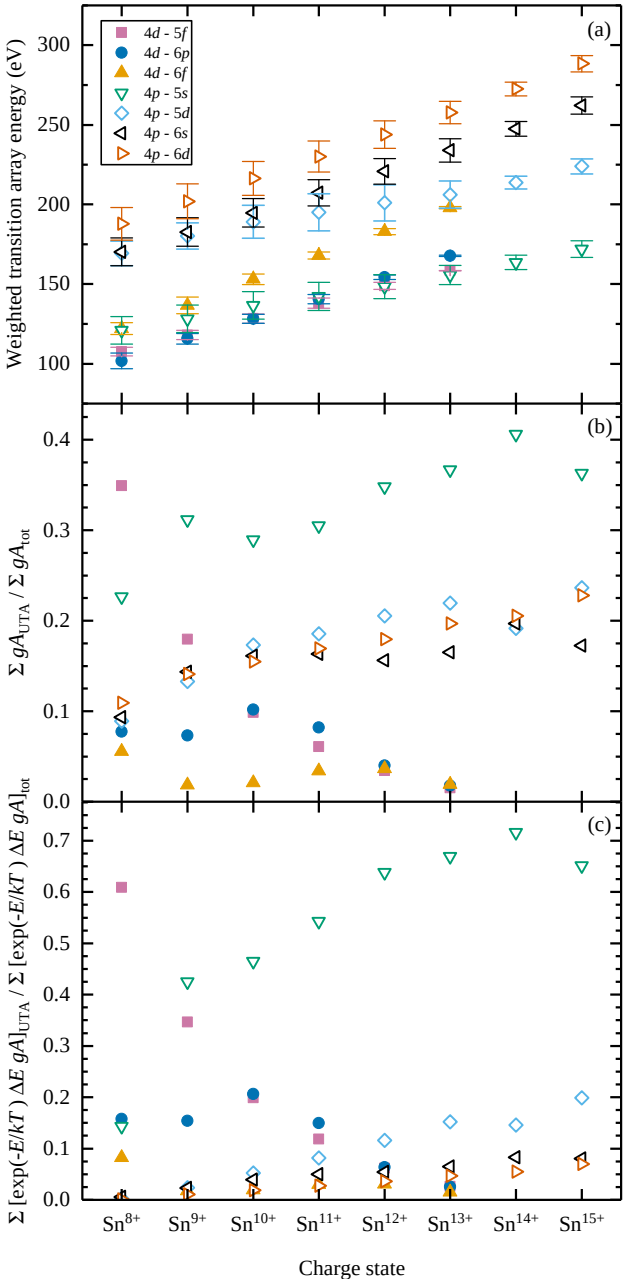

FIGURE 3.2 (Caption on the following page).

FIGURE 3.2 (Figure on the previous page) Scaling of the properties of the investigated transition arrays along the isonuclear sequence of the Sn ions observed in the experimental spectrum. The legend denotes the transition arrays according to the nomenclature used in the main text. (a) Weighted transition array energies μ_1 (see section 3.5) with the error bars indicating the width of the arrays, expressed as the Gaussian standard deviation σ. (b) Relative contributions of transition arrays for each ion in terms of weighted transition rates gA. (c) Relative array intensities for each ion calculated assuming the excited states relative populations to be in accordance with local thermodynamic equilibrium scaling (see main text).

For each ion Fig. 3.2(b) shows the relative contributions of the arrays using the sum of their UTA transition rates ΣgA_{UTA} relative to the total ΣgA_{tot} for all the UTAs here investigated of that charge state. The transition array with the highest relative contribution is the $4p$–$5s$ array with the sole exception of Sn^{8+}, for which the largest contribution comes from the $4d$–$5f$ array. Relatively large weighted transition rates are seen also for the other core-excited transitions $4p$–$5d$, $4p$–$6s$, and $4p$–$6d$. In previous work [41] only the arrays $4d$–$5f$ and $4p$–$6d$ were taken into account to explain their experimental result. These configurations, according to our FAC calculations, are of significance primarily for the ions Sn^{8+}–Sn^{11+} but cannot be expected to sufficiently explain the features even for these charge states. For all the ions investigated, using the weighted transition rates we show that the core-excited, open-$4p$-shell configurations play a significant role in interpreting the high-energy out-of-band EUV emission of these Sn ions. We note that the energies of the associated configurations scale steeply with ionic charge. This means that we have to take into account the fact that the transition energies quickly move over the wavelength band studied in this work, as well as that the relative populations of the excited states need to be considered carefully.

LTE considerations

To obtain the actual expected emission characteristics in a plasma, weighted transition rates of the relevant UTAs alone are not sufficient, and the relative population of the excited states needs to be considered. A straightforward approach is provided by the local thermodynamic equilibrium (LTE) assumption, the conditions for which are expected to be well met in the extremely high-density plasma created by the Nd:YAG laser pulse [128] where collisional processes outpace the relevant atomic decay rates by orders of magnitude. In this case, the population of the excited states can be approximated by the related

Maxwell-Boltzmann statistics. The intensity I_{ij} of a single transition between atomic states i and j can subsequently be expressed as [31]

$$I_{ij} = n_i \Delta E_{ij} A_{ij} \propto \exp(-E_i/kT) \Delta E_{ij} g_i A_{ij}, \tag{3.1}$$

where n_i is the population of the excited state, ΔE_{ij} is the transition energy, E_i is the energy of the excited state and kT is the temperature associated with the emitter. From a preliminary comparison between calculations and the experimental spectrum, it becomes apparent that the wide wavelength range of the line emission is characterised by a very broad charge state distribution: in the spectrum, features belonging to Sn^{8+} through Sn^{15+} are tentatively observed. This broad distribution hints to the fact that the spectrum cannot be modelled by a single temperature, and that the different charge states exist in regions of the plasma where the temperature and density allow them to exist in the first place. Thus, in the following, the temperature kT in equation (3.1) is assumed to be the temperature at which the average charge state in the plasma is equal to the ion under consideration. The required relation between average charge state $\bar{Z}$ and temperature kT is determined from thermodynamic considerations of the equation of state of Sn in reference [129], obtaining the following relationship:

$$kT(\mathrm{eV}) = 0.56 \cdot \bar{Z}^{5/3}. \tag{3.2}$$

As is shown in Fig. 3.2(c), once this scaling is applied, the $4p$–$5s$ re-enforces its position as dominant contribution to the ions' emitted radiation. The arrays $4d$–$5f$ and $4d$–$6p$ are relatively bright for the lower charge states Sn^{8+}–Sn^{11+}, whilst the core-excited transitions become more relevant for the higher charge states.

3.4 Comparison

Fig. 3.3 shows the comparison between resulting LTE-weighted FAC calculations and the experimental spectrum. The former contribution is broken down into its individual charge state constituents for which we show drop-line plots of the three largest contributing configurations in each case. Only the top 95% of the transition rates is shown for improved visibility. The envelopes shown, again per charge state, are the results of convolving, for all contributing configurations, the quantities $\Delta E_{ij} \exp(-E_i/kT) g_i A_{ij}$ with a Gaussian function having width equal to the instrument resolution. The sum of all the normalised envelopes without any further weighting factors is shown as the solid trace (dark-orange) below the experimental spectrum. This trace is only arbitrarily scaled with a common, unity multiplication factor and shifted upwards using a constant offset for improved visibility without the use of any free fit-parameters.

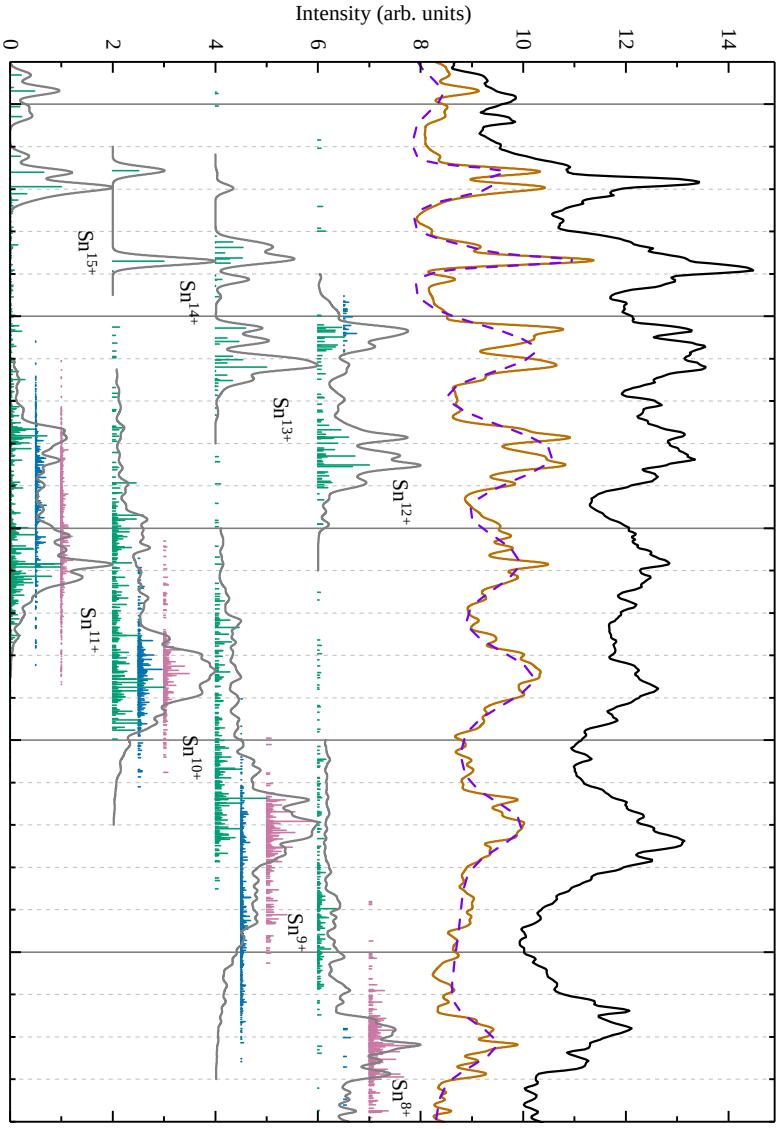

FIGURE 3.3 (Caption on the following page).

FIGURE 3.3 (Figure on the previous page) The topmost black line shows the short wavelength features from the experimental spectrum in Fig. 3.1 in the 7–12 nm range. The bar plots show the LTE-weighted transition rates for the three strongest transition arrays of each ion (see main text and Fig. 3.2): top, in pink, $4p^6\ 4d^m$–$4p^6\ 4d^{m-1}\ 5f$; middle, in blue, $4p^6\ 4d^m$–$4p^6\ 4d^{m-1}\ 6p$; bottom, in green, $4p^6\ 4d^m$–$4p^5\ 4d^m\ 5s$. For clarity, only the top 95 % of the transition rates is shown. Solid grey lines represent the envelopes for each charge state, determined by the convolution of all the transition arrays (see main text) with Gaussian curves. The sum of all the normalised envelopes, scaled with a single multiplication factor and shifted upwards with an offset for improved visibility, is shown by the dark-orange line below the experimental data. The purple dashed line is the result of using the spectral shape parameters (table 3.2) introduced in section 3.6.

Nearly all sub-structures visible within the experimental spectrum can be linked to their theoretical counterparts. We note that this treatment treatment does not include opacity effects. This is justified by previous experimental and theoretical studies of tin plasmas [28, 119], where it was shown that opacity does not play a significant role in the 7–12 nm region, quite unlike the case of the 12–15 nm region spanned by the UTAs relevant for the in-band emission. The agreement of our calculations with the experiment supports this statement.

Remarkably, our equivalent summation of the various normalised contributions reproduces the experimental spectrum quite well. This observation hints at a broad and relatively flat charge state distribution, which in part may be due to the time- and space-integrating nature of our measurement, thus averaging over large temperature and density gradients that are characteristic for these laser-produced plasmas [130]. The detailed explanation of this observed feature is left for future work, as enabled by the here presented line identification. Minor wavelength shifts between calculated features and measurement are apparent, with an average absolute difference of 0.04 nm. Such a difference on the parts-per-thousand level is excellent considering the limited number of configurations used in our calculations, and surpasses the absolute accuracy obtained with FAC in complex ions where configuration interaction is prominent [131]. We conclude that the line features in our final synthetic spectrum are in excellent agreement with the experimental spectrum, strongly supporting our identifications of both charge states and electronic configurations.

3.5 UTA formalism

Having obtained an excellent replication of the experiment using our calculations, we will next employ the Bauche-Arnoult UTA formalism [31, 76, 122] to interpret our calculation results. The transition arrays presented in the previous sections are here characterised using the moments of their distribution [31, 76]. The nth-order moment μ_n of the energy distribution of $E1$ transitions between configurations A and B is expressed as

$$\mu_n\left(A \to B\right) = \frac{\sum_{i,j} \left|\langle i \left|\mathbf{D}\right| j\rangle\right|^2 \left[\langle i \left|\mathbf{H}\right| i\rangle - \langle j \left|\mathbf{H}\right| j\rangle\right]^n}{\sum_{i,j} \left|\langle i \left|\mathbf{D}\right| j\rangle\right|^2}, \tag{3.3}$$

where $\mathbf{D}$ is the electric dipole operator, $\mathbf{H}$ the Hamiltonian matrix, i and j denotes the atomic states belonging to configurations A and B, respectively. The moment μ_n can also be conveniently expressed in terms of transition energies and weighted transition rates [132]:

$$\mu_n\left(A \to B\right) = \frac{\sum_k (\Delta E_k)^n g A_k}{\sum_k g A_k}, \tag{3.4}$$

with ΔE_k the energy of the kth $E1$ transition (between atomic states i and j), g the statistical weight of the transition upper level and A_k the Einstein's coefficient.

The first moment of the distribution, μ_1, is the $E1$-strength-weighted average energy of the transition array. The width of the transition array is represented by the standard deviation of the distribution, i.e. the square root of the variance:

$$\sigma = \sqrt{V} = \sqrt{\mu_2 - (\mu_1)^2}. \tag{3.5}$$

Finally, the asymmetry of the distribution is described by the skewness α_3 [122]:

$$\alpha_3 = \frac{\mu_3 - 3\mu_1 V - (\mu_1)^3}{V^{3/2}}. \tag{3.6}$$

These quantities are helpful in the statistical representation of the transition array using a single skewed Gaussian curve [122]:

$$f(E) = \left\{1 - \frac{\alpha_3}{2}\left(\frac{E-\mu_1}{\sigma} - \frac{(E-\mu_1)^3}{3\sigma^3}\right)\right\} \exp\left[-\frac{(E-\mu_1)^2}{2\sigma^2}\right]. \tag{3.7}$$

An example of the application of this representation is given in Fig. 3.4 for the three main transition arrays here studied of Sn^{10+}. It illustrates well the huge

simplification that is still able to capture the emission characteristics using but three parameters, which are listed for all studied transition arrays and for all investigated Sn ions in Table 3.1. The suitability of this approach in replicating the total ion emission, as shown in Fig. 3.4 by the solid grey and dotted orange curves, is discussed in the following section.

3.6 Spectral shape parameters

The statistical quantities in the UTA formalism are useful to present in a concise manner the result of our FAC calculations, thus providing information about the atomic physics aspects behind the emission of these Sn ions. Whilst these values could be used to interpret experimental data, it is necessary to take into account the relevant configuration arrays by scaling their relative contributions accordingly to our LTE arguments (see Fig. 3.2(c)). Even doing so, the UTA formalism would provide limited detail in the comparison with experimentally measured emission intensities as is illustrated in Fig. 3.4. We instead provide a more straightforward and more apt comparison which can be used to identify the individual contributions of the Sn^{8+}–Sn^{15+} charge states. We use the LTE-weighted emission intensities obtained convolving all the investigated transition arrays, i.e. the Gaussian envelopes shown in Fig. 3.3. These envelopes can be conveniently described by fitting two Gaussian curves, obtaining the very good qualitative agreement shown in Fig. 3.4. The equation for these Gaussian fits reads

$$f(\lambda) = \Sigma_i A_i \exp\left[-\frac{(\lambda - \lambda_{c,i})^2}{2w_i^2}\right], \tag{3.8}$$

with λ being the wavelength, and i=1,2. The list of coefficients A_i, $\lambda_{c,i}$, w_i is given in table 3.2. No simple scaling of these parameters with temperature is obtainable. Therefore, to extend this approach to arbitrary kT values, our calculations need to be re-evaluated starting from equation (3.1).

Despite their artificial meaning, these parameters can be very useful to easily diagnose the emission of Sn LPPs in this wavelength region. Whilst the substructure of the emission is lost the major features and characteristics are preserved, with much more detail and accuracy than in the skewed Gaussian representation using the UTA formalism. Fig. 3.4 shows this aspect, with the skewed Gaussian curve overestimating the contribution in the short wavelength region, thus shifting the centre of mass of the emission to shorter wavelength. The data as provided is self-consistent, in the sense that the relative amplitudes of the Gaussian fits agree with the relative contribution to the spectrum of the different ions. Potentially, combining this tool with absolutely calibrated spectral

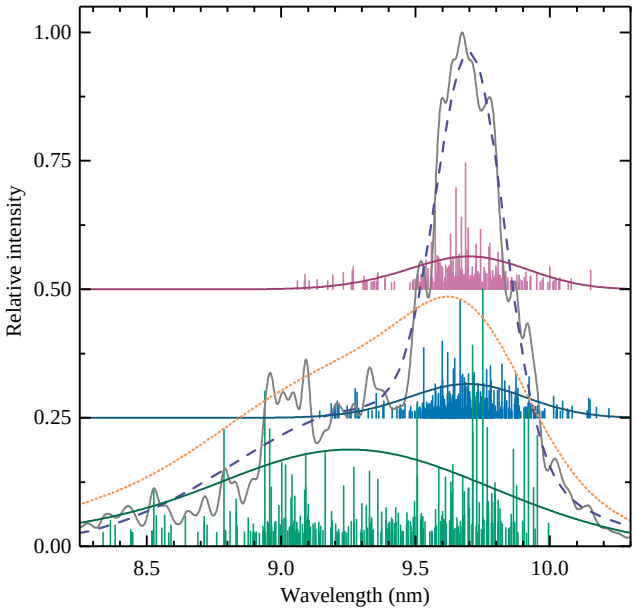

FIGURE 3.4 Details of the emission of Sn^{10+} in the 8.2–10.4 nm region. The Gaussian envelope of the emission (solid gray line, from Fig. 3.3) is mainly determined by the LTE-weighted transition rates of the three strongest transition arrays, here shown as the bar plots: in pink (top) $4p^6\,4d^4$–$4p^6\,4d^3\,5f$, in blue (middle) $4p^6\,4d^4$–$4p^6\,4d^3\,6p$, and in green (bottom) $4p^6\,4d^4$–$4p^5\,4d^4\,5s$. Only the top 95 % of the transition rates is shown. Each transition array is also represented using their respective skewed Gaussian from equation 3.7 with the relevant parameters from table 3.1, scaled accordingly to their relative gA contribution. Also shown is the total sum of the skewed Gaussians (dotted orange curve). The double Gaussian fit (purple dashed line) is determined by the spectral shape parameters in table 3.2. All the curves have been scaled to conserve the integral emission of the transition arrays.

TABLE 3.1 UTA properties for all the $E1$-contributing transition arrays investigated with the flexible atomic code for the ions Sn^{8+} to Sn^{15+}. Weighted mean energy μ_1, standard deviation σ, skewness α_3 and total number of lines N are here presented in accordance with the UTA formalism [76] (see section 3.5).

	Sn^{8+}				Sn^{9+}				Sn^{10+}			
UTA	μ_1 (eV)	σ (eV)	α_3	N	μ_1 (eV)	σ (eV)	α_3	N	μ_1 (eV)	σ (eV)	α_3	N
$4d$–$5f$	107.6	2.7	-0.520	5034	118.0	2.9	-0.214	5313	128.3	3.0	0.323	3247
$4d$–$6p$	101.7	4.9	-0.576	3226	115.7	3.3	0.090	3366	128.2	2.9	0.209	2275
$4d$–$6f$	122.0	3.7	0.310	5614	136.6	5.2	0.091	5423	153.0	3.3	-1.077	2672
$4p$–$5s$	121.0	8.6	0.779	4752	128.2	8.6	0.869	6304	136.6	8.6	0.746	3897
$4p$–$5d$	169.3	7.7	-0.541	20806	180.2	8.2	-0.530	28983	189.1	10.4	-0.487	21257
$4p$–$6s$	170.3	8.7	0.741	6192	182.7	8.9	0.797	8288	194.8	8.9	1.018	5664
$4p$–$6d$	187.9	10.2	0.418	21424	202.0	10.9	0.449	29012	216.4	10.6	0.584	21331

	Sn^{11+}				Sn^{12+}				Sn^{13+}			
UTA	μ_1 (eV)	σ (eV)	α_3	N	μ_1 (eV)	σ (eV)	α_3	N	μ_1 (eV)	σ (eV)	α_3	N
$4d$–$5f$	138.0	3.1	0.314	870	148.8	2.2	-1.061	96	158.4	0.1	10.042	3
$4d$–$6p$	140.6	2.9	-0.539	644	154.3	1.5	-1.369	64	167.8	0.5	2.351	3
$4d$–$6f$	167.9	2.2	-0.606	679	182.9	1.9	-0.770	89	198.0	0.7	0.715	5
$4p$–$5s$	142.3	8.8	0.953	1620	148.4	7.5	1.371	377	155.7	6.0	1.315	37
$4p$–$5d$	195.0	11.7	-0.025	8098	201.0	11.4	0.486	1546	206.2	8.5	1.373	132
$4p$–$6s$	207.3	8.3	1.170	2112	220.8	8.0	1.283	403	233.9	7.3	1.471	38
$4p$–$6d$	230.1	9.7	0.947	8126	243.8	8.7	1.299	1564	257.8	7.1	1.628	132

	Sn^{14+}				Sn^{15+}			
UTA	μ_1 (eV)	σ (eV)	α_3	N	μ_1 (eV)	σ (eV)	α_3	N
$4p$–$5s$	163.6	4.5	0.541	3	172.0	5.2	0.678	14
$4p$–$5d$	213.8	4.0	1.037	7	224.0	4.7	0.790	39
$4p$–$6s$	247.5	4.6	0.715	3	262.2	5.4	0.744	14
$4p$–$6d$	272.5	4.3	0.932	7	288.4	5.1	0.750	40

measurement could yield valuable information regarding the relative charge state populations in the plasma, and the magnitude and nature of the radiation continuum underlying the atomic line emission. These aspects are topics of future investigations.

TABLE 3.2 Coefficients of the Gaussian fits to the envelopes of the LTE-weighted intensities for all ions investigated (see Fig. 3.3 and section 3.4) evaluated at the temperature kT determined from equation (3.2). The amplitudes A_i are scaled to agree with the relative contribution to the spectrum of each ion.

Ion	kT (eV)	A_1	$\lambda_{c,1}$ (nm)	w_1 (nm)	A_2	$\lambda_{c,2}$ (nm)	w_2 (nm)
Sn^{8+}	17.8	0.115	11.438	0.748	0.247	11.438	0.094
Sn^{9+}	21.7	0.346	10.400	0.105	0.244	10.400	0.560
Sn^{10+}	25.9	0.267	9.321	0.496	0.763	9.705	0.127
Sn^{11+}	30.3	1.000	9.155	0.136	0.641	8.647	0.158
Sn^{12+}	35.1	0.700	8.100	0.086	0.775	8.650	0.127
Sn^{13+}	40.1	0.408	7.709	0.052	0.426	8.210	0.085
Sn^{14+}	45.3	0.123	7.313	0.019	0.244	7.740	0.019
Sn^{15+}	50.9	0.234	6.950	0.078	0.628	7.380	0.055

3.7 Conclusions

We present the results of spectroscopic measurements in the extreme ultraviolet regime of the emission of the plasma created from molten Sn droplets when irradiated by a high-energy pulse from a Nd:YAG laser at its fundamental wavelength. Using the flexible atomic code, electric dipole transition from excited configurations towards the ground states in the ions Sn^{8+}–Sn^{15+} were investigated. Including a simple local thermodynamic equilibrium scaling for the relative populations of these excited states, we have shown that the most intense contribution to the radiation in the 7–12 nm region can be attributed to the radiative decay of the core excited configuration [Ar] $3d^{10}\ 4s^2\ 4p^5\ 4d^m\ 5s$ towards the ground state in the ions here studied. Moreover, the transition energies and rates from FAC calculations, scaled with LTE population, reproduce very well the unresolved transition arrays measured experimentally. The unresolved-transition-array formalism is subsequently used to present in a concise manner the result of our atomic structure calculations. Furthermore, spectral shape parameters of double Gaussian fits to the LTE-weighted emission spectra of each Sn ion are provided, enabling straightforward interpretation of our results. These parameters also provide simplified spectral information to interpret emission from industrial plasma EUV light sources which may facilitate their optimization. Our findings thus further the understanding of the atomic structure of Sn ions and their emissions in the context of laser-produced plasma and EUV sources.

3.8 Acknowledgments

This work has been carried out at the Advanced Research Center for Nanolithography (ARCNL), a public-private partnership of the University of Amsterdam (UvA), the Vrije Universiteit Amsterdam (VU), the Netherlands Organisation for Scientific Research (NWO) and the semiconductor equipment manufacturer ASML.

We would like to thank J.C. Berengut (University of New South Wales, Sydney) for the fruitful conversation during the early stages of the manuscript. We would also like to thank T.A. Cohen Stuart, R. Jaarsma, the AMOLF mechanical and design workshop, the software and electronics departments for technical support.

CHAPTER FOUR

SPECTRAL CHARACTERIZATION OF AN INDUSTRIAL EUV LIGHT SOURCE FOR NANOLITHOGRAPHY

F. Torretti, F. Liu, M. Bayraktar, J. Scheers, Z. Bouza, W. Ubachs, R. Hoekstra, and O. O. Versolato

Submitted (Aug 2019)

The emission spectra from an industrial, droplet-based, laser-produced plasma, extreme ultraviolet light source for nanolithography are here presented and analyzed. The dependence of spectral features on the CO_2-drive-laser intensity is studied by changing the beam spot size at constant pulse energy and duration. We characterize the spectrum by fitting the results of atomic structure calculations to the short-wavelength region (7–11 nm), where the contributions from various charge states can be resolved, and obtain the relative contributions of charge states Sn^{9+}–Sn^{15+}. These relative contributions are compared to charge state populations as calculated with the non-equilibrium plasma kinetics code FLYCHK. The calculations are shown to be in good qualitative agreement with the results, showing that the effective plasma temperature, and with it, the shape of the unresolved, main emission feature at 13.5 nm, is a remarkably weak function of laser intensity under this source normal operating conditions.

4.1 Introduction

Extreme ultraviolet (EUV) lithography [14, 133] is the main candidate for replacement of current 193 nm immersion lithography [17, 38, 39, 117], with further miniaturization and fewer processing steps enabled by the shorter wavelength of the radiation. In nanolithographic applications, EUV radiation is generated using laser-produced plasma (LPP) light sources. In state-of-the-art industrial LPP, molten tin micro-droplets are first pre-deformed into disk-like targets by a low-intensity laser *prepulse*, in order to ensure optimal coupling with the following high-intensity (10^9–10^{10} W/cm^2) *main pulse*. The resultant hot, high density LPP efficiently emits EUV radiation around 13.5 nm due to the atomic line emission from the highly-charged Sn^{9+}–Sn^{14+} ions [30, 32–37, 119, 120]. This radiation conveniently overlaps with the peak reflectivity of molybdenum-silicon multi-layer mirrors [16, 118], characterized by a 2 % reflectivity bandwidth centered at 13.5 nm wavelength and employed as projection optics in EUV lithography scanners [14]. On the path towards high-volume EUV lithography, source characterization, physical understanding and improvement are important targets [18]. Amongst other techniques, spectroscopic measurements of the source emission spectrum are a powerful tool to diagnose source conditions [27]. Moreover, the projection optics [14] and EUV pellicle [134] in the scanner are sensitively dependent on the spectral emission characteristics as, e.g., the out-of-band EUV spectrum, i.e. photons outside the 2 % reflection bandwidth, may influence coating lifetime and further introduce undesirable thermal effects [135, 136].

We present spectra obtained from an industrial LPP EUV light source. The analysis revolves around the short wavelength emission features found in the 7–11 nm range. The result of atomic structure calculations given in Ref. [137] are used to characterize the charge state contribution to the spectrum by employing a fitting procedure. Using the non-equilibrium plasma kinetics code FLYCHK [138], the fit results are compared to the calculated charge state populations, thus obtaining an effective plasma temperature and scaling thereof with laser intensity.

4.2 Experiment

The plasma emission spectra have been acquired from an industrial ASML "S2" EUV source driven by a 10.6-μm-wavelength CO_2-gas-laser [139] with EUV power of 100 W at the intermediate focus, i.e. the power delivered by the source to the scanner. The source is operated with a repetition rate of 50 kHz, with Sn droplets of 20–30 μm in diameter [17]. The initially-spherical droplet is pre-

deformed into a thin, disk-like target about 300 μm in diameter using a 10-μm laser *prepulse* of few tens of mJ. This prepulse is followed by a 10-μm, high-energy, high-intensity *main pulse* which creates the plasma necessary for EUV emission. The main pulse energy is kept constant throughout the experiments at approximately 500 mJ. Its temporal profile also remains unchanged, which exhibits a strong peak decaying over a several-10-ns time scale. In order to probe different plasma temperatures, and therefore charge state populations, the main pulse beam-size on target is scanned by changing the position of the last optical elements along the laser propagation direction. This operation results in the main pulse beam-spot at Sn target being monotonically scanned, going from approximately 200 μm to 400 μm diameter. Changes in the spatial size of the main pulse will affect its intensity, the parameter pertinent for setting plasma temperature [128]. In the rest of this chapter, due to the fact that the laser-pulse duration remains unchanged, average laser fluence at the target will be employed as the relevant quantity. In the performed scan, the fluence is varied between approximately $300\,\mathrm{J/cm^2}$ to $800\,\mathrm{J/cm^2}$. The total EUV energy in the 2 % band at the intermediate focus per pulse is in the range of 2.5 mJ to 2.8 mJ.

Throughout the experiment, while the laser beam-spot is changed, the source is operated to maximize in-band EUV output for each given experimental condition. This is achieved by adjusting the alignment of the droplet and prepulse laser in the plane perpendicular to laser propagation direction. By adjusting alignment between the droplet and the prepulse, the disk-like target will exhibit a tilt with respect to the main pulse propagation direction [26]. Due to this tilt, the cylindrical symmetry of the main pulse-target interaction is broken, and the spectral emission may be expected to suffer from anisotropy. Angular dependence of the EUV emission in the 2 % band in this type of sources is a well-established fact, even in perfectly cylindrically-symmetric interactions [27, 140]; moreover, there are no studies dedicated to the investigation of the anisotropy of the full EUV emission spectrum. Therefore, dedicated measurements were performed to study the aforementioned angular properties and, more precisely, the effects of the optimization procedure. Keeping all other parameters constant, the laser-to-droplet alignment is changed as performed during the optimization procedure. The resulting target tilt is inspected using a shadowgraphic technique [23], imaging the Sn disk at 90° with respect to the laser direction. Anisotropy of the emission after irradiating the tilted targets with the main pulse was found to mainly affect the total amount of radiation emitted but has negligible impact on the spectral characteristics of the emission. Fig. 4.1 shows the relative emission spectra obtained for three distinct target tilts, illustrated by the shadowgraphic images in the figure legend.

The spectra were measured from a view-port positioned 90° to the drive laser axis using a broadband transmission grating spectrometer [27, 141, 142].

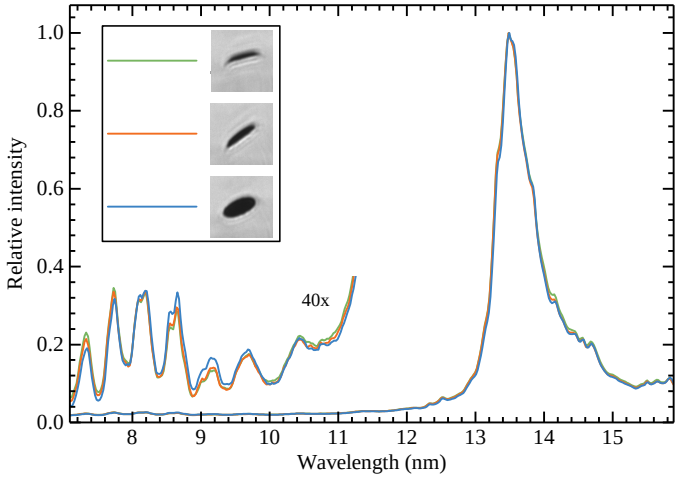

FIGURE 4.1 Three normalized spectra obtained under the same experimental conditions except for the target tilt. Shadowgraphic images of the pre-deformed target, obtained at 90° with respect to the main drive laser, show in the figure legend the different tilts just before the main pulse arrival. The short-wavelength emission features are magnified by a factor 40 to be visible on the same scale.

The spectrometer was operated with a 50-μm-wide entrance slit and a near-normal-incidence 10 000 lines/mm grating resulting in an instrument resolution of 0.11 nm full-width-at-half-maximum at a wavelength of 13.5 nm [27]. The diffracted light was subsequently recorded by a back-illuminated charge coupled device (CCD) from Princeton Instruments (PIXIS-XO: 2KB) with 2048x512 pixels. The camera was cooled to -17 °C to reduce the thermal noise. The spectrometer was aligned to observe the zero-order light close to the edge of the camera to help with the wavelength calibration. For each source setting, dark background frames were recorded by placing on the spectrometer line of sight a Si window of 2 mm thickness that absorbs light below 1.1 μm wavelength. These background frames were then subtracted from the recorded spectra to eliminate the dark counts and read-out noise. The resulting images were cropped and averaged over the non-dispersive axis to yield the raw spectra. The dispersive axis of the raw spectra was calibrated using the geometrical parameters of the spectrometer and applying the grating equation, obtaining a wavelength calibration uncertainty of 0.02 nm. The intensity axis of the spectra was corrected for the diffraction efficiency of the grating and quantum efficiency of the camera [143].

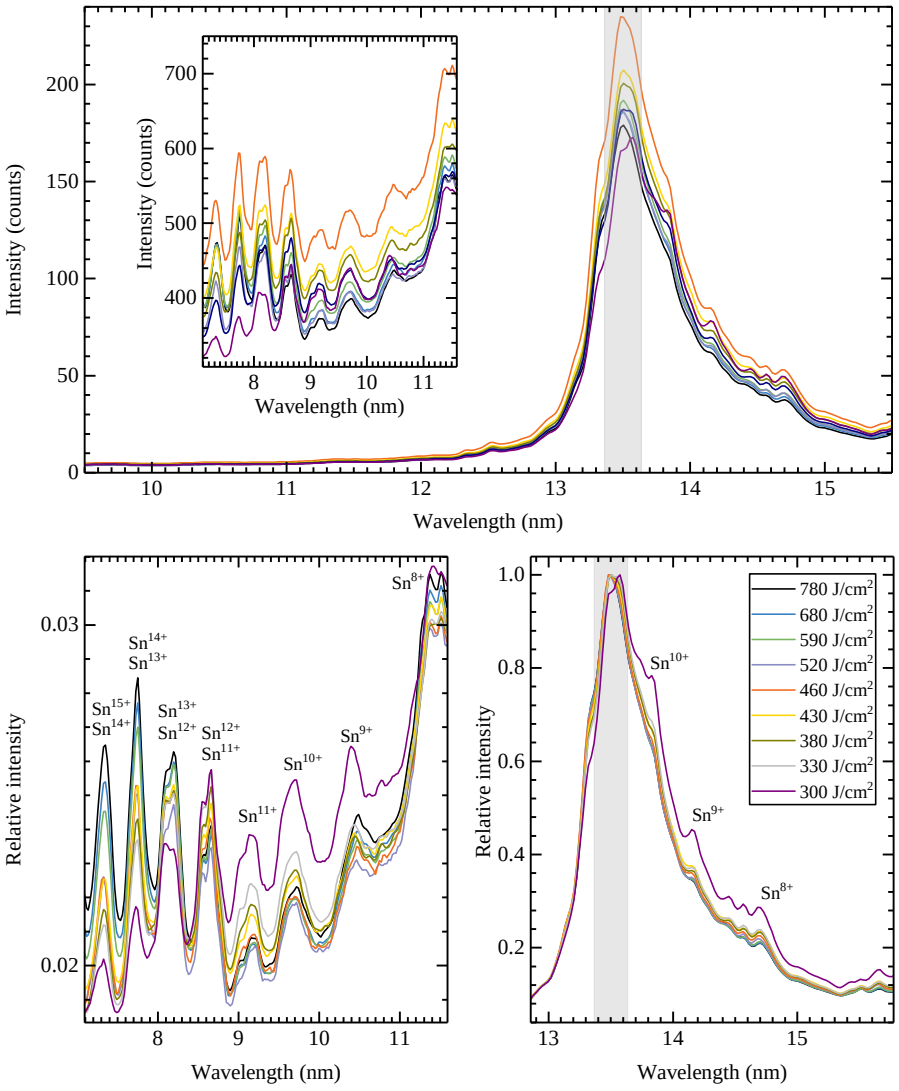

FIGURE 4.2 Top: absolute intensity spectra recorded for different laser fluences. Due to the large differences, the short wavelength emission features are presented in the appropriately scaled inset. Bottom: zoomed views for the short wavelength region and for the main emission feature, both normalized to the peak intensity at 13.5 nm. The gray shaded areas highlight the 2-% band around 13.5 nm.

4.3 Results

Spectra obtained at different laser fluences are shown in Fig. 4.2. The dominant contribution to the spectrum is clearly the narrow emission feature centered around 13.5 nm wavelength. This emission feature is composed of thousands of atomic transitions in the ions Sn^{8+}–Sn^{14+} [27, 30, 32, 34, 120], which are clustered together in what are commonly known as unresolved transition arrays (UTAs) [76]. The lower charge states Sn^{8+}–Sn^{10+} mainly radiate photons with wavelengths longer than 13.5 nm [32, 120], whereas the ions Sn^{11+}–Sn^{14+} contribute to radiation in the 2 % reflectivity bandwidth [34, 120].

Due to the changes in total emission intensity, relative changes between the spectra are better observed by normalizing each data set to its maximum value. In this representation, many interesting different aspects of the main emission feature become immediately apparent. Most laser fluences produce spectra with only very minor differences, with the exception of the lowest fluence in which the stronger contribution of lower charge states is observed in the long-wavelength tail of the emission. The features observed in this portion of the spectrum are well matched to strong transitions in Sn^{8+}–Sn^{10+} [32, 120].

The short-wavelength emission features between 7 and 11 nm, despite their much lower emission intensity, show much more drastic changes than the main feature at 13.5 nm. Moreover, the features observed in this region are charge state resolved even for the ions Sn^{11+}–Sn^{15+} [137], allowing for further information to be distilled. The spectrum produced by the lowest laser fluence is easily recognized by the stronger contribution from lower charge states Sn^{9+}–Sn^{11+} [137]. The strong presence of these charge states in both the main feature and the short wavelength region clearly indicates that the plasma temperature is too low for optimal source performance. Higher temperatures are necessary in order to increase the plasma average charge state and improve the source brightness at 13.5 nm.

Examination of the short-wavelength emission features also shows that, particularly when looking at emission from higher charge states, this spectral region is much more sensitive to laser fluence, and thus plasma temperature, changes. Therefore, the analysis of the features in the 7–11 nm range can be valuable to infer properties of the laser-produced plasma. This analysis is performed by employing the atomic data calculated in Ref. [137], where more detail on the atomic structure responsible for the emission features can be found. In short, these features stem from electric dipole transitions to the ground configurations of the ions Sn^{8+}–Sn^{15+}. The strongest transitions are in the form of $4p \rightarrow 5s$ and $4d \rightarrow 5p$. To perform the present analysis, the transition energies and probabilities from the calculations in Ref. [137] are employed.

In order to properly compare the atomic data with experimental spectra,

some sort of scaling argument for the populations of excited states should be invoked. In Ref. [137], local thermodynamic equilibrium (LTE) was used as, in the case of higher-density, 1-μm-wavelength-driven LPP, the collision frequencies overcome spontaneous emission rates. Griem's criterion [144] states that, for the transitions here investigated, equilibrium should exist for electron densities above few times $10^{20}\,e/\mathrm{cm}^3$. In the present case, the strong reduction of the relevant plasma density due to the longer wavelength of the CO_2 drive-laser effectively breaks this assumption. In general, one would need a full collisional-radiative modeling approach, including the detailed atomic structure of all ions participating and all the relevant atomic plasma processes connecting said ions and their energy levels. This approach is extremely challenging and very computationally expensive, and lies beyond the scope of this work. For simplicity, the following approximations are used: first, using the non-equilibrium code FLYCHK [138], the average charge state as a function of electron temperature is calculated for a $10^{19}\,e/\mathrm{cm}^3$ plasma; the level populations of each charge state are then weighted as if in LTE, applying the temperature found from FLYCHK. This approach may be expected to under- or overestimate the actual population of excited states but, when looking only at relative intensities and given that the individual spectra extends over a very limited wavelength range, the errors introduced should be tolerable. The calculated spectra for the charge states Sn^{9+}–Sn^{15+} are shown in Fig. 4.3, already weighted using the appropriate Boltzmann factors (as determined from FLYCHK temperatures). Note that these calculated spectra have been manually shifted on average by 0.05 nm to match the experimentally observed features to ensure the convergence of the fitting procedure described in the following.

The calculated spectra are subsequently used as input in a non-linear least-squares fitting routine which employs seven free-fit-parameters, one for each charge state. A linear combination of the calculated spectra is obtained which matches the experimental spectra. This procedure is quite robust, converging successfully for all spectra. An exemplary fitting result is shown in Fig. 4.3. The gray shaded area represent the continuum pedestal on which the atomic line emission rests. This continuum needs to be introduced as another fit-parameter to ensure the convergence of the fit. For the typical plasma densities and temperatures of a CO_2-produced-plasma, there is no clear physical reason for continuum radiation to exist as bound-bound transitions fully dominate emissivity. It is worth pointing out that the continuum levels almost perfectly correlate to the total amount of light recorded by the camera, which might then indicate the presence of stray light inside the spectrometer. Regardless of the underlying cause, the presence of the continuum pedestal does not affect the results of the analyses here presented.

From the fit parameters it is possible to extract the radiative contribution

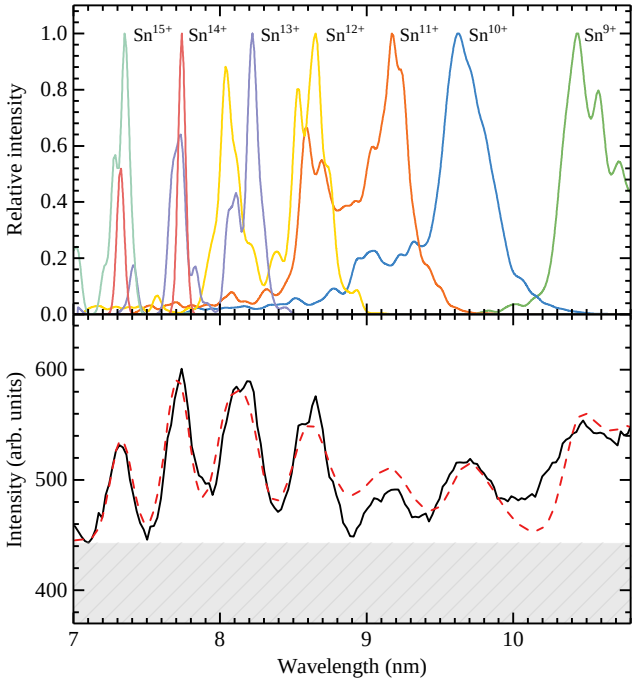

FIGURE 4.3 Top: individual charge state spectra calculated with the atomic data from Ref. [137] and weighted using Boltzmann statistics (see main text). Bottom: exemplary case, showing the result of fitting the short wavelength region to the spectrum obtained at 460 J/cm^2. Solid black line: experimental spectrum; dashed red line: fitted spectra; gray shaded area: fitted continuum level (see main text).

of each charge state to the short-wavelength range, see Fig. 4.4. These calculated contributions act as a simple proxy for the charge states populations in the LPP. We note that some of the results show limitations of the method here employed. Firstly, the contributions from lower charge states, in particular that from Sn^{9+}, seem to be overestimated. This could be due to the fact that these emission features are on top of the left-hand shoulder of the main emission feature centered at 13.5 nm. This extra contribution beneath would make them appear brighter. Secondly, the contribution from Sn^{11+} is fairly constant for all laser fluences, which could be an artifact from our fitting procedure. Moving towards the higher charge states, the contributions obtained however seem to be well-suited to qualitatively describe the change in charge state populations due

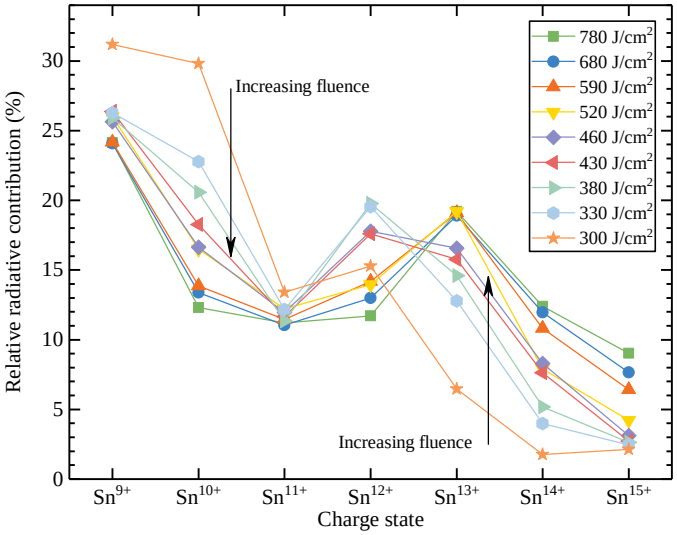

FIGURE 4.4 Relative radiative contribution of each charge state to the emission between 7 and 11 nm as determined from the fitting procedure for all laser fluence values.

to changing laser fluence, and thus, changing plasma temperature. For this reason, we will now focus on these contributions and compare the corresponding fit results to the relative charge state populations as function of plasma temperature as obtained from FLYCHK calculations for a plasma with $10^{19}\,e/\mathrm{cm}^3$ electron density.

A comparison between the experimental data and the calculations is shown in Fig. 4.5, where the radiative contributions obtained from the fit results have been re-normalized for the charge states Sn^{11+}–Sn^{15+} such that their sum yields one for each experimental realization. When comparing these to the results from FLYCHK, it is seen that the general trends of the various charge states are well captured by the fitting procedure employed: Sn^{12+} contributions monotonically decrease from a 40% contribution value as laser fluence is increased; Sn^{13+} increases, then peaks at $520\,\mathrm{J/cm}^2$ before slowly falling again; Sn^{14+} and Sn^{15+} both monotonically increase over the measured range. Such behavior is observed also in our calculations, indicating that a 30–42 eV temperature range was probed (shown as a shaded gray area in Fig. 4.5).

The dependence of the effective plasma electron temperature on the applied laser fluence can be deduced from these data, e.g., from the ratio between the contributions from Sn^{13+} and Sn^{12+}, by comparing our experimental results

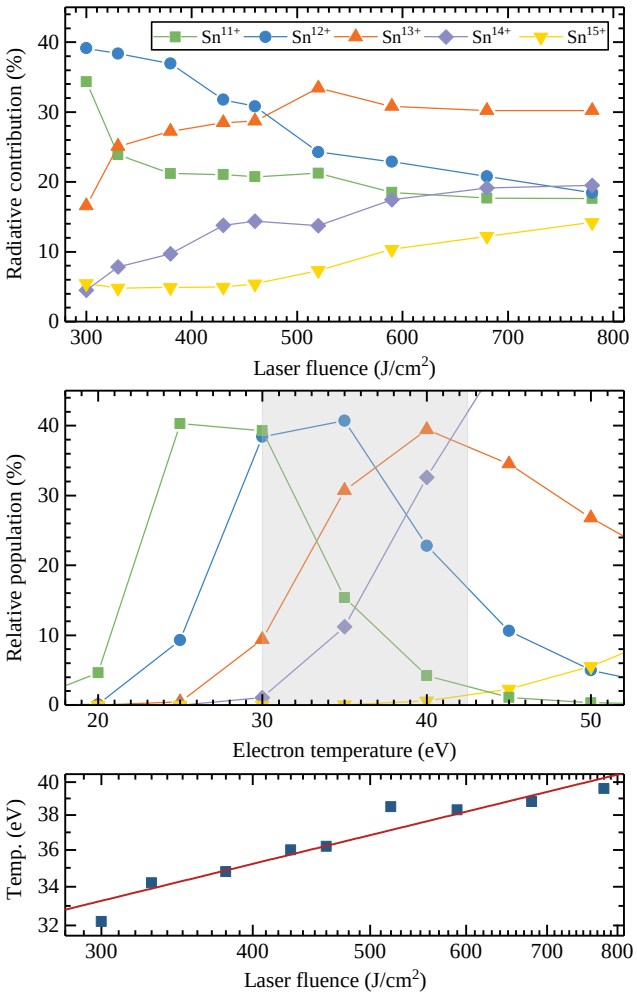

FIGURE 4.5 Qualitative comparison between the fitting procedure and FLYCHK calculations. Top: relative radiative contribution of the charge states Sn^{11+}–Sn^{15+}. Middle: relative charge state population from FLYCHK as function of electron temperature for a $10^{19}\ e/cm^3$ density. The gray shaded area highlights the portion of the calculation that correlates to the range of experimental data shown in the upper panel. Bottom: scaling of electron temperature with laser fluence as deduced from the ratio of Sn^{13+} contribution to that of Sn^{12+} (see main text). The red solid line shows $T \propto F^{0.2}$.

to FLYCHK calculations. We note that normalization factors and any associated systematic uncertainties identically drop out in this ratio. In the range observed, this leads to a monotonically increasing ratio Sn^{13+}/Sn^{12+} for both experimental data and results from calculations.

Through these calculations, each experimental point can be associated with a unique temperature value, and therefore a relationship between temperature and fluence is established as presented in the bottom panel of Fig. 4.5. A monotonic increase of temperature, in the range 30–40 eV, with laser fluence ranging 300–800 J/cm^2 is observed. This suggests a surprisingly weak scaling $T \propto F^{0.2}$ of the effective plasma temperature T with fluence F. Recalling that in our framework fluence is a proxy for laser intensity (trivially, intensity $I \propto F$), this value can be compared to temperature-intensity relationships found in literature. The scaling found here is far weaker than the $T \propto F^{3/5}$ predicted by the collisional-radiative modeling approach [128] that is often cited in the literature. It is also lower than other approaches, such as the analytic results from Mora [145] resulting in a power of 4/9 or the 0.53 value found by Basko and coworkers [129]. Note that the aforementioned theory scaling powers do not include (changes in) radiative loss fraction [25, 129] which may lower the calculated value. On the other hand, the actual scaling may be expected to be weaker still as we use emission as a proxy of charge state balance, uncorrected for a hypothesized faster increase of the population of the more highly excited states with temperature. Such detailed calculations are however outside of the scope of the current work and are not expected to change our main conclusions. A partial explanation for the observed weak scaling may be found in the temporal shape of the laser pulse which first strongly peaks to decay over a longer, several-10-ns time scale. Thus, a wide range of instantaneous laser intensities is effectively probed in a single laser pulse and this may influence the effective, average, plasma temperature. Care should be taken applying these results outside of the studied case as the scalings found are tied to the presented experimental conditions, namely the operational conditions of this EUV source.

4.4 Conclusions

The emission spectra in the 7–16 nm range from an industrial EUV light source are presented. The short-wavelength emission features in the 7 to 11 nm region are shown to strongly change with laser intensity and offer the possibility to individually diagnose several Sn charge states that strongly contribute to the main, unresolved emission feature at 13.5 nm wavelength relevant for nanolithography. Using the available atomic data for these emission features and the result of non-equilibrium plasma kinetics calculations with the code FLY-

CHK, synthetic spectra are generated for each charge state contributing in the 7–11 nm spectral region. The calculated spectra are then fitted to the experimental spectra, obtaining radiative contribution for each charge state. The changes of these contributions as function of the laser intensity are compared to the calculated charge state populations and their dependency on electron temperature. The data are in good qualitative agreement, showing that the effective plasma temperature is remarkably weakly dependent on laser intensity in the source here investigated.

4.5 Acknowledgments

The authors would like to thank ASML EUV System Power group and Proto-21 team for their support and thank Igor Fomenkov for in-depth technical discussions. The used transmission grating spectrometer has been developed in the Industrial Focus Group XUV Optics at University of Twente, and supported by the FOM Valorisation Prize 2011 awarded to F. Bijkerk and NanoNextNL Valorization Grant awarded to M. Bayraktar in 2015. Part of this work has been carried out at the Advanced Research Center for Nanolithography (ARCNL), a public-private partnership of the University of Amsterdam (UvA), the Vrije Universiteit Amsterdam (VU), the Netherlands Organisation for Scientific Research (NWO) and the semiconductor equipment manufacturer ASML. This project has received funding from European Research Council (ERC) Starting Grant number 802648 and is part of the VIDI research programme with project number 15697, which is financed by NWO.

Chapter Five

Radiation transport and scaling of optical depth in Nd:YAG laser-produced microdroplet-tin plasma

R. Schupp, F. Torretti, R. A. Meijer, M. Bayraktar, J. Sheil, J. Scheers, D. Kurilovich, A. Bayerle, A. A. Schafgans, M. Purvis, K. S. E. Eikema, S. Witte, W. Ubachs, R. Hoekstra, and O. O. Versolato

Applied Physics Letters **115**(12), 124101 (2019), edited by F. Torretti

Experimental scaling relations of optical depth are presented for the emission spectra of a tin-droplet-based, 1-μm-laser-produced-plasma extreme-ultraviolet (EUV) light source. Observed changes in the complex spectral emission of the plasma over a wide range of droplet diameters (16–65 μm) and laser pulse durations (5–25 ns) are accurately captured in a scaling relation featuring the optical depth of the plasma as the single, pertinent parameter. The scans were performed at constant laser intensity of $1.4 \cdot 10^{11}$ W/cm^2 that maximizes the emission in a 2 % bandwidth around 13.5 nm, the bandwidth relevant for industrial EUV lithography, relative to the total spectral energy. Using a one-dimensional radiation transport model, the relative optical depth of the plasma is found to linearly increase with droplet size, with a slope that increases with laser pulse duration. For small droplets and short laser pulses the fraction of light emit-

ted in the 2 % bandwidth around 13.5 nm relative to the total spectral energy is shown to reach values of more than 14 % that may enable conversion efficiencies of 1-μm-wavelength laser light into industrially-useful EUV radiation which could rival those of current state-of-the-art 10-μm-wavelength-driven sources.

5.1 Introduction

The semiconductor industry is currently moving from deep ultraviolet to extreme ultraviolet (EUV) lithography for high-volume manufacturing of the next generation of microelectronics, in which the shorter wavelength of the EUV radiation enables further miniaturization. The light sources of choice for the nanolithographic applications are laser-produced plasmas (LPPs) [18, 30, 32–41, 45, 79, 119, 120, 146, 147]. In these sources, tens-of-micrometer-sized tin droplets are irradiated by high-intensity ($10^{10}\,\mathrm{W/cm^2}$) laser pulses, in order to generate a high-density ($10^{19}\,e/\mathrm{cm^3}$) plasma that efficiently emits EUV radiation [148]. Tin is used because several of its charge states have many dipole transitions such as the $4d$–$4f$, $4p$–$4d$, and $4d$–$5p$ transition arrays in Sn^{8+}–Sn^{15+} that strongly emit around 13.5 nm [30,37], a wavelength that matches the peak reflectivity of available Mo/Si multilayer optics [16, 118] used in state-of the-art EUV-lithography machines. The light of interest within the 2 % reflectivity bandwidth of these mirrors is referred to as *in-band* radiation.

Currently, CO_2-gas lasers operating at 10 μm wavelength are used to drive the EUV-emitting plasma but with further developments regarding their output power, YAG solid-state lasers operating at 1 μm may become a viable alternative in the future. YAG laser systems provide a smaller footprint, a higher efficiency in converting electrical power to laser light, and very good temporal pulse shaping capabilities. The shorter wavelength of YAG lasers also gives rise to a 100-time increase in critical plasma density ($n_{\mathrm{crit}} \propto \lambda^{-2}$) compared to CO_2 driven plasmas, and higher laser intensities of typically $10^{11}\,\mathrm{W/cm^2}$ are needed to efficiently produce in-band radiation. The higher critical density results in a much greater, nearly complete absorption of the laser light by the tin target through the mechanism of inverse bremsstrahlung [125,145]. A possibly adverse effect of this large critical density is the creation of EUV radiation in plasma regions characterized by large optical depths, which could lead to significant self-absorption of the emitted radiation. This results in broadening of the spectral emission out of the 2 % bandwidth of interest, thus reducing the *spectral purity* (SP) of the EUV plasma source [28, 29, 124, 149]. SP is defined as the ratio of in-band energy over the total EUV energy emitted into the half-sphere back toward the laser, which is covered by multilayer optics in industrial sources. Considering conservation of energy, SP represents the absolute upper limit to the *conversion efficiency* of

laser light into in-band radiation: $\mathrm{CE} \leq \mathrm{SP}$, where CE approaches SP only if all light is emitted in the backwards-facing 2π steradian [27]. A more stringent limit of $\mathrm{CE} \leq \mathrm{SP}/2$ is found in case of spherically symmetric emission [125]. Given the importance of SP as indicator for source performance, its scaling with relevant source parameters such as tin-droplet size, laser pulse duration and laser-beam spot-size needs to be quantified and understood. In spite of its importance, literature covering the emission properties of LPP from high-purity tin microdroplets, the industrial targets of choice, remains scarce [140, 150, 151].

In this chapter a systematic study of the influence of droplet size and laser pulse duration on the emission spectrum of a droplet-based, Nd:YAG-driven EUV source is presented. An analytical solution for radiation transport in an optically-thick, one-dimensional plasma is used to quantify the opacity-driven broadening of key emission features.

5.2 Experiment

In the experiment spherical micrometer-sized tin droplets were irradiated with high intensity laser pulses from a Nd:YAG laser system [152] operated at 1064 nm as described in Ref. [23, 27]. The laser pulse was temporally box-shaped and of adjustable duration. It had a spatially flat-top shape of 96 μm diameter to homogeneously heat the plasma. The spectral emission from the plasma was observed with a transmission grating spectrometer [142] under 60° with respect to the incoming laser beam. The measured spectra were corrected for the first and second order diffraction efficiencies of the grating, as well as for the quantum efficiency of the camera. The wavelength axis of the spectra was calibrated in a separate experiment using atomic line emission from an aluminum plasma. After all corrections, the SP values were calculated with respect to the measured spectral range of 5.5 to 25.5 nm.

Using a laser intensity of $1.4 \cdot 10^{11}$ W/cm^2 at which SP is optimal [27], two sets of experiments were conducted. Firstly, spectra were measured for several laser pulse durations within the range of 5 to 25 ns while keeping the droplet diameter fixed at 46 μm. As seen in Fig. 5.1(a), the main emission feature at 13.5 nm broadens for longer laser pulse duration while all other spectral emission features stay remarkably similar even though the laser pulse duration was varied by a factor of five. This indicates that laser intensity is the pertinent parameter of the investigated LPP determining charge state distribution and temperature of the plasma [27, 128]. Secondly, spectra were measured for various droplet sizes in the range of 16 to 65 μm at constant laser pulse durations of 5, 15 and 25 ns. Spectra for the 15 ns case are shown in Fig. 5.1(b). A striking similarity in spectral structure is observed among plasmas formed on droplets of various sizes.

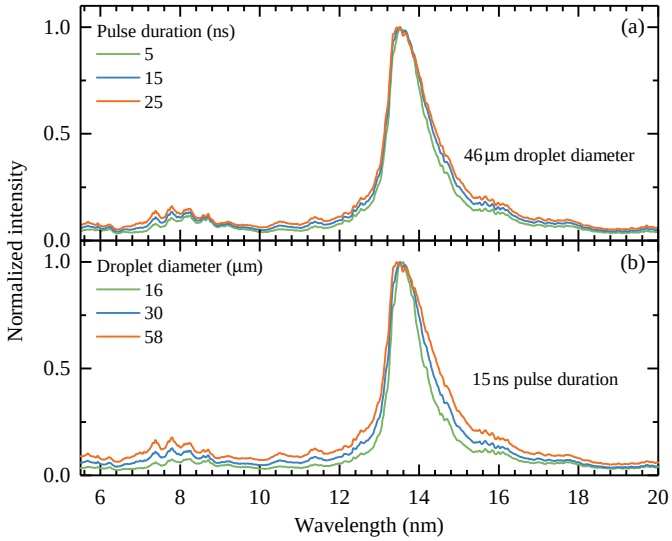

FIGURE 5.1 Selection of emission spectra of Nd:YAG laser-produced plasma from tin microdroplets irradiated at constant laser intensity of $I = 1.4 \cdot 10^{11}\,\mathrm{W/cm^2}$ while varying either (a) laser-pulse duration or (b) droplet diameter.

With increasing droplet size the main spectral feature at 13.5 nm broadens and the short-wavelength radiation between 5.5 and 12 nm increases in intensity, relatively to the main emission feature.

5.3 Methods

The observed broadening of spectral features for increased pulse duration and droplet size, illustrated in Fig. 5.1, can be connected to an increase in the optical depth of the emitting plasma. The spectral radiance L_λ of a plasma with significant absorption and re-emission can be calculated using the equation of radiation transport. The subscript λ indicates the wavelength dependency of L_λ. The solution for a homogeneous one-dimensional plasma can be given in analytic form [153]:

$$L_\lambda = S_\lambda \left[1 - \exp(-\tau_\lambda)\right], \tag{5.1}$$

where $S_\lambda = \eta_\lambda/\alpha_\lambda$ is the source function defined by the ratio of emissivity η_λ and the absorptivity α_λ. Opacity is defined as $\kappa_\lambda = \alpha_\lambda/\rho$, where ρ is the plasma mass density. In local thermodynamic equilibrium (LTE), where the atomic

levels are thermally populated, the source function S_λ equals Planck's spectral radiance B_λ. We assume that such LTE holds for the high-density, strongly collisional Nd:YAG-driven plasma. In the exponent, τ_λ is the wavelength-specific optical depth given by $\tau_\lambda = \int \alpha_\lambda \mathrm{d}x$ where the absorptivity α_λ is integrated over the plasma length. Rearranging Eq. (5.1), the optical depth of the observed plasma can be obtained from its spectral radiance via

$$\tau_\lambda = -\ln\left(1 - \frac{L_\lambda}{B_\lambda}\right), \tag{5.2}$$

with the ratio L_λ / B_λ being defined as *relative spectral radiance*.

The optical depths of plasmas of same temperature and density can only differ by a wavelength-independent factor a_i, here defined as *relative optical depth* and related to the possibly different plasma lengths, connecting different optical depths via $\tau_{\lambda,i} = a_i\, \tau_{\lambda,0}$. It follows from Eq. (5.2) that

$$\frac{L_{\lambda,i}}{B_\lambda} = 1 - \left(1 - \frac{L_{\lambda,0}}{B_\lambda}\right)^{a_i}. \tag{5.3}$$

It is instructive to use Eq. (5.3) to interpret the experimentally-observed spectral changes, thus hypothesizing that plasma length-scale is the pertinent parameter determining the spectral variations.

At the wavelength λ_p of peak radiance near 13.5 nm, the optical depth typically has high values as follows from the work of Colgan *et al.* [119]. Their calculation results indicate a peak opacity value of approximately $5 \cdot 10^5\,\mathrm{cm}^2/\mathrm{g}$ at a relevant $0.01\,\mathrm{g/cm}^3$ ion density. Thus, taking a reasonable $20\,\mu\mathrm{m}$ plasma length [125], we deduce a typical value $\tau_{\lambda_p} \approx 10$ such that $L_{\lambda_p} = B_{\lambda_p}$ in Eq. (5.1) to very good approximation. Therefore, we proceed by normalizing the experimentally-observed spectra $O_{\lambda,i}$ to their value at 13.5 nm, after division by the blackbody spectral radiance B_λ. This procedure allows to obtain the normalized relative spectral radiance $L_{\lambda,i}/B_\lambda$ directly from the emission recorded by the spectrometer $O_{\lambda,i}$, with other factors such as source size or overall detection efficiency conveniently dropping out.

Using Eq. (5.3) any spectrum can be expressed in terms of any other spectrum via the relative optical depth a_i. The value of a_i can be obtained with respect to a chosen reference spectrum from a fit of Eq. (5.3) to the relative spectral radiance $L_{\lambda,i}/B_\lambda$. As reference, for which $a_i = 1$, the spectral emissivity $L_{\lambda,0}/B_\lambda$ of the spectrum with the narrowest main emission feature is used in the following, i.e. the one measured at 5 ns pulse duration and 16 µm droplet size. Typical literature values for the electron temperatures at which Nd:YAG LPPs most efficiently emit in-band radiation vary between 28 and 40 eV [119, 125, 154, 155].

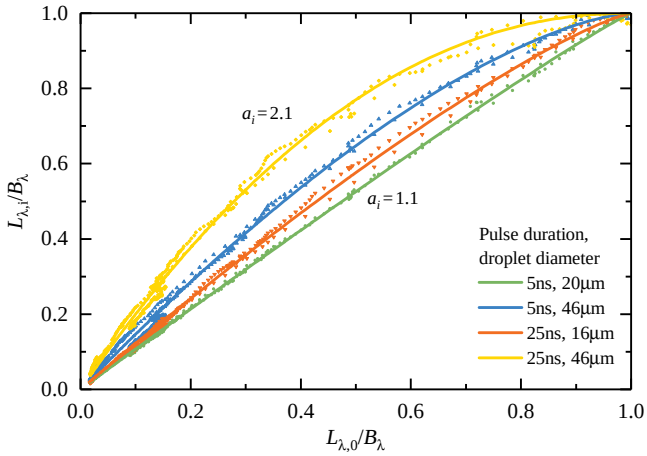

FIGURE 5.2 Relative spectral radiance $L_{\lambda,i}/B_\lambda$ of experimental spectra taken at constant laser intensity for different laser pulse durations and droplet sizes (see Fig. 5.1). The spectral emissivities are plotted with respect to the one of a reference spectrum $L_{\lambda,0}/B_\lambda$ obtained at 5 ns laser pulse duration and 16µm droplet diameter (at which conditions the main emission feature at 13.5 nm is narrowest). For the blackbody function B_λ, a temperature of 34 eV was used. The solid lines depict fits of Eq. (5.3) to the data featuring the relative optical depth a_i as single free fit parameter.

A temperature in the center of this range of 34 eV is chosen for B_λ for all spectra. A common temperature is used because the laser intensity, which sets the effective plasma temperature, remains constant for all measurements. Variation of the blackbody temperature within the stated limits changes the fitted relative optical depth (see below) by less than 3 %.

5.4 Results

Fig. 5.2 shows exemplary data of $L_{\lambda,i}/B_\lambda$ versus $L_{\lambda,0}/B_\lambda$ for a wide range of droplet sizes and pulse durations. Excellent agreement between the data and the model fit, which features the relative optical depth a_i as single free-fit parameter, is observed. The thus obtained a_i values enable reproduction of spectra measured at other droplet sizes and laser pulse durations by radiation transport of the reference spectrum. Inserting the relative optical depth obtained from the fits into Eq. (5.3) and multiplying by B_λ leads to an excellent reproduction of other experimental spectra as seen in Fig. 5.3(a,b). This is especially true for the

main emission feature around 13.5 nm. When comparing the transported spectrum in the short-wavelength region between 5 and 12 nm, minor differences are visible for increasing pulse duration in Fig. 5.3(a), and slightly more pronounced differences are observed for increasing droplet size in Fig. 5.3(b). This may be explained by changes in the plasma other than a simple optical depth scaling, such as emission from a multi-temperature plasma or a slight dependence of plasma charge state distribution with droplet size and pulse duration.

Comparison of the relative intensities of the short-wavelength features suggests that the average charge state slightly increases with droplet size [27, 137]. To account for a possibly higher average charge state of the plasma at longer pulse duration and larger droplet size, the scaled reference spectrum may instead be compared to spectra taken at lower laser intensity. Indeed, comparing to spectra taken at a laser intensity of $1.1 \cdot 10^{11}\,\mathrm{W/cm^2}$ leads to an excellent agreement over the entire spectral range measured. We thus observe that the short-wavelength band between 5 and 12 nm is a much more sensitive probe to the emission properties of Sn LPPs than the main emission feature at 13.5 nm.

In Fig. 5.4(a) the fitted values for spectra of all pulse durations and droplet sizes are summarized. The relative optical depth a_i appears to scale linearly with droplet radius and to strongly depend on the pulse duration. Linear fits are in good agreement with the data and converge to a common intercept of approximately 0.7 at zero droplet diameter. The fit coefficients monotonically increase with pulse duration from 0.017 to 0.025 and $0.030\,\mu\mathrm{m}^{-1}$ for 5, 15 and 25 ns, respectively.

Having identified the optical depth as the pertinent scaling parameter for Nd:YAG laser-produced tin plasmas, the spectral purity of the emission spectrum is related to this parameter in Fig. 5.4(b). Using this scaling all experimental $\mathrm{SP}_{5.5\text{-}25.5\mathrm{nm}}$ values, calculated over a range of 5.5 to 25.5 nm as denoted by the subscript, collapse onto the gray, dashed curve obtained by calculating the $\mathrm{SP}_{5.5\text{-}25.5\mathrm{nm}}$ of the radiation transported reference spectrum.

It is instructive to compare the $\mathrm{SP}_{5.5\text{-}25.5\mathrm{nm}}$ scaling captured by the gray, dashed curve with the SP value of a spectrum from a state-of-the-art, $\mathrm{CO_2}$-laser-driven EUV source. The plasmas of such sources are expected to have small optical depth $\tau < 1$ and thus less broadening, considering the 100-fold decrease in critical density compared to the Nd:YAG case. These $\mathrm{CO_2}$-driven sources are, in general, characterized by relatively high SP and CE values. The spectrum (see Fig. 5.5) was obtained by pre-deforming a tin droplet with a low intensity $\mathrm{CO_2}$ laser *prepulse*, leading to a disk-shaped target of approximately 200 µm in diameter. To produce EUV radiation, the flat target was subsequently irradiated by a high-intensity, 100 ns, 320 mJ *main pulse* with a beam size that matched the target size. In this case, the spectrum was measured over a wavelength range spanning 6.8 to 16.7 nm. The fraction of light emitted in the 2 % bandwidth

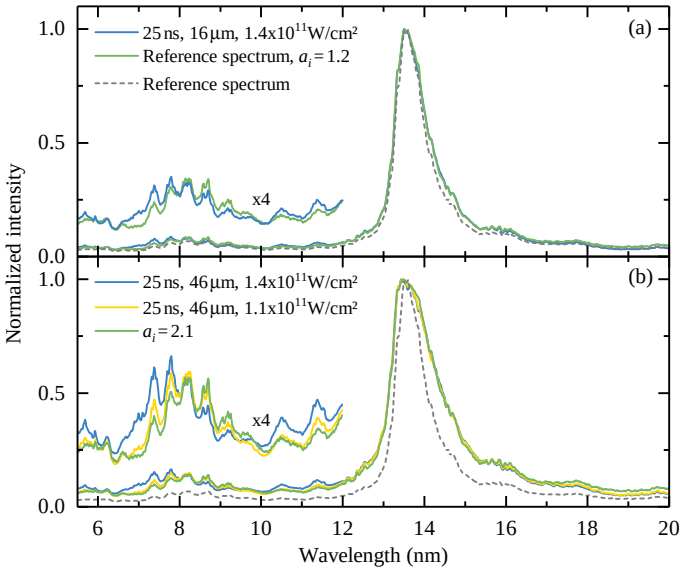

FIGURE 5.3 Comparison of the reference spectrum and the radiation-transported reference spectrum with other measured spectra. The reference spectrum was transported using Eq. (5.3) employing the relative optical depth as determined in Fig. 5.2 for (a) increasing laser pulse duration, and (b) increasing laser pulse duration and droplet size. An additional spectrum is shown measured at the lower laser intensity of $1.1 \cdot 10^{11}$ W/cm^2, which provides a better match with the radiation transported spectrum in the 5 to 12 nm range.

around 13.5 nm relative to the total spectral energy in this measured bandwidth is $\mathrm{SP}_{\text{6.8-16.7nm}} = 23\,\%$. For a relative optical depth $a_i = 0.6$, the Nd:YAG reference spectrum is found to closely match this $\mathrm{SP}_{\text{6.8-16.7nm}}$ performance (also see Fig. 5.5). Over the extended wavelength range of 5.5 to 25.5 nm that defines SP in this work, this scaled Nd:YAG LPP spectrum has $\mathrm{SP}_{\text{5.5-25.5nm}} = 16.5\,\%$. The reference spectrum for $a_i = 0.6$ closely resembles the CO_2 spectrum. This is a remarkable finding as the plasma conditions for the two cases are vastly different, such as the LTE and $\tau \gg 1$ not being met by the CO_2 case.

Calculating the maximally obtainable conversion efficiency via $\mathrm{CE} = \mathrm{SP}/2$ [27, 125], a significantly higher maximum CE value is expected for CO_2-driven LPPs, given its higher SP. However, accounting for the fraction of laser light ε absorbed by the tin target, near unity (> 0.9 [25]) for the case of 1 µm radiation while about 0.7 for 10 µm light [156], both drive laser cases may indeed have about the same conversion efficiency limit of $\mathrm{CE} = \varepsilon \mathrm{SP}_{5.5-25.5\mathrm{nm}}/2 \approx 6\,\%$,

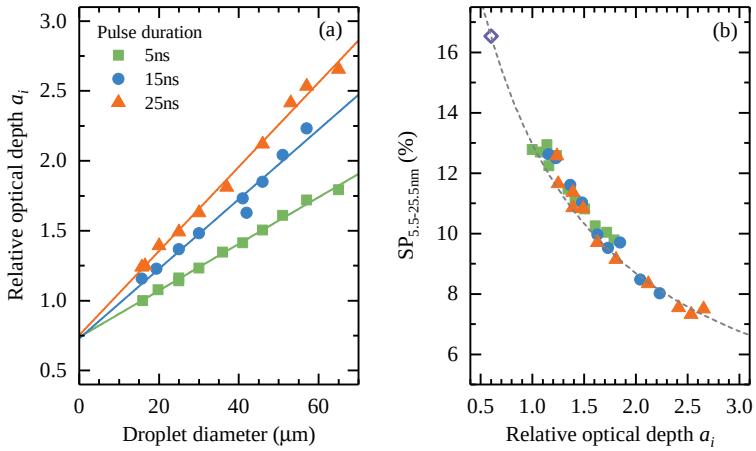

FIGURE 5.4 (a) Dependency of the relative optical depth a_i on droplet diameter for various laser pulse durations as obtained, e.g., in Fig. 5.2. The solid lines show a linear extrapolation of the data toward zero droplet size. (b) Experimental values for spectral purity ($SP_{5.5\text{-}25.5nm}$) versus relative optical depth. The dashed line represents $SP_{5.5\text{-}25.5nm}$ as calculated from the radiation transported reference spectrum. The open diamond symbol indicates the $SP_{5.5\text{-}25.5nm}$ value of the radiation transported reference spectrum for a relative optical depth parameter $a_i = 0.6$, obtained from comparison of the reference spectrum with the emission of the CO_2-laser-driven plasma as shown in Fig. 5.5 (see main text).

which would make 1 µm solid-state lasers a viable alternative as source drive-laser. Naturally, the maximum obtainable CE depends not only on the emission spectrum as there are further significant contributions to the total energy balance, aside from a finite emission anisotropy. Examples include plasma kinetics, ionization energy, as well as contributions from plasma emission outside the 5.5 to 25.5 nm range. A careful comparison of this total energy balance is required between the CO_2 and Nd:YAG drive laser cases. Further, a central requirement is the creation of manageable amounts of debris from the plasma. This entails, among others, fragments or high-energy particles that could reduce optics lifetime. Laser energy not contributing to radiation may instead lead to the production of fast ionic debris and possible gains in spectral purity and radiative output power should be carefully weighed out against, e.g., increases in the tin load on the optical components.

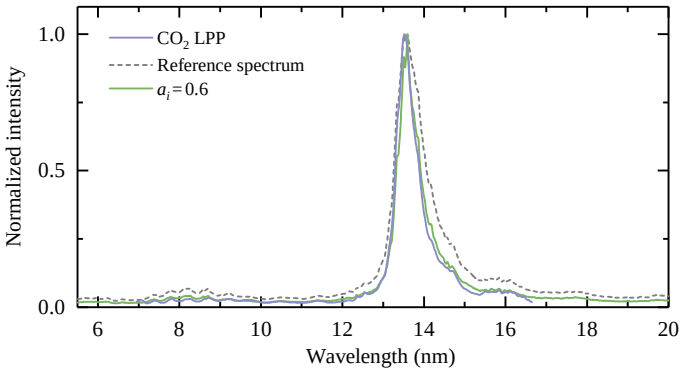

FIGURE 5.5 Comparison of the transported reference spectrum using Eq. (5.3) with $a_i = 0.6$, and the spectral emission from a CO_2-laser-driven plasma.

5.5 Conclusions

Optical depth is established to be the pertinent scaling parameter in high-density laser-produced plasmas from tin-microdroplets. Observed changes in the experimental emission spectra from plasmas originating from various droplet sizes as well as various laser pulse durations are remarkably well described using a one-dimensional radiation transport equation featuring the relative optical depth of the plasma as sole parameter. The excellent description of the experimental data by the model suggests that a dominant fraction of the EUV emission may be produced in a single-density, single-temperature region of the plasma because the underlying opacity does not appear to change. The here established scaling with optical depth indicates that Nd:YAG LPPs may suffer from strong absorption and re-emission significantly redistributing the spectral energy into wavelength-bands other than 13.5 nm in case of large plasma size. Therefore, the optical depth of these light sources needs to be minimized to reach highest SP values which can be done by reduction of laser pulse duration and droplet size. In such optimized cases, and accounting for the difference in laser absorptivity, CE values from Nd:YAG-driven plasma could be obtained such that they rival those of state-of-the-art CO_2-driven plasma sources.

5.6 Acknowledgments

This work has been carried out at the Advanced Research Center for Nanolithography (ARCNL), a public-private partnership of the University of Amsterdam (UvA), the Vrije Universiteit Amsterdam (VU), the Netherlands Organisa-

tion for Scientific Research (NWO) and the semiconductor equipment manufacturer ASML. The part of this work concerning the CO_2 laser-produced plasma has been carried out at ASML San Diego part of ASML US LP. This project has received funding from European Research Council (ERC) Starting Grant number 802648 and is part of the VIDI research programme with project number 15697, which is financed by NWO.

Chapter Six

Unexpectedly large radiative emission between highly-excited states in Sn laser-produced plasma

F. Torretti, J. Sheil, R. Schupp, M. M. Basko, M. Bayraktar, R. A. Meijer, S. Witte, W. Ubachs, R. Hoekstra, O. O. Versolato, A. J. Neukirch, and J. Colgan

Submitted (Aug 2019)

The opacity spectra of Sn plasma in the extreme ultraviolet (EUV) regime are calculated, for local thermodynamic equilibrium conditions, using the Los Alamos suite of atomic codes and its opacity and plasma modeling code ATOMIC. The detailed atomic structure calculations of the complex Sn ions show an unexpectedly large contribution to EUV emission from transitions between highly-excited states, up to approximately 90 % of the total opacity, with the more well-known EUV transitions to the ground manifold contributing only 10 %. The transitions between doubly- and triply-excited states are shown to be serendipitously aligned around 13.5 nm, the wavelength of relevance in EUV light sources for the nanolithographic industry. Our opacity calculations, in conjunction with a radiation transport model, are validated by the comparison with the emission spectra of a droplet-based, laser-produced Sn-plasma light source. The calculations are in excellent agreement with the measurements and show that a single-temperature, single-density plasma can be used to capture the majority of the emission features.

6.1 Introduction

The highly charged ions of Sn and their atomic structure posses particular technological value as the enabler of next-generation nanolithography [14,17,18,22, 39,117,133]. They are employed as emitters of photons in a narrow band closely matching the 2 % reflection bandwidth of multilayer optics [118], centered at 13.5 nm. This short-wavelength radiation will soon be used to imprint smaller features on commercial microchips. The aptness of Sn ions to this application is due to their complex, open-$4d$-subshell structures [32–37, 40, 41, 79, 119, 120]. Within these structures, $\Delta n = 0$ one-electron-excited configurations decay to the ground state manifold via a multitude of transitions clustered together in unresolved transitions arrays (UTAs) [76], centered in the industrially relevant band around 13.5 nm. Moreover, the average excitation energies of these configurations are similar for the ions Sn^{11+}–Sn^{14+}, making these charge states excellent radiators of 13.5 nm photons. In industrial applications, Sn ions are bred in laser-produced plasmas (LPPs) driven by a 10-µm-wavelength CO_2-gas-laser. Switching to solid-state lasers, for example to 1-µm-wavelength YAG, could be beneficial regarding many technological aspects, including a reduction of the device footprint and a strongly increased overall efficiency of converting electrical power to useful extreme ultraviolet (EUV) photons [27]. The tenfold decrease in laser wavelength increases the critical plasma density by approximately two orders of magnitude. In the context of understanding and supporting the drive laser wavelength change in future industrial sources, calculation of complete and accurate opacity spectra and of the atomic data therein is an important and crucial element in simulations of source performance, as these data are needed in radiation hydrodynamics codes [125, 129, 130, 157] and for the calculation of emission spectra. The amount of detail in the atomic structure necessary to ensure accurate simulations is an open question. In fact, long-standing discrepancies exist between the experimental measurements of Sn opacity [28] and various theoretical calculations using atomic structure and plasma codes [28, 119, 158]. This chapter identifies the main culprits of the historical discrepancies and addresses them, in order to generate correct opacity spectra. These spectra are then shown to be in excellent agreement with the emission from a droplet-based EUV source.

6.2 Atomic structure calculations

The level scheme presented in Fig. 6.1 exemplifies the characteristics in the atomic structure that need to be captured to accurately determine the opacities of a Sn plasma for nanolithograpic applications. This structure shows the average

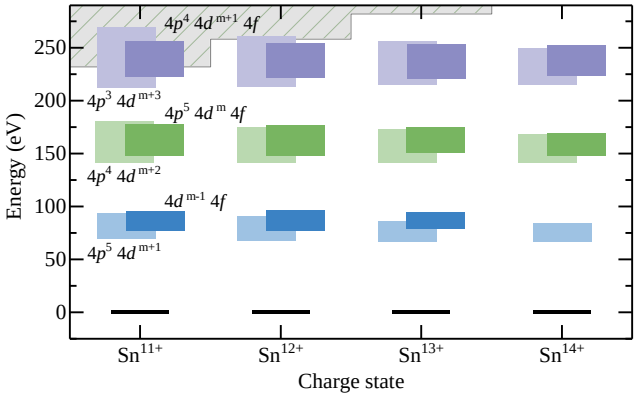

FIGURE 6.1 Schematic energy level diagram of the ions Sn^{11+}–Sn^{14+}. The ground-state configurations of these ions take the form $4d^m$, with $m = 3-0$. The lowest-lying level of each ground-state manifold is shown in black and is fixed at an energy of 0 eV. The energy "spread" of an excited configuration is illustrated by a rectangle, centered at the average energy of the configuration and whose width represents the first moment of the level distributions. The shaded gray area denotes the ionization potentials of the ions.

energies and widths of some of the typical configurations that play a role in the generation of EUV photons. The most notable phenomenon is that the excitation energies of electrons within the $n = 4$ manifold are rather independent of the occupation of the manifold itself: the energy required to promote a $4p$ electron to the $4d$ subshell is almost the same regardless of the number of electrons in any of the other subshells. The highly excited configurations, thanks to their large number of levels and high statistical weights, are able to provide a large contribution to the production of EUV photons by decaying via electric dipole transitions towards the lower levels, which in turn decay again radiating similar energy photons. Beyond the few exemplary configurations shown in Fig. 6.1, other configurations overlap with the ones presented, e.g., configurations with a single excited electron in the $n = 5$ shell.

We present the opacity spectrum of a Sn plasma calculated in local thermodynamic equilibrium (LTE) at conditions relevant for the production of EUV light in an industrial setting. The calculations were performed using the Los Alamos code ATOMIC [159, 160], which takes as input state-of-the-art atomic data calculated with the Los Alamos suite of atomic codes [161,162]. The atomic structure was calculated using the semi-relativistic Hartree-Fock approach im-

plemented in the CATS code (based on Cowan's code [52]). These data are used by ATOMIC to calculate opacity spectra under the assumption of LTE with input from equation-of-state calculations performed with ChemEOS [163,164], which ensures convergence of the partition function and thermodynamic consistency.

In the entire procedure, one of the most challenging aspects is the atomic structure of the highly charged Sn ions, due to their open $4d$-subshells and the existence of strong configuration-interaction (CI) between levels in the $n = 4$ manifold. The difficulties associated with accurate calculations of these level structures were presented in a recent study of Colgan *et al.* whereby Sn opacities, calculated using the aforementioned Los Alamos codes, were shown to be very sensitive on the choice of underlying atomic structure [119]. However, without a suitable experimental benchmark, it was not possible to determine whether sufficient configurations were included in the atomic structure models.

In the current work, to ensure that the position of highly excited levels and their oscillator strengths are calculated to the highest possible accuracy, full CI effects are taken into account for most of the single, double, and triple excitations of valence, $4s$, and $4p$ electrons of the ground-state configuration into the majority of $n = 4$ and $n = 5$ subshells. The list of configurations that were included in the full CI calculation for Sn^{12+} is presented in Table 6.1. This list comprises 94 configurations and generates over $3 \cdot 10^5$ fine-structure levels and more than 10^{10} dipole-allowed transitions. Similar sets of configurations were used for the neighboring ion stages. Moreover, we also included a significant number of other configurations for which the transitions were included using intermediate-coupling [119]. This mixed approach, called '2-mode', maintains the accuracy of CI calculations for the most important transitions in the EUV regime, while retaining other levels that represent more highly excited states that are necessary for an accurate partition function and opacity at higher photon energies. The list of configurations adopted for a given ion stage was determined by systematically increasing the number of configurations allowed to interact, and identifying for which configuration sets the positions of the dominant transitions converge. It is well-known that *ab initio* calculations performed in this manner do not necessarily reproduce experimental spectra to a high degree of accuracy. To circumvent this, it is standard practice in Cowan code calculations to introduce so-called "scaling factors" which pre-multiply the radial integrals appearing in the Hamiltonian matrix elements. As noted by Cowan [52], these scaling factors account for the 'infinity of small perturbations' that are necessarily omitted in practical atomic structure calculations. Normally, a reduction of 10–15 % of the radial integrals, i.e., applying scaling factors of 0.85–0.9, can bring theoretical calculations of level energies (and subsequently calculated transition wavelengths) into very good agreement with experimental observations. In our CATS calculations, the scaling factor is set to a

TABLE 6.1 List of configurations included in the full CI calculation for Sn^{12+}. Here, angular momenta $l = 0 - 4 \rightarrow s - g$.

Inner subshells		Outer subshells
$4s^2\,4p^6$	+	$\{4d^2, 4d\,4f, 4f^2, 4d\,5l, 4f\,5l\}$
$4s^2\,4p^5$	+	$\{4d^3, 4d^2\,4f, 4d\,4f^2, 4d^2\,5l, 4d\,4f\,5l\}$
$4s^2\,4p^4$	+	$\{4d^4, 4d^3\,4f, 4d^2\,4f^2, 4d^3\,5l, 4d^2\,4f\,5l\}$
$4s^1\,4p^6$	+	$\{4d^3, 4d^2\,4f, 4d\,4f^2, 4d^2\,5l, 4d\,4f\,5l\}$
$4s^2\,4p^3$	+	$\{4d^5, 4d^4\,4f, 4d^3\,4f^2, 4d^4\,5l, 4d^3\,4f\,5l\}$
$4s^1\,4p^5$	+	$\{4d^4, 4d^3\,4f, 4d^2\,4f^2, 4d^3\,5l, 4d^2\,4f\,5l\}$
$4s^2\,4p^6$	+	$\{5s^2, 5s\,5l, 5p^2, 5p\,5l, 5d^2, 5d\,5l, 5f\,5g\}$
$4s^2\,4p^5\,4d$	+	$\{5s^2, 5s\,5p, 5s\,5d\}$

standard 0.87 based on previous CATS calculations performed on a wide range of elements and charge states. When using the configuration set in Table 6.1, already much larger than previous calculations presented in Ref. [119], the position of the major transitions to the ground-state configuration (e.g. $4d^2\,{}^1G_4 \rightarrow 4d\,4f\,{}^1H_5$ in Sn^{12+}) are in excellent agreement with the experimental observations in Ref. [34]. Calculations were then performed using ATOMIC including atomic structure data for all relevant ion stages calculated in a manner similar to Sn^{12+}. These calculations produced an intense emission feature, in good qualitative agreement with the measured spectrum apart from a crucial shift in the central position of the emission feature towards shorter wavelength. In fact, the feature was positioned outside the relevant 2 % emission band for nanolithography. Since it was established that the well-known transitions to the ground manifold are correctly calculated, the discrepancy must originate from inaccurate positioning of transitions between excited states.

This unexpected finding led us to re-consider our atomic structure calculations for the excited-excited transitions. Little data for such excited transitions are available for the Sn^{11+}–Sn^{14+} ions. For Sn^{14+}, the calculated electronic structure differed from the interpretation of charge-exchange measurements (and accompanying calculations) of D'Arcy *et al.* [45] by around 2 % in wavelength position. We found that reducing the scaling factors in CATS to 0.75 yielded much better agreement with these data and with the experimental charge-exchange emission spectra of Tanuma *et al.* [37]. This further reduction may account for greater correlation effects between these high-energy configurations, arising from their high density of states.

Adopting scaling factors of 0.87 and 0.75 for the transitions to the ground manifolds and for transitions between excited states, respectively, opacity spec-

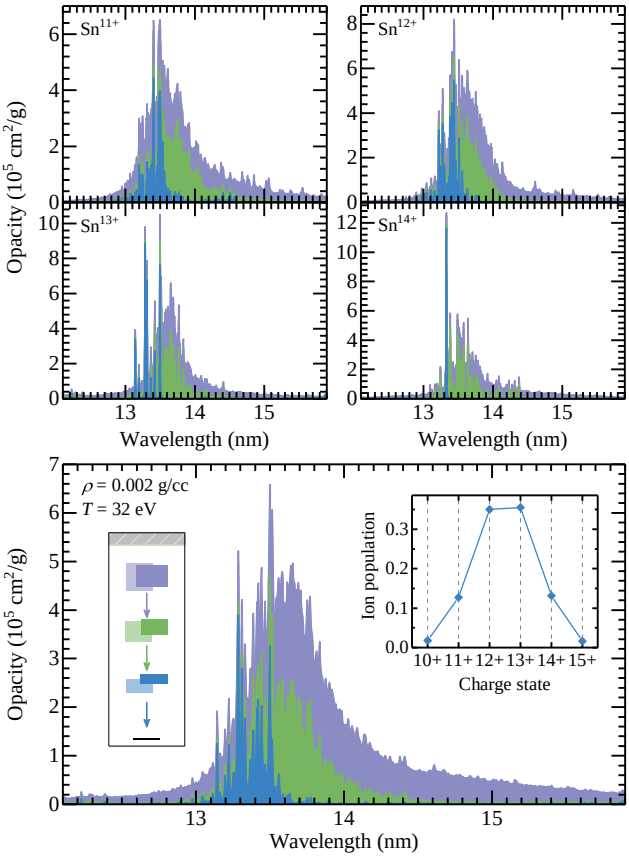

FIGURE 6.2 Opacity spectra calculated for a 32 eV, 0.002 g/cm^3 LTE Sn plasma. The shaded areas represent the cumulative contributions (i.e. the next contribution is plotted stacked on top of the previous one) stemming from different types of excited states. They are divided according to the energy of the lower state into which the ions radiatively decay: in blue, transitions into the ground state manifold (from single-electron excited states); in green, transitions into levels with energies between 0 and 150 eV (comprising mainly transitions between singly- and doubly-excited states); in purple, transitions occurring between doubly-excited states (lying above 150 eV) and higher-lying multiply-excited states. Top: Opacity spectra of the individual Sn ions. Bottom: Total opacity spectrum. The left inset contains the simplified atomic structure of Sn^{13+} (see Fig. 6.1 and main text), while the right inset shows the relative charge state population of the plasma. All spectra are convoluted with a Gaussian profile to improve the visibility of the various contributions.

tra are calculated at the representative temperature and density of 32 eV and 0.002 g/cm^3 (approximately 10^{20} e/cm^3). These plasma conditions, used throughout this chapter, are typical for a 1-μm-driven LPP tailored for emission of 13.5 nm photons, as suggested by radiation hydrodynamic simulations [125, 129] (see supplementary material). Light emission is described as happening at sub-critical density, close to the sonic surface of the ablation front at an electron density close to 10^{20} e/cm^3. These density and temperature values also support the LTE approach adopted, as given by Griem's criterion [144].

In Fig. 6.2, the contribution of the four ion stages Sn^{11+}–Sn^{14+} to the total opacity is shown. Each spectrum shows the three major bound-bound contributions, which can be loosely associated with singly-excited, doubly-excited, and triply-excited states (see Fig. 6.1). Remarkably, for this choice of temperature and density, the well-known transitions to the ground levels comprise only 11 % of the total opacity in the 5 nm to 20 nm range. The remaining 89% is associated with higher-lying transitions: 26 % is attributed to transitions between singly- and doubly-excited states, 25 % to transitions between doubly- and triply-excited states, and 38 % is associated with higher excitations. Even when considering the opacity in a 2 % bandwidth around 13.5 nm, the transitions from singly-excited configurations only account for 19 % of the total opacity.

6.3 Comparison

In order to benchmark our present calculations, we have made comparisons with experimental laser-produced tin-plasma spectra recorded for a variety of laser intensities, which in turn determine the plasma temperature and the plasma charge state balance [27]. The experimental spectra were obtained by irradiating a molten Sn microdroplet, 30 μm in diameter, with a 15-ns-long Nd:YAG laser-pulse having a flat-top spatial profile of 96 μm diameter [27,152]. The emission in the EUV regime is recorded using a wavelength-calibrated spectrometer [141]. The experiment is described in further detail in Ref. [27]. Spectra have been recorded at three distinct laser intensities: $1.4{\cdot}10^{11}$ W/cm^2 (this value gives optimal performance with respect to EUV emission [27]), $6.6 \cdot 10^{10}$ W/cm^2, and $3.9 \cdot 10^{10}$ W/cm^2.

To enable a comparison between opacity calculations and experimental emission spectra, we must adopt a model for radiation transport through the plasma medium. In LTE, the complexity of the radiation transfer problem is reduced since the (spectral) emissivity η_λ and the (spectral) opacity κ_λ are linked by the relation $\eta_\lambda = B_\lambda \cdot \kappa_\lambda \cdot \rho$ [153], where B_λ is Planck's spectral radiance and ρ the mass density (the product of κ_λ and ρ being the absorptivity α_λ). Gen-

erally, even in the 1D approximation, the radiation transport equation should be solved numerically along the plasma column leading to the observer. This would necessitate the calculation of opacities for each (ρ,T) pair. Such an endeavor, particularly in view of the level of detail in the opacity calculations here presented, is beyond the scope of this work. Instead, a single-temperature, single-density approach is here employed. For such a medium, the spectral flux I_λ can be determined using the simple solution $I_\lambda = B_\lambda\,[1 - \exp(-\tau)]$, with the optical depth τ defined as the product between α_λ and the transport path-length L. The temperature of the opacities are chosen such that the calculated charge state contributions matched the observed one. In order to justify the choice of density and path length, we have undertaken radiation hydrodynamic simulations using the RALEF-2D code [125, 129, 165]. These simulations indicate that the vast majority of the emission originates in a 10- to 30-μm-thick plasma having density on the order of $10^{20}\,e/\mathrm{cm}^3$, rather independent of laser intensity (see supplementary material). In our comparisons below, we use a constant 30-μm path length at $10^{20}\,e/\mathrm{cm}^3$ density.

In Fig. 6.3, a comparison between the experimental emission spectra and the spectral fluxes obtained from applying the aforementioned 1D radiation transport model to the ATOMIC opacity calculations is presented for three different laser intensities. Overall, the level of agreement is excellent. Fig. 6.3(a) shows the spectrum for the laser intensity $1.4 \cdot 10^{11}\,\mathrm{W/cm}^2$. The spectral flux calculated using the single-density, single-temperature approach is able to reproduce the experimental emission strikingly well. The figure also shows the plasma opacity from Fig. 6.2, which makes apparent that without the contributions from the multiply excited states it would not be possible to fully explain the experimental spectrum. To further highlight the importance of these transitions, our results are compared with calculations from previous works. The dashed line was obtained using the opacity from Colgan *et al.* [119], which, as discussed in a previous section, perfectly exemplifies the shift of the main emission feature towards shorter wavelengths, arising from inaccuracies in the calculated line positions for transitions between highly-excited states. The dotted line is based on opacity data from Ref. [28], generated with the HULLAC code at an electron temperature of 30 eV but at a higher mass density of $0.01\,\mathrm{g/cm}^3$. To enable the comparison at similar optical depth, the path length used to calculate the spectral flux was a corresponding five time shorter. These calculations significantly overestimate the width of the main emission feature and are in poor agreement with the experimental spectra and, while some disparities could be explained by the density difference, the overall discrepancy should be attributed to the atomic structure employed.

Fig. 6.3(b) and (c) show the comparison between calculations and experiment at lower laser intensities. These spectra clearly exhibit the spectral signa-

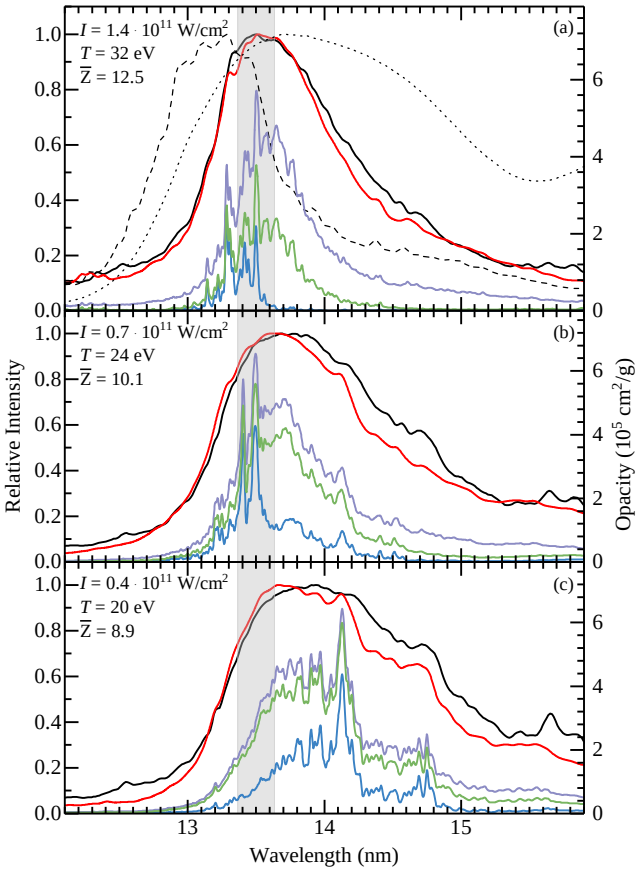

FIGURE 6.3 Comparison between experimental spectra (black solid lines) and calculated fluxes (red solid lines), all normalized to their respective maximum. The spectral fluxes are the result of the 1D radiation transport through a single-density ($0.002\,\mathrm{g/cm^3}$), single-temperature plasma (see main text). Panel (a) includes the spectral flux calculated using an opacity spectrum from Ref. [119] (dashed line) and the spectral flux obtained from HULLAC calculations [28] (dotted line). Opacity spectra, broken down according to the various contributions illustrated in Fig. 6.2 are also shown. The mean charge state $\bar{Z}$ of the calculation is given as well. The shaded gray area highlights the industrially-relevant 2 % bandwidth around 13.5 nm.

ture of lower Sn charge states. The data are still in good agreement, even though some deviations are observed in the 14–16 nm region. Indeed, our assumptions might (partially) break down at lower intensities, due to inapplicability of the single-density, single-temperature approach or deviation from the calculated charge state balance. The opacity breakdowns for these two cases show that the relevance of the highly excited states decreases for the lower plasma temperatures but they are still necessary for complete opacity spectra.

6.4 Discussion and conclusions

It is interesting to consider why multiply excited states appear to be so important in Sn plasma. Lower Z elements under similar conditions, e.g. Al or Fe, are also ionized approximately ten times; however, this results in ion stages with much simpler configurations, such as open-2p- or open-3p-subshells in Al and Fe respectively. Multiply-excited states in these subshells have much smaller statistical weights compared to the multiply-excited states of Sn, and so their relative contribution to the plasma emission is also much smaller. If instead one looks once again at open-$4d$-subshells but in a lighter element, such as neutral Sr, the multiply-excited states are energetically much further away from the ground state due to the smaller nuclear charge. Compared to Sn, this significantly reduces their contribution to the partition function. For example, the $4p^5\,4d^3$ configuration in neutral Sr at a temperature of 1 eV contributes 10^{-13} times less than in the case of the same configuration for Sn ions in a 30 eV plasma. For all of these reasons, Sn finds itself in this peculiar position in which, due to the plasma conditions necessary for nanolithography, the complicated structures of these multiple, $n = 4$ excited-electron configurations play a staggeringly important role.

In summary, we show that the opacity of high-density Sn plasma of relevance for nanolithographic applications are characterized by a remarkably large contribution from highly-excited states. Multiple electron excitation into the $4d$ or $4f$ subshells leads to states with very high angular momenta and large statistical weights, as well as very large dipole line strengths. These configurations are heavily affected by configuration-interaction, making them challenging to calculate accurately. Crucially, the dominant bound-bound transitions involving these multiply-excited states are clustered close to 13.5 nm, as are the transitions from singly-excited states, which explains the intense emission feature from Sn laser-produced plasmas used in the nanolithographic industry. The calculations are shown to be in excellent agreement with experimental emission spectra from a droplet-based, Sn laser-produced-plasma source. Our results will enable accurate simulation of emission spectra from radiation hydrodynamic

simulations of high-density Sn plasmas. They also emphasize the importance of multiply-excited states in extreme ultraviolet sources, which could also play an important role in other short-wavelength applications [166] ranging from beyond-EUV lithography [167] to water-window imaging [168].

6.5 Acknowledgments

We thank J. Abdallah and C.J. Fontes for useful discussions. This project has received funding from European Research Council (ERC) Starting Grant number 802648 and is part of the VIDI research programme with project number 15697, which is financed by the Netherlands Organization for Scientific Research (NWO). Part of this work has been carried out at the Advanced Research Center for Nanolithography (ARCNL), a public-private partnership of the University of Amsterdam (UvA), the Vrije Universiteit Amsterdam (VU), NWO and the semiconductor equipment manufacturer ASML. Part of this work was supported by the US Department of Energy through the Los Alamos National Laboratory. Los Alamos National Laboratory is operated by Triad National Security, LLC, for the National Nuclear Security Administration of U.S. Department of Energy (Contract No. 89233218NCA000001).

6.6 Appendix

This appendix explores where the extreme ultraviolet light is generated in a laser-produced plasma resulting from the irradiation of a Sn microdroplet by a high-intensity, 1-μm-wavelength laser-pulse. This investigation starts by performing RALEF-2D simulations. RALEF-2D is a two-dimensional numerical code which solves the 2D single-fluid, one-temperature hydrodynamics equations and the spectral radiation transfer equation, making it very apt to simulate systems in which energy transport by thermal radiation plays a significant role [125,129,165,169]. It was also recently validated against measurements of laser-induced propulsion of Sn microdroplets [25].

The simulations begin by setting the initial conditions of the system: droplet size, spatial and temporal laser profiles, and laser energy. For the three spectra shown in Fig. 3 of this chapter, the parameters are as follows: 30 μm droplet diameter; box-shaped laser profiles, 96 μm spatially, and 15 ns temporally; laser energies of 170 mJ, 78 mJ, and 47 mJ, corresponding to $1.4 \cdot 10^{11}\,\mathrm{W/cm^2}$, $0.7 \cdot 10^{11}\,\mathrm{W/cm^2}$, and $0.4 \cdot 10^{11}\,\mathrm{W/cm^2}$ intensities. From the simulation results, it is possible to obtain the spatial dependency of temperature and density as a function of time. The duration of the laser beam is sufficient to have a steady-state ablation front, and therefore in the following we will look at the time instant

at the end of the laser pulse (before it is turned off). To simplify the analysis, the 2D arrays are reduced to 1D profiles obtained along a line 60 °with respect to the laser propagation direction (emulating the observation angle of the spectrometer in the experiment).

Temperature and density, and their spatial variations, set the radiation transport properties of the plasma medium. In order to characterize the emission, we will use a heavily simplified version of the radiation transport equation. Firstly, we assume that scattering is small relative to absorption mechanisms; secondly, we look at frequency integrated variables to simplify the amount of data necessary for these calculations. In this static limit, all variables are ultimately a function of only the position along the transport length s and therefore the radiation transport equation reads:

$$\frac{\partial I}{\partial s} = \alpha[B(T) - I], \tag{6.1}$$

with I the frequency-integrated radiation intensity, s the path length variable, α the non-linearly averaged absorption coefficient, and $B(T) = \sigma T^4/\pi$. In order to solve the previous equation, one needs an approximate value for α. In general, this quantity is equated to the Planck mean opacity:

$$\alpha \approx \alpha_P \equiv \frac{1}{B(T)} \int_0^\infty \alpha_\nu B_\nu \mathrm{d}\nu. \tag{6.2}$$

The Planck mean opacity, in the case of Sn plasma, can be calculated as follows [129]:

$$\alpha_P\,[\mathrm{m}^{-1}] = 3.3 \cdot 10^{-7} \cdot \rho\,[\mathrm{g/cm}^3] \cdot T^{-1}\,[\mathrm{eV}]. \tag{6.3}$$

The solution to equation (6.1) reads:

$$I(s) = I_0 \exp\left[-\int_{s0}^{s} \alpha(s')\mathrm{d}s'\right] + \int_{s0}^{s} \alpha(s')B(s') \exp\left[-\int_{s'}^{s} \alpha(s'')\mathrm{d}s''\right]\mathrm{d}s', \tag{6.4}$$

which can be easily solved numerically using the profiles obtained from RALEF-2D.

The solution to $I(s)$ is presented, alongside the temperature and density profiles, for the three laser intensities in Fig. 6.4. These profiles, besides their absolute values, are rather independent of laser intensity. They clearly show that the vast majority of the radiation field intensity builds up in the first 20 µm,

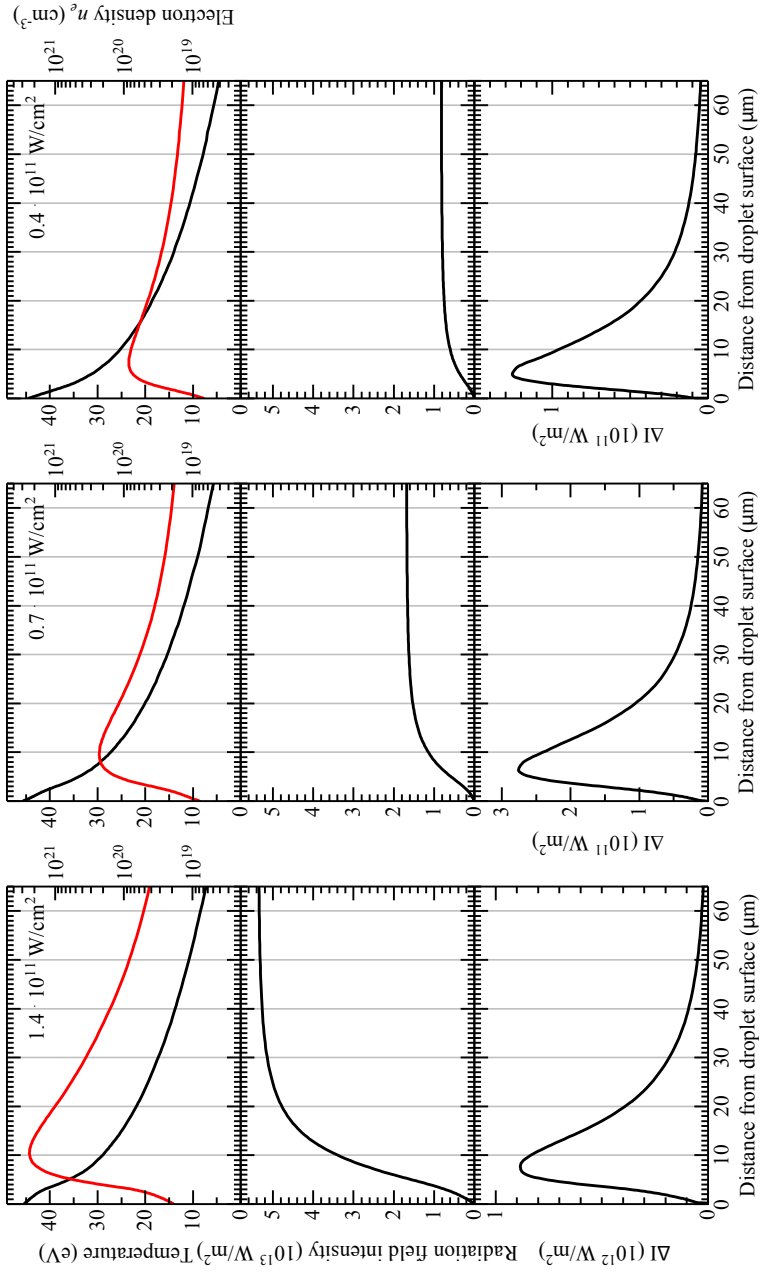

FIGURE 6.4 (Caption on the following page).

FIGURE 6.4 (Figure on the previous page) Top: temperature (red solid line, left-hand axis) and density (black solid line, right-hand axis) profiles calculated by RALEF-2D simulations for the three laser intensities. Middle: radiation field intensity obtained by solving the radiation transport equation. Bottom: Difference between radiation field intensities in two adjacent positions, indicators of the local radiation emission. Note that the y-axes in the bottom plots are individually scaled for readability. See main text for further details.

then leveling off as the lower temperature, rarefied plasma does not contribute strongly to the radiation field, neither in emission nor in absorption. Perhaps of even more practical use is the differential of $I(s)$, i.e. the difference between radiation field intensities in two adjacent positions. When looking at infinitesimal increments, this quantity reads (following from the radiation transport equation):

$$\Delta I = I(s + \mathrm{d}s) - I(s) \approx I(s)[\exp(-\alpha \mathrm{d}s) - 1] + \alpha B \mathrm{d}s, \tag{6.5}$$

where the first term of the right-hand-side can be identified as the absorption contribution (always negative) and the second term is the emissivity. Therefore, ΔI is a good measure of the local radiation emission. This quantity peaks at approximately $2 \cdot 10^{20}\, e/\mathrm{cm}^3$ electron density, with the majority of the radiation originating at the $10^{20}\, e/\mathrm{cm}^3$ level. Moreover, these emission characteristics are independent of laser intensity and common to all the three cases explored. The values found are in good agreement with the ones chosen in the 1D radiation model necessary to compare the opacity calculations to the experimental emission spectra, where a path length of 30 μm together with the density of $10^{20}\, e/\mathrm{cm}^3$ gives very good agreement with the experimental data.

On the other hand, temperature peak values given by the code are higher than expected. These results are rather inconsistent with our spectroscopic measurements simply on the basis of charge state balance. If we look at the highest intensity case in Fig. 6.4, temperatures over 45 eV are observed. At this temperature, we would expect a plasma average charge state above 14+ according to Ref. [129]. This is demonstrably not the case. These discrepancies could be originating from the opacity tables employed in RALEF-2D, which do not include the contribution from highly-excited states as outlined in the present work. As the laser intensities and associated temperatures are shown to have a minor influence on density and length scale results (cf. Fig. 6.4), these minor inconsistencies do not impact the results of said density and length scales.

APPENDIX A

OPACITY AND EMISSIVITY IN LTE

The previous chapters of this thesis deal with the concept of plasma opacity. The use of this quantity is widespread in different branches of physics, particularly when it is necessary to calculate the emission and absorption of photons by a medium. The frequency-dependent opacity κ_ν, typically expressed in units of cm^2/g, is defined as the ratio between the absorptivity α_ν and the mass density ρ. In the following, we will focus exclusively on bound-bound transitions, since these are the strongest contributors in laser-produced-plasma for nanolithograpy. In general, bound-free and free-free cross-sections need to be included as contribution to the total absorption coefficient α_ν. This quantity can be calculated when the atomic structure and population of the absorbing medium is known, and it is defined as

$$\alpha_\nu = \sum_{i<j} \sigma_{\nu,ij} \left(n_i - \frac{g_i}{g_j} n_j \right), \tag{A.1}$$

typically expressed in cm^{-1}. n_i and n_j are the populations the lower and upper level of a transition, respectively, and g_i, g_j are the levels statistical weights. $\sigma_{\nu,ij}$ is the absorption cross-section:

$$\sigma_{\nu,ij} = \frac{\pi e^2}{m_e c} f_{ij} \phi(\nu), \tag{A.2}$$

with f_{ij} the oscillator strength*, and $\phi(\nu)$ the frequency-dependent line shape for absorption (defined such that $\int_0^\infty \phi(\nu)\,\mathrm{d}\nu = 1$).

*A handy relationship to calculate f_{ij} using the Einstein's coefficient is $f_{ij} = 2.30457 \cdot 10^{-8} \cdot A_{ij}\ [\mathrm{s}^{-1}]/\Delta E_{ij}^2\ [\mathrm{eV}]$

The frequency-dependent emissivity is

$$\eta_\nu = \frac{2h\nu^3}{c^2} \sum_{i<j} \sigma_{\nu,ij} \frac{g_i}{g_j} n_j, \tag{A.3}$$

assuming that emissivity and absorptivity have the same line shape.

In LTE, the ratio between η_ν and α_ν (the so-called source function S_ν) is equal to the black-body radiation spectrum. In the following, we will prove this relationship. For simplicity, let us look at the single contribution between a lower level i and an upper level j. The ratio between emission and absorption coefficients reads

$$S_\nu = \frac{\eta_{\nu,ij}}{\alpha_{\nu,ij}} = \frac{2h\nu^3}{c^2} f_{ij} \frac{g_i}{g_j} n_j \frac{1}{f_{ij}} \frac{1}{n_i} \left(1 - \frac{g_i}{g_j} \frac{n_j}{n_i}\right)^{-1}. \tag{A.4}$$

Finally, we can invoke the condition of LTE and the fact that excited level populations follow Boltzmann's distribution:

$$\frac{n_j}{n_i} = \frac{g_j}{g_i} \exp\left(-\frac{E_j - E_i}{kT}\right). \tag{A.5}$$

Using this relation, all the ratios between degeneracies cancel out and we are left with the following:

$$S_\nu = \frac{2h\nu^3}{c^2} \frac{\exp(-\Delta E/kT)}{1 - \exp(-\Delta E/kT)}. \tag{A.6}$$

Remembering that $E = h\nu$ and dividing both numerator and denominator by $\exp(-\Delta E/kT)$, we obtain

$$S_\nu = \frac{2h\nu^3}{c^2} \frac{1}{\exp(-h\nu/kT) - 1} = B_\nu. \tag{A.7}$$

REFERENCES

[1] J. Bardeen and W. H. Brattain, "The transistor, a semi-conductor triode", Phys. Rev. **74**(2), 230–231 (1948).

[2] "Nobel prize in Physics 1956: W. B. Shockley, J. Bardeen, and W. H. Brattain", `https://www.nobelprize.org/prizes/physics/1956/summary/`, accessed: 2019-08-02.

[3] "Nobel prize in Physics 2000: Z. I. Alferov, H. Kroemer, and J. S. Kilby", `https://www.nobelprize.org/prizes/physics/2000/summary/`, accessed: 2019-08-02.

[4] Z. I. Alferov, "Nobel lecture: The double heterostructure concept and its applications in physics, electronics, and technology", Rev. Mod. Phys. **73**(3), 767–782 (2001).

[5] "Annual Semiconductor Sales Increase 21.6 Percent, Top $400 Billion for First Time", `https://www.semiconductors.org/annual-semiconductor-sales-increase-21.6-percent-top-400-billion-for-first-time/`, accessed: 2019-08-02.

[6] G. E. Moore, "Cramming more components onto integrated circuits", Proc. IEEE **86**(1), 82–85 (1998).

[7] G. E. Moore, "Progress in digital integrated electronics", Proc. IEDM Tech. Dig. **11**(3), 11–13 (1975).

[8] "International Technology Roadmap for Semiconductors", `http://www.itrs2.net/`, accessed: 2019-08-02.

[9] C. A. Mack, "Fifty years of moore's law", IEEE Trans. Semicond. Manuf. **24**(2), 202–207 (2011).

[10] H. J. Levinson, *Principles of lithography*, SPIE press, fourth edn. (2019), ISBN 978-1510627604.

[11] "Asml", `https://www.asml.com/en/company/about-asml`, accessed: 2019-08-02.

[12] D. Abercrombie, P. Lacour, O. El-Sewefy, A. Volkov, E. Levine, K. Arb, C. Reid, Q. Li, and P. Ghosh, "Double patterning from design enablement to verification", in "Photomask Technology 2011", vol. 8166, p. 81660X (2011).

[13] I. Fomenkov, "EUV source for high volume manufacturing: performance at 250 W and key technologies for power scaling", `https://www.euvlitho.com/2017/S1.pdf`, EUVL Workshop 2017.

[14] C. Wagner and N. Harned, "EUV lithography: Lithography gets extreme", Nat. Photonics **4**(1), 24 (2010).

[15] V. Bakshi (Editor), *EUV Lithography*, SPIE Press, second edn. (2018).

[16] S. Bajt, J. B. Alameda, T. W. Barbee, Jr., W. M. Clift, J. A. Folta, B. B. Kaufmann, and E. A. Spiller, "Improved reflectance and stability of Mo-Si multilayers", Opt. Eng. **41**(8), 1797–1804 (2002).

[17] I. Fomenkov, D. Brandt, A. Ershov, A. Schafgans, Y. Tao, G. Vaschenko, S. Rokitski, M. Kats, M. Vargas, M. Purvis, R. Rafac, B. La Fontaine, S. De Dea, A. LaForge, J. Stewart, S. Chang, M. Graham, D. Riggs, T. Taylor, M. Abraham, and D. Brown, "Light sources for high-volume manufacturing EUV lithography: technology, performance, and power scaling", Adv. Opt. Techn. **6**(3-4), 173–186 (2017).

[18] M. Purvis, I. V. Fomenkov, A. A. Schafgans, M. Vargas, S. Rich, Y. Tao, S. I. Rokitski, M. Mulder, E. Buurman, M. Kats, J. Stewart, A. D. LaForge, C. Rajyaguru, G. Vaschenko, A. I. Ershov, R. J. Rafac, M. Abraham, D. C. Brandt, and D. J. Brown, "Industrialization of a robust EUV source for high-volume manufacturing and power scaling beyond 250W", in "Extreme Ultraviolet (EUV) Lithography IX", vol. 10583, p. 1058327, International Society for Optics and Photonics (2018).

[19] A. L. Klein, *Laser impact on flying drops*, Ph.D. thesis, University of Twente (2017).

[20] D. Kurilovich, *Laser-induced dynamics of liquid tin microdroplets*, Ph.D. thesis, Vrije Universiteit Amsterdam (2019).

[21] R. Lebert, T. Krücken, and H.-J. Kunze, "Fundamentals and limits of plasma-based euv sources", in V. Bakshi (Editor), "EUV sources for lithography", chap. 7, pp. 197–222, SPIE Press (2006).

[22] O. O. Versolato, "Physics of laser-driven tin plasma sources of EUV radiation for nanolithography", Plasma Sources Sci. Technol. **28**(8), 083001 (2019).

[23] D. Kurilovich, A. L. Klein, F. Torretti, A. Lassise, R. Hoekstra, W. Ubachs, H. Gelderblom, and O. O. Versolato, "Plasma propulsion of a metallic microdroplet and its deformation upon laser impact", Phys. Rev. Appl. **6**(1), 014018 (2016).

[24] D. Hudgins, N. Gambino, B. Rollinger, and R. Abhari, "Neutral cluster debris dynamics in droplet-based laser-produced plasma sources", J. Phys. D **49**(18), 185205 (2016).

[25] D. Kurilovich, M. M. Basko, D. A. Kim, F. Torretti, R. Schupp, J. C. Visschers, J. Scheers, R. Hoekstra, W. Ubachs, and O. O. Versolato, "Power-law scaling of plasma pressure on laser-ablated tin microdroplets", Phys. Plasmas **25**(1), 012709 (2018).

[26] S. A. Reijers, D. Kurilovich, F. Torretti, H. Gelderblom, and O. O. Versolato, "Laser-to-droplet alignment sensitivity relevant for laser-produced plasma sources of extreme ultraviolet light", J. Appl. Phys. **124**(1), 013102 (2018).

[27] R. Schupp, F. Torretti, R. A. Meijer, M. Bayraktar, J. Scheers, D. Kurilovich, A. Bayerle, K. S. E. Eikema, S. Witte, W. Ubachs, R. Hoekstra, and O. O. Versolato, "Efficient generation of extreme ultraviolet light from nd:yag-driven microdroplet-tin plasma", Phys. Rev. Applied **12**(1), 014010 (2019).

[28] S. Fujioka, H. Nishimura, K. Nishihara, A. Sasaki, A. Sunahara, T. Okuno, N. Ueda, T. Ando, Y. Tao, Y. Shimada, K. Hashimoto, M. Yamaura, K. Shigemori, M. Nakai, K. Nagai, T. Norimatsu, T. Nishikawa, N. Miyanaga, Y. Izawa, and K. Mima, "Opacity effect on extreme ultraviolet radiation from laser-produced tin plasmas", Phys. Rev. Lett. **95**(23), 235004 (2005).

[29] J. White, P. Dunne, P. Hayden, F. O'Reilly, and G. O'Sullivan, "Optimizing 13.5 nm laser-produced tin plasma emission as a function of laser wavelength", Appl. Phys. Lett. **90**(18), 181502 (2007).

[30] G. O'Sullivan, B. Li, R. D'Arcy, P. Dunne, P. Hayden, D. Kilbane, T. McCormack, H. Ohashi, F. O'Reilly, P. Sheridan, E. Sokell, C. Suzuki, and T. Higashiguchi, "Spectroscopy of highly charged ions and its relevance to EUV and soft x-ray source development", J. Phys. B: At. Mol. Opt. Phys. **48**(14), 144025 (2015).

[31] J. Bauche, C. Bauche-Arnoult, and O. Peyrusse, *Atomic Properties in Hot Plasmas*, Springer International Publishing (2015), ISBN 978-3-319-18146-2.

[32] S. S. Churilov and A. N. Ryabtsev, "Analyses of the Sn IX–Sn XII spectra in the EUV region", Phys. Scr. **73**(6), 614 (2006).

[33] S. S. Churilov and A. N. Ryabtsev, "Analysis of the $4p^6\,4d^7$–($4p^6\,4d^6\,4f$ + $4p^5\,4d^8$) transitions in the Sn VIII spectrum", Opt. Spectrosc. **100**(5), 660–666 (2006).

[34] S. S. Churilov and A. N. Ryabtsev, "Analysis of the spectra of In XII–XIV and Sn XIII–XV in the far-VUV region", Opt. Spectrosc. **101**(2), 169–178 (2006).

[35] A. N. Ryabtsev, É. Ya. Kononov, and S. S. Churilov, "Spectra of rubidium-like Pd X-Sn XIV ions", Opt. Spectrosc. **105**(6), 844–850 (2008).

[36] I. Y. Tolstikhina, S. S. Churilov, A. N. Ryabtsev, and K. N. Koshelev, "Atomic tin data", in V. Bakshi (Editor), "EUV sources for lithography", chap. 4, pp. 113–148, SPIE Press (2006).

[37] H. Ohashi, S. Suda, H. Tanuma, S. Fujioka, H. Nishimura, A. Sasaki, and K. Nishihara, "EUV emission spectra in collisions of multiply charged Sn ions with He and Xe", J. Phys. B: At. Mol. Opt. Phys. **43**(6), 065204 (2010).

[38] J. Benschop, V. Banine, S. Lok, and E. Loopstra, "Extreme ultraviolet lithography: status and prospects", J. Vac. Sci. Technol. B **26**(6), 2204 (2008).

[39] V. Y. Banine, K. N. Koshelev, and G. H. P. M. Swinkels, "Physical processes in EUV sources for microlithography", J. Phys. D: Appl. Phys. **44**(25), 253001 (2011).

[40] V. I. Azarov and Y. N. Joshi, "Analysis of the $4d^7$–$4d^6\,5p$ transition array of the eighth spectrum of tin: Sn VIII", J. Phys. B: At. Mol. Opt. Phys. **26**(20), 3495–3514 (1993).

[41] W. Svendsen and G. O'Sullivan, "Statistics and characteristics of XUV transition arrays from laser-produced plasmas of the elements tin through iodine", Phys. Rev. A **50**(5), 3710–3718 (1994).

[42] J. Sugar, V. Kaufman, and W. L. Rowan, "Resonance lines $4p^6$–$4p^5\ 4d$ of the Kr I isoelectronic sequence", J. Opt. Soc. Am. B **8**(10), 2026–2027 (1991).

[43] J. Sugar, V. Kaufman, and W. L. Rowan, "Rb-like spectra: Pd X to Nd XXIV", J. Opt. Soc. Am. B **9**(11), 1959–1961 (1992).

[44] H. Ohashi, S. Suda, H. Tanuma, S. Fujioka, H. Nishimura, K. Nishihara, T. Kai, A. Sasaki, H. A. Sakaue, N. Nakamura, and S. Ohtani, "Complementary spectroscopy of tin ions using ion and electron beams", in "J. Phys.: Conf. Ser.", vol. 163, p. 012071, IOP Publishing (2009).

[45] R. D'Arcy, H. Ohashi, S. Suda, H. Tanuma, S. Fujioka, H. Nishimura, K. Nishihara, C. Suzuki, T. Kato, F. Koike, J. White, and G. O'Sullivan, "Transitions and the effects of configuration interaction in the spectra of Sn XV–Sn XVIII", Phys. Rev. A **79**(4), 042509 (2009).

[46] R. D'Arcy, H. Ohashi, S. Suda, H. Tanuma, S. Fujioka, H. Nishimura, K. Nishihara, C. Suzuki, T. Kato, F. Koike, A. O'Connor, and G. O'Sullivan, "Identification of $4d$–$5p$ transitions in the spectra of Sn XV–Sn XIX recorded from collisions between Sn ions and He", J. Phys. B: At. Mol. Opt. Phys. **42**(16), 165207 (2009).

[47] J. Yatsurugi, E. Watanabe, H. Ohashi, H. A. Sakaue, and N. Nakamura, "EUV spectroscopy of highly charged ions with high- and low-energy EBITs", Phys. Scr. **2011**(T144), 014031 (2011).

[48] M. F. Gu, "The flexible atomic code", Can. J. Phys. **86**(5), 675–689 (2008).

[49] S. W. Epp, J. R. Crespo López-Urrutia, M. C. Simon, T. Baumann, G. Brenner, R. Ginzel, N. Guerassimova, V. Mäckel, P. H. Mokler, B. L. Schmitt, H. Tawara, and J. Ullrich, "X-ray laser spectroscopy of highly charged ions at FLASH", J. Phys. B: At. Mol. Opt. Phys. **43**(19), 194008 (2010).

[50] E. Eliav, U. Kaldor, and Y. Ishikawa, "Open-shell relativistic coupled-cluster method with Dirac-Fock-Breit wave functions: Energies of the gold atom and its cation", Phys. Rev. A **49**(3), 1724–1729 (1994).

[51] E. Eliav, U. Kaldor, and Y. Ishikawa, "Ionization potentials and excitation energies of the alkali-metal atoms by the relativistic coupled-cluster method", Phys. Rev. A **50**(2), 1121–1128 (1994).

[52] R. D. Cowan, *The Theory of Atomic Structure and Spectra*, University of California Press (1981).

[53] I. Lindgren, "Relativistic many-body and QED calculations on atomic systems", Int. J. Quantum Chem. **57**(4), 683–695 (1996).

[54] E. Eliav, U. Kaldor, and Y. Ishikawa, "Relativistic coupled-cluster method: Intrashell excitations in the f^2 shells of Pr^{3+} and U^{4+}", Phys. Rev. A **51**(1), 225 (1995).

[55] D. K. Nandy and B. K. Sahoo, "Development of a relativistic coupled-cluster method for one-electron detachment theory: Application to Mn IX, Fe X, Co XI, and Ni XII ions", Phys. Rev. A **88**(5), 052512 (2013).

[56] M. S. Safronova, V. A. Dzuba, V. V. Flambaum, U. I. Safronova, S. G. Porsev, and M. G. Kozlov, "Highly charged ions for atomic clocks, quantum information, and search for α variation", Phys. Rev. Lett. **113**(3), 030801 (2014).

[57] A. Windberger, J. R. Crespo López-Urrutia, H. Bekker, N. S. Oreshkina, J. C. Berengut, V. Bock, A. Borschevsky, V. A. Dzuba, E. Eliav, Z. Harman, U. Kaldor, S. Kaul, U. I. Safronova, V. V. Flambaum, C. H. Keitel, P. O. Schmidt, J. Ullrich, and O. O. Versolato, "Identification of the predicted $5s$–$4f$ level crossing optical lines with applications to metrology and searches for the variation of fundamental constants", Phys. Rev. Lett. **114**(15), 150801 (2015).

[58] A. N. Ryabtsev and E. Ya. Kononov, "Resonance transitions in Rh VIII, Pd IX, Ag X and Cd XI spectra", Phys. Scr. **84**(1), 015301 (2011).

[59] B. M. Penetrante, J. N. Bardsley, D. DeWitt, M. Clark, and D. Schneider, "Evolution of ion-charge-state distributions in an electron-beam ion trap", Phys. Rev. A **43**(9), 4861 (1991).

[60] G. Brenner, J. R. Crespo López-Urrutia, Z. Harman, P. H. Mokler, and J. Ullrich, "Lifetime determination of the Fe XIV $3s^2\,3p\;{}^2P^\circ_{3/2}$ metastable level", Phys. Rev. A **75**(3), 032504 (2007).

[61] H. Bekker, O. O. Versolato, A. Windberger, N. S. Oreshkina, R. Schupp, T. M. Baumann, Z. Harman, C. H. Keitel, P. O. Schmidt, J. Ullrich, and J. R. Crespo López-Urrutia, "Identifications of $5s_{1/2}$–$5p_{3/2}$ and $5s^2$–$5s\,5p$ EUV transitions of promethium-like Pt, Ir, Os and Re", J. Phys. B: At. Mol. Opt. Phys. **48**(14), 144018 (2015).

[62] G. C. Rodrigues, P. Indelicato, J. P. Santos, P. Patté, and F. Parente, "Systematic calculation of total atomic energies of ground state configurations", At. Data. Nucl. Data Tables **86**(2), 117–233 (2004).

[63] A. Kramida, Yu. Ralchenko, J. Reader, and and NIST ASD Team, NIST Atomic Spectra Database (ver. 5.3), [Online]. Available: `http://physics.nist.gov/asd` [2016, February 2]. National Institute of Standards and Technology, Gaithersburg, MD. (2015).

[64] J. Sucher, "Foundations of the relativistic theory of many-electron atoms", Phys. Rev. A **22**(2), 348 (1980).

[65] Y. Ishikawa, R. Baretty, and R. C. Binning Jr, "Relativistic gaussian basis set calculations on one-electron ions with a nucleus of finite extent", Chem. Phys. Lett. **121**(1), 130–133 (1985).

[66] E. Eliav, M. J. Vilkas, Y. Ishikawa, and U. Kaldor, "Extrapolated intermediate hamiltonian coupled-cluster approach: Theory and pilot application to electron affinities of alkali atoms", J. Chem. Phys. **122**(22), 224113 (2005).

[67] G. L. Malli, A. B. F. Da Silva, and Y. Ishikawa, "Universal gaussian basis set for accurate *ab initio* relativistic Dirac-Fock calculations", Phys. Rev. A **47**(1), 143 (1993).

[68] TRAFS-3C code (Tel-Aviv Relativistic Atomic Fock-Space coupled cluster code), written by E. Eliav, U. Kaldor and Y. Ishikawa (1990-2013), with contributions by A. Landau.

[69] V. M. Shabaev, I. I. Tupitsyn, and V. A. Yerokhin, "QEDMOD: Fortran program for calculating the model Lamb-shift operator", Comput. Phys. Commun. **189**, 175 – 181 (2015).

[70] J. R. Crespo López-Urrutia, P. Beiersdorfer, K. Widmann, and V. Decaux, "Visible spectrum of highly charged ions: The forbidden optical lines of Kr, Xe, and Ba ions in the Ar I to Kr I isoelectronic sequence", Can. J. Phys. **80**(12), 1687–1700 (2002).

[71] Y. Kobayashi, K. Kubota, K. Omote, A. Komatsu, J. Sakoda, M. Minoshima, D. Kato, J. Li, H. A. Sakaue, I. Murakami, and N. Nakamura, "Extreme ultraviolet and visible spectroscopy of promethiumlike heavy ions", Phys. Rev. A **92**(2), 022510 (2015).

[72] A. Borovik Jr, M. F. Gharaibeh, P. M. Hillenbrand, S. Schippers, and A. Müller, "Detailed investigation of electron-impact single-ionization

cross sections and plasma rate coefficients of N-shell tin ions", J. Phys. B: At. Mol. Opt. Phys. **46**(17), 175201 (2013).

[73] A. Kramida, "The program LOPT for least-squares optimization of energy levels", Comp. Phys. Comm. **182**(2), 419–434 (2011).

[74] A. N. Ryabtsev and E. Ya. Kononov, "Eighth spectrum of palladium: Pd VIII", Phys. Scr. **91**(2), 025402 (2016).

[75] E. Biémont, R. D. Cowan, and J. E. Hansen, "Transition probabilities for forbidden lines in the ground-state configuration of the bromine isoelectronic sequence", Phys. Scr. **37**(6), 850 (1988).

[76] J. Bauche, C. Bauche-Arnoult, and M. Klapisch, "Transition arrays in the spectra of ionized atoms", Adv. Atom. Mol. Phys. **23**, 131–195 (1988).

[77] S. Fujioka, M. Shimomura, Y. Shimada, S. Maeda, H. Sakaguchi, Y. Nakai, T. Aota, H. Nishimura, N. Ozaki, A. Sunahara, K. Nishihara, N. Miyanaga, Y. Izawa, and K. Mima, "Pure-tin microdroplets irradiated with double laser pulses for efficient and minimum-mass extreme-ultraviolet light source production", Appl. Phys. Lett. **92**(24), 241502 (2008).

[78] H. Mizoguchi, T. Abe, Y. Watanabe, T. Ishihara, T. Ohta, T. Hori, A. Kurosu, H. Komori, K. Kakizaki, A. Sumitani, O. Wakabayashi, H. Nakarai, J. Fujimoto, and A. Endo, "First generation laser-produced plasma source system for HVM EUV lithography", in "Extreme Ultraviolet (EUV) Lithography", vol. 7636, p. 763608, International Society for Optics and Photonics (2010).

[79] A. Windberger, F. Torretti, A. Borschevsky, A. Ryabtsev, S. Dobrodey, H. Bekker, E. Eliav, U. Kaldor, W. Ubachs, R. Hoekstra, J. R. Crespo López-Urrutia, and O. O. Versolato, "Analysis of the fine structure of Sn^{11+}–Sn^{14+} ions by optical spectroscopy in an electron-beam ion trap", Phys. Rev. A **94**(1), 012506 (2016).

[80] V. V. Flambaum, A. A. Gribakina, G. F. Gribakin, and M. G. Kozlov, "Structure of compound states in the chaotic spectrum of the Ce atom: localization properties, matrix elements, and enhancement of weak perturbations", Phys. Rev. A **50**(1), 267 (1994).

[81] V. A. Dzuba, V. V. Flambaum, G. F. Gribakin, and C. Harabati, "Chaos-induced enhancement of resonant multielectron recombination in highly charged ions: Statistical theory", Phys. Rev. A **86**(2), 022714 (2012).

[82] J. C. Berengut, C. Harabati, V. A. Dzuba, V. V. Flambaum, and G. F. Gribakin, "Level-resolved quantum statistical theory of electron capture into many-electron compound resonances in highly charged ions", Phys. Rev. A **92**(6), 062717 (2015).

[83] C. Harabati, J. C. Berengut, V. V. Flambaum, and V. A. Dzuba, "Electron recombination with tungsten ions with openf-shells", J. Phys. B: At. Mol. Opt. Phys. **50**(12), 125004 (2017).

[84] V. A. Dzuba, V. V. Flambaum, and M. G. Kozlov, "Combination of the many-body perturbation theory with the configuration-interaction method", Phys. Rev. A **54**(5), 3948–3959 (1996).

[85] J. C. Berengut, V. V. Flambaum, and M. G. Kozlov, "Calculation of isotope shifts and relativistic shifts in C I, C II, C III, and C IV", Phys. Rev. A **73**, 012504 (2006).

[86] J. C. Berengut, V. V. Flambaum, A. Ong, J. K. Webb, J. D. Barrow, M. A. Barstow, S. P. Preval, and J. B. Holberg, "Limits on the dependence of the fine-structure constant on gravitational potential from white-dwarf spectra", Phys. Rev. Lett. **111**(1), 010801 (2013).

[87] A. Ong, J. C. Berengut, and V. V. Flambaum, "Measuring chemical evolution and gravitational dependence of α using ultraviolet Fe V and Ni V transitions in white-dwarf spectra", Phys. Rev. A **88**(5), 052517 (2013).

[88] I. M. Savukov, "Configuration-interaction many-body-perturbation-theory energy levels of four-valent Si I", Phys. Rev. A **91**(2), 022514 (2015).

[89] J. C. Berengut, "Isotope shifts and relativistic shifts of cr ii for the study of α variation in quasar absorption spectra", Phys. Rev. A **84**(5), 052520 (2011).

[90] J. C. Berengut, "Particle-hole configuration interaction and many-body perturbation theory: Application to Hg^+", Phys. Rev. A **94**(1), 012502 (2016).

[91] P. H. M. Uylings, A. J. J. Raassen, and J.-F. Wyart, "Calculations of $5d^{N-1}\,6s$ systems using orthogonal operators: do orthogonal operators survive configuration interaction?", J. Phys. B: At. Mol. Opt. Phys. **26**(24), 4683 (1993).

[92] J. E. Hansen, P. H. M. Uylings, and A. J. J. Raassen, "Parametric fitting with orthogonal operators", Phys. Scr. **37**, 664–672 (1988).

[93] T. Harada and T. Kita, "Mechanically ruled aberration-corrected concave gratings", Appl. Opt. **19**(23), 3987–3993 (1980).

[94] W. R. Johnson, S. A. Blundell, and J. Sapirstein, "Finite basis sets for the dirac equation constructed from B splines", Phys. Rev. A **37**(2), 307 (1988).

[95] V. A. Dzuba and W. R. Johnson, "Calculation of the energy levels of barium using B splines and a combined configuration-interaction and many-body-perturbation-theory method", Physical Review A **57**(4), 2459 (1998).

[96] K. Beloy and A. Derevianko, "Application of the dual-kinetic-balance sets in the relativistic many-body problem of atomic structure", Comp. Phys. Comm. **179**(5), 310 (2008).

[97] M. G. Kozlov and S. G. Porsev, "Effective hamiltonian for valence electrons of an atom", Optics and Spectroscopy **87**, 352–356 (1999).

[98] V. A. Dzuba, "V^{N-M} approximation for atomic calculations", Phys. Rev. A **71**(3), 032512 (2005).

[99] J. S. M. Ginges and J. C. Berengut, "QED radiative corrections and many-body effects in atoms: vacuum polarization and binding energy shifts in alkali metals", J. Phys. B: At. Mol. Opt. Phys. **49**(9), 095001 (2016).

[100] J. S. M. Ginges and J. C. Berengut, "Atomic many-body effects and lamb shifts in alkali metals", Phys. Rev. A **93**(5), 052509 (2016).

[101] V. V. Flambaum and J. S. M. Ginges, "Radiative potential and calculations of QED radiative corrections to energy levels and electromagnetic amplitudes in many-electron atoms", Phys. Rev. A **72**(5), 052115 (2005).

[102] F. A. Parpia, C. Froese Fischer, and I. P. Grant, "GRASP92: A package for large-scale relativistic atomic structure calculations", Comp. Phys. Comm. **94**(2), 249–271 (1996).

[103] J. E. Hansen, A. J. J. Raassen, P. H. M. Uylings, and G. M. S. Lister, "Parametric fitting to d^N configurations using orthogonal operators", Nucl. Instrum. Meth. Phys. Res. Sect. B: Beam Interact. Mater. Atoms **31**(1), 134–138 (1988).

[104] A. N. Ryabtsev and E. Ya. Kononov, "Resonance transitions in the Pd VII spectrum", Phys. Scr. **85**(2), 025301 (2012).

[105] G. J. van het Hof and Y. N. Joshi, "The analysis of the $4d^8$, $4d^7\,5s$ and $4d^7\,5p$ configurations of six-times ionized tin: Sn VII", Phys. Scr. **48**(6), 714 (1993).

[106] V. I. Azarov, Y. N. Joshi, S. S. Churilov, and A. N. Ryabtsev, "Analysis of the $4d^7$ ($4f$ + $6p$) and $4p^5\,4d^9$ configurations of Sn VII, Sb VIII and Te IX", Phys. Scr. **50**(6), 642 (1994).

[107] P. Beiersdorfer, J. Crespo López-Urrutia, V. Decaux, K. Widmann, and P. Neill, "Polarization spectroscopy of x-ray transitions from beam-excited highly charged ions", Rev. Sci. Instrum. **68**(1), 1073–1076 (1997).

[108] A. S. Shlyaptseva, R. C. Mancini, P. Neill, P. Beiersdorfer, J. R. Crespo López-Urrutia, and K. Widmann, "Polarization-dependent spectra of x-ray dielectronic satellite lines of Be-like Fe", Phys. Rev. A **57**(2), 888–898 (1998).

[109] H. Jörg, Z. Hu, H. Bekker, M. A. Blessenohl, D. Hollain, S. Fritzsche, A. Surzhykov, J. R. Crespo López-Urrutia, and S. Tashenov, "Linear polarization of x-ray transitions due to dielectronic recombination in highly charged ions", Phys. Rev. A **91**(4), 042705 (2015).

[110] C. Shah, H. Jörg, S. Bernitt, S. Dobrodey, R. Steinbrügge, C. Beilmann, P. Amaro, Z. Hu, S. Weber, S. Fritzsche, A. Surzhykov, J. R. Crespo López-Urrutia, and S. Tashenov, "Polarization measurement of dielectronic recombination transitions in highly charged krypton ions", Phys. Rev. A **92**(4), 042702 (2015).

[111] C. W. Nielson and G. F. Koster, *Spectroscopic Coefficients for the p^n, d^n, and f^n Configurations*, MIT press (1963).

[112] A. J. J. Raassen and Th. A. M. van Kleef, "Analysis of the fifth spectrum of palladium (Pd V)", Physica B+C **142**(3), 359–374 (1986).

[113] A. J. J. Raassen and Th. A. M. van Kleef, "Analysis of the sixth spectrum of palladium (Pd VI)", Physica B+C **146**(3), 423–437 (1987).

[114] A. N. Ryabtsev and E. Ya. Kononov, "Resonance transitions in Rh VIII, Pd IX, Ag X and Cd XI spectra", Phys. Scr. **84**(1), 015301 (2011).

[115] Th. A. M. van Kleef, A. J. J. Raassen, and Y. N. Joshi, "Analysis of the $4d^7$–$4d^6\,5p$ transitions in the fifth spectrum of silver (Ag V)", Phys. Scr. **36**(1), 140 (1987).

[116] Y. N. Joshi, A. J. J. Raassen, Th. A. M. van Kleef, and A. A. van der Valk, "The sixth spectrum of silver: Ag VI, and a study of the parameter values in $4d$-spectra", Phys. Scr. **38**(5), 677 (1988).

[117] Y. Kawasuji, K. M. Nowak, T. Hori, T. Okamoto, H. Tanaka, Y. Watanabe, T. Abe, T. Kodama, Y. Shiraishi, H. Nakarai, T. Yamazaki, S. Okazaki, T. Saitou, H. Mizoguchi, and Y. Shiraishi, "Key components technology update of the 250W high-power LPP-EUV light source", in "SPIE Advanced Lithography", vol. 10143, p. 101432G, International Society for Optics and Photonics (2017).

[118] Q. Huang, V. Medvedev, R. van de Kruijs, A. Yakshin, E. Louis, and F. Bijkerk, "Spectral tailoring of nanoscale EUV and soft x-ray multilayer optics", Appl. Phys. Rev. **4**(1), 011104 (2017).

[119] J. Colgan, D. P. Kilcrease, J. Abdallah Jr, M. E. Sherrill, C. J. Fontes, P. Hakel, and G. S. J. Armstrong, "Atomic structure considerations for the low-temperature opacity of Sn", High Energy Density Phys. **23**, 133–137 (2017).

[120] F. Torretti, A. Windberger, A. Ryabtsev, S. Dobrodey, H. Bekker, W. Ubachs, R. Hoekstra, E. V. Kahl, J. C. Berengut, J. R. Crespo López-Urrutia, and O. O. Versolato, "Optical spectroscopy of complex open-$4d$-shell ions Sn^{7+}–Sn^{10+}", Phys. Rev. A **95**(4), 042503 (2017).

[121] B. Mertens, M. Weiss, H. Meiling, R. Klein, E. Louis, R. Kurt, M. Wedowski, H. Trenkler, B. Wolschrijn, R. Jansen, A. van de Runstraat, R. Moors, K. Spee, S. Plöger, and R. van de Kruijs, "Progress in EUV optics lifetime expectations", Microelectron. Eng. **73**, 16–22 (2004).

[122] C. Bauche-Arnoult, J. Bauche, and M. Klapisch, "Asymmetry of $l^{N+1} - l^N l'$ transition-array patterns in ionic spectra", Phys. Rev. A **30**(6), 3026–3032 (1984).

[123] S. A. George, W. T. Silfvast, K. Takenoshita, R. T. Bernath, C.-S. Koay, G. Shimkaveg, and M. C. Richardson, "Comparative extreme ultraviolet emission measurements for lithium and tin laser plasmas", Opt. Lett. **32**(8), 997–999 (2007).

[124] H. Tanaka, A. Matsumoto, K. Akinaga, A. Takahashi, and T. Okada, "Comparative study on emission characteristics of extreme ultraviolet radiation from CO_2 and Nd:YAG laser-produced tin plasmas", Appl. Phys. Lett. **87**(4), 041503 (2005).

[125] M. M. Basko, "On the maximum conversion efficiency into the 13.5-nm extreme ultraviolet emission under a steady-state laser ablation of tin microspheres", Phys. Plasmas **23**(8), 083114 (2016).

[126] B. L. Henke, E. M. Gullikson, and J. C. Davis, "X-ray interactions: Photoabsorption, scattering, transmission, and reflection at E = 50-30'000 eV, Z = 1-92", At. Data. Nucl. Data Tables **54**(2), 181 – 342 (1993).

[127] G. O'Sullivan, A. Cummings, C. Z. Dong, P. Dunne, P. Hayden, O. Morris, E. Sokell, F. O'Reilly, M. G. Su, and J. White, "Emission and absorption in laser produced plasmas: processes and applications", in "J. Phys. Conf. Ser.", vol. 163, p. 012003, IOP Publishing (2009).

[128] D. Colombant and G. F. Tonon, "X-ray emission in laser-produced plasmas", J. Appl. Phys. **44**(8), 3524–3537 (1973).

[129] M. M. Basko, V. G. Novikov, and A. S. Grushin, "On the structure of quasi-stationary laser ablation fronts in strongly radiating plasmas", Phys. Plasmas **22**(5), 053111 (2015).

[130] M. G. Su, Q. Min, S. Q. Cao, D. X. Sun, P. Hayden, G. O'Sullivan, and C. Z. Dong, "Evolution analysis of EUV radiation from laser-produced tin plasmas based on a radiation hydrodynamics model", Sci. Rep. **7**, 45212 (2017).

[131] D. Kilbane and G. O'Sullivan, "Ground-state configurations and unresolved transition arrays in extreme ultraviolet spectra of lanthanide ions", Phys. Rev. A **82**(6), 062504 (2010).

[132] J. White, P. Hayden, P. Dunne, A. Cummings, N. Murphy, P. Sheridan, and G. O'Sullivan, "Simplified modeling of 13.5 nm unresolved transition array emission of a Sn plasma and comparison with experiment", J. Appl. Phys. **98**(11), 113301 (2005).

[133] M. M. Waldrop, "The chips are down for Moore's law", Nature **530**(7589), 144 (2016).

[134] P. J. van Zwol, M. Nasalevich, W. P. Voorthuijzen, E. Kurganova, A. Notenboom, D. Vles, M. Peter, W. Symens, A. J. M. Giesbers, J. H. Klootwijk, R. W. E. van de Kruijs, and W. J. van der Zande, "Pellicle films supporting the ramp to HVM with EUV", in "Photomask Technology 2017", vol. 10451, p. 104510O, International Society for Optics and Photonics (2017).

[135] K. Liu, Y. Li, F. Zhang, and M. Fan, "Transient thermal and structural deformation and its impact on optical performance of projection optics for extreme ultraviolet lithography", Jpn. J. Appl. Phys. **46**(10A), 6568–6572 (2007).

[136] G. Yang and Y. Li, "Analysis and control of thermal and structural deformation of projection optics for 22-nm EUV lithography", in "Extreme Ultraviolet (EUV) Lithography III", vol. 8322, p. 83222V, International Society for Optics and Photonics (2012).

[137] F. Torretti, R. Schupp, D. Kurilovich, A. Bayerle, J. Scheers, W. Ubachs, R. Hoekstra, and O. O. Versolato, "Short-wavelength out-of-band EUV emission from Sn laser-produced plasma", J. Phys. B: At. Mol. Opt. Phys. **51**(4) (2018).

[138] H.-K. Chung, M. H. Chen, W. L. Morgan, Y. Ralchenko, and R. W. Lee, "FLYCHK: Generalized population kinetics and spectral model for rapid spectroscopic analysis for all elements", High Energy Density Phys. **1**(1), 3 – 12 (2005).

[139] I. Fomenkov, "EUVL Exposure Tools for HVM: Status and Outlook", `https://www.euvlitho.com/2016/P2.pdf` (2016), EUVL Workshop 2016.

[140] H. Chen, X. Wang, L. Duan, H. Lan, Z. Chen, D. Zuo, and P. Lu, "Angular distribution of ions and extreme ultraviolet emission in laser-produced tin droplet plasma", J. Appl. Phys. **117**(19), 193302 (2015).

[141] S. J. Goh, H. J. M. Bastiaens, B. Vratzov, Q. Huang, F. Bijkerk, and K. J. Boller, "Fabrication and characterization of free-standing, high-line-density transmission gratings for the vacuum UV to soft X-ray range", Opt. Express **23**(4), 4421–4434 (2015).

[142] M. Bayraktar, H. M. Bastiaens, C. Bruineman, B. Vratzov, and F. Bijkerk, "Broadband transmission grating spectrometer for measuring the emission spectrum of EUV sources", NEVAC blad **54**(1), 14–19 (2016).

[143] L. Poletto, A. Boscolo, and G. Tondello, "Characterization of a charge-coupled-device detector in the 1100–0.14-nm (1-eV to 9-keV) spectral region", Appl. Opt. **38**(1), 29–36 (1999).

[144] H. R. Griem, "Validity of local thermal equilibrium in plasma spectroscopy", Phys. Rev. **131**(3), 1170–1176 (1963).

[145] P. Mora, "Theoretical model of absorption of laser light by a plasma", Phys. Fluids **25**(6), 1051–1056 (1982).

[146] A. A. Schafgans, D. J. Brown, I. V. Fomenkov, R. Sandstrom, A. Ershov, G. Vaschenko, R. Rafac, M. Purvis, S. Rokitski, Y. Tao, D. J. Riggs, W. J.

Dunstan, M. Graham, N. R. Farrar, D. C. Brandt, N. Böwering, A. Pirati, N. Harned, C. Wagner, H. Meiling, and R. Kool, "Performance optimization of MOPA pre-pulse LPP light source", in "Extreme Ultraviolet (EUV) Lithography VI", vol. 9422, p. 94220B, International Society for Optics and Photonics (2015).

[147] S. K. Moore, "EUV lithography finally ready for fabs", IEEE Spectrum **55**(1), 46–48 (2018).

[148] M. A. Purvis, A. Schafgans, D. J. W. Brown, I. Fomenkov, R. Rafac, J. Brown, Y. Tao, S. Rokitski, M. Abraham, M. Vargas, S. Rich, T. Taylor, D. Brandt, A. Pirati, A. Fisher, H. Scott, A. Koniges, D. Eder, S. Wilks, A. Link, and S. Langer, "Advancements in predictive plasma formation modeling", in "Extreme Ultraviolet (EUV) Lithography VII", vol. 9776, p. 97760K, International Society for Optics and Photonics (2016).

[149] P. Hayden, A. Cummings, N. Murphy, G. O'Sullivan, P. Sheridan, J. White, and P. Dunne, "13.5 nm extreme ultraviolet emission from tin based laser produced plasma sources", J. Appl. Phys. **99**(9), 093302 (2006).

[150] A. Z. Giovannini and R. S. Abhari, "Three-dimensional extreme ultraviolet emission from a droplet-based laser-produced plasma", J. Appl. Phys. **114**(3), 033303 (2013).

[151] A. Z. Giovannini and R. S. Abhari, "Effects of the dynamics of droplet-based laser-produced plasma on angular extreme ultraviolet emission profile", Appl. Phys. Lett. **104**(19), 194104 (2014).

[152] R. A. Meijer, A. S. Stodolna, K. S. E. Eikema, and S. Witte, "High-energy Nd:YAG laser system with arbitrary sub-nanosecond pulse shaping capability", Opt. Lett. **42**(14), 2758–2761 (2017).

[153] H. A. Scott, "Collisional-radiative modeling for radiation hydrodynamics codes", in Y. Ralchenko (Editor), "Modern Methods in Collisional-Radiative Modeling of Plasmas", chap. 4, pp. 81–104, Springer International Publishing (2016).

[154] M. Murakami, S. Fujioka, H. Nishimura, T. Ando, N. Ueda, Y. Shimada, and M. Yamaura, "Conversion efficiency of extreme ultraviolet radiation in laser-produced plasmas", Phys. Plasmas **13**(3), 033107 (2006).

[155] A. Hassanein, V. A. Sizyuk, T. S. Sizyuk, and S. S. Harilal, "Effects of plasma spatial profile on conversion efficiency of laser-produced plasma sources for EUV lithography", J. Micro/Nanolithogr. MEMS MOEMS **8**(4), 041503 (2009).

[156] A. Hassanein, T. Sizyuk, V. Sizyuk, and S. S. Harilal, "Combined effects of pre-pulsing and target geometry on efficient EUV production from laser produced plasma experiments and modeling", in "Extreme Ultraviolet (EUV) Lithography II", vol. 7969, p. 79690D, International Society for Optics and Photonics (2011).

[157] H. A. Scott, "Cretin - a radiative transfer capability for laboratory plasmas", J. Quant. Spectrosc. Radiat. Transf. **71**(2-6), 689–701 (2001).

[158] J. Zeng, C. Gao, and J. Yuan, "Detailed investigations on radiative opacity and emissivity of tin plasmas in the extreme-ultraviolet region", Phys. Rev. E **82**(2), 026409 (2010).

[159] N. H. Magee, J. Abdallah, J. Colgan, P. Hakel, D. P. Kilcrease, S. Mazevet, M. Sherrill, C. J. Fontes, and H. L. Zhang, "Los Alamos opacities: Transition from LEDCOP to ATOMIC", in "AIP Conference Proceedings", vol. 730, pp. 168–179, AIP (2004).

[160] P. Hakel, M. E. Sherrill, S. Mazevet, J. Abdallah Jr, J. Colgan, D. P. Kilcrease, N. H. Magee, C. J. Fontes, and H. L. Zhang, "The new Los Alamos opacity code ATOMIC", J. Quant. Spectr. Rad. Transfer **99**(1-3), 265–271 (2006).

[161] J. Abdallah Jr, R. E. H. Clark, J. M. Peek, and C. J. Fontes, "Kinetics calculations for near Ne-like ions", J. Quant. Spectr. Rad. Transfer **51**(1-2), 1–8 (1994).

[162] C. J. Fontes, H. L. Zhang, J. Abdallah Jr, R. E. H. Clark, D. P. Kilcrease, J. Colgan, R. T. Cunningham, P. Hakel, N. H. Magee, and M. E. Sherrill, "The Los Alamos suite of relativistic atomic physics codes", J. Phys. B: At. Mol. Opt. Phys. **48**(14), 144014 (2015).

[163] P. Hakel and D. P. Kilcrease, "CHEMEOS: A new chemical-picture-based model for plasma equation-of-state calculations", in "AIP Conference Proceedings", vol. 730, pp. 190–199, AIP (2004).

[164] D. P. Kilcrease, J. Colgan, P. Hakel, C. J. Fontes, and M. E. Sherrill, "Equations of state for opacity calculations", in "Workshop on Astrophysical Opacities", vol. 515 of *Astronomical Society of the Pacific Conference Series*, ASP (2018).

[165] M. M. Basko, P. V. Sasorov, M. Murakami, V. G. Novikov, and A. S. Grushin, "One-dimensional study of the radiation-dominated implosion of a cylindrical tungsten plasma column", Plasma Phys. Control. Fusion **54**(5), 055003 (2012).

[166] D. Bleiner, J. Costello, F. Dortan, G. O'Sullivan, L. Pina, and A. Michette (Editors), *Short Wavelength Laboratory Sources*, The Royal Society of Chemistry (2015), ISBN 978-1-84973-456-1.

[167] G. Tallents, E. Wagenaars, and G. Pert, "Optical lithography: Lithography at EUV wavelengths", Nat. Photonics **4**(12), 809–811 (2010).

[168] H. Legall, G. Blobel, H. Stiel, W. Sandner, C. Seim, P. Takman, D. H. Martz, M. Selin, U. Vogt, H. M. Hertz, D. Esser, H. Sipma, J. Luttmann, M. Höfer, H. D. Hoffmann, S. Yulin, T. Feigl, S. Rehbein, P. Guttmann, G. Schneider, U. Wiesemann, M. Wirtz, and W. Diete, "Compact x-ray microscope for the water window based on a high brightness laser plasma source", Opt. Express **20**(16), 18362–18369 (2012).

[169] M. M. Basko, J. A. Maruhn, and A. Tauschwitz, "Development of a 2D radiation-hydrodynamics code RALEF for laser plasma simulations", GSI Report 2010-1, PLASMA-PHYSICS-25, GSI Helmholtzzentrum für Schwerionenforschung GmbH (2010).

List of publications

Chapter One:
A. Windberger, **F. Torretti**, A. Borschevsky, A. Ryabtsev, S. Dobrodey, H. Bekker, E. Eliav, U. Kaldor, W. Ubachs, R. Hoekstra, J. R. Crespo López-Urrutia, and O. O. Versolato, "Analysis of the fine structure of Sn^{11+}–Sn^{14+} ions by optical spectroscopy in an electron beam ion trap", Phys. Rev. A **94**(1), 012506 (2016)

Chapter Two:
F. Torretti, A. Windberger, A. Ryabtsev, S. Dobrodey, H. Bekker, W. Ubachs, R. Hoekstra, E. V. Kahl, J. C. Berengut, J. R. Crespo López-Urrutia, and O. O. Versolato, "Optical spectroscopy of complex open $4d$-shell ions Sn^{7+}–Sn^{10+}", Phys. Rev. A **95**(4), 042503 (2017)

Chapter Three:
F. Torretti, R. Schupp, D. Kurilovich, A. Bayerle, J. Scheers, W. Ubachs, R. Hoekstra, and O. O. Versolato, "Short-wavelength out-of-band euv emission from Sn laser-produced plasma", J. Phys. B: At. Mol. Opt. Phys. **51**(4), 045005 (2018)

Chapter Four:
F. Torretti, F. Liu, M. Bayraktar, J. Scheers, Z. Bouza, W. Ubachs, R. Hoekstra, and O. O. Versolato, "Spectral characterization of an industrial EUV light source for nanolithography", Submitted (August 2019)

Chapter Five:
R. Schupp, **F. Torretti**, R. A. Meijer, M. Bayraktar, J. Sheil, J. Scheers, D. Kurilovich, A. Bayerle, A. A. Schafgans, M. Purvis, K. S. E. Eikema, S. Witte, W. Ubachs, R. Hoekstra, and O. O. Versolato, "Radiation transport and scaling of optical depth in Nd:YAG laser-produced microdroplet-tin plasma", Appl. Phys. Lett. **115**(12), 124101 (2019)

CHAPTER SIX:
F. Torretti, J. Sheil, R. Schupp, M. M. Basko, M. Bayraktar, R. A. Meijer, S. Witte, W. Ubachs, R. Hoekstra, O. O. Versolato, A. J. Neukirch, and J. Colgan, "Unexpectedly large radiative emission between highly-excited states in Sn laser-produced plasma", Submitted (August 2019)

The author has also contributed to the following publications:

- R. Schupp, **F. Torretti**, R. A. Meijer, M. Bayraktar, J. Scheers, D. Kurilovich, A. Bayerle, K. S. E. Eikema, S. Witte, W. Ubachs, R. Hoekstra, and O. O. Versolato, "Efficient generation of extreme ultraviolet light from Nd:YAG-driven microdroplet-tin plasma", Phys. Rev. Appl. **12**(1), 014010 (2019).
- J. Scheers, A. Ryabtsev, A. Borschevsky, J. C. Berengut, K. Haris, R. Schupp, D. Kurilovich, **F. Torretti**, A. Bayerle, E. Eliav, W. Ubachs, O. O. Versolato, and R. Hoekstra, "Energy Level Structure of Sn^{3+} Ions", Phys. Rev. A **98**(6), 062503 (2018).
- D. Kurilovich, T. de F. Pinto, **F. Torretti**, R. Schupp, J. Scheers, A. S. Stodolna, H. Gelderblom, K. S. E. Eikema, S. Witte, W. Ubachs, R. Hoekstra, and O. O. Versolato, "Expansion dynamics after laser-induced cavitation in liquid tin microdroplets", Phys. Rev. Appl. **10**(1), 054005 (2018).
- S. A. Reijers, D. Kurilovich, **F. Torretti**, H. Gelderblom, and O. O. Versolato, "Laser-to-droplet alignment sensitivity relevant for laser-produced plasma sources of extreme ultraviolet light", J. Appl. Phys. **124**(1), 013102 (2018).
- D. Kurilovich, M. M. Basko, D. A. Kim, **F. Torretti**, R. Schupp, J. C. Visschers, J. Scheers, R. Hoekstra, W. Ubachs, and O. O. Versolato, "Power-law scaling of plasma pressure on laser-ablated tin microdroplets", Phys. Plasmas **25**(1), 012709 (2018).
- D. Kurilovich, A. L. Klein, **F. Torretti**, A. Lassise, R. Hoekstra, W. Ubachs, H. Gelderblom, and O. O. Versolato, "Plasma propulsion of a metallic microdroplet and its deformation upon laser Impact", Phys. Rev. Appl. **6**(1), 014018 (2016).

Acknowledgments

The past four years have been quite challenging, and this thesis only exists thanks to the help of the people with whom I have had the luck of working. To my supervisors, my colleagues and all the external collaborators, thank you. I share all these accomplishments with you.

Thank you to my friends, with whom I was able to (somewhat) wind down in my time off, and to my family for their eternal support.

I am yet to mention any names simply because one person stands above all others with her contribution. By supporting me through the last six years and pushing me to do better, you could say she is single-handedly responsible for this thesis having seen the light of day. To my wife, Domile Torretti, the most heartfelt of thanks. Words can hardly describe the joy you bring me and the extent of your positive influence on my life but, at the very least, this thesis will stand as a testament to that.

Francesco Torretti
August 2019